

# **For Reference**

---

**NOT TO BE TAKEN FROM THIS ROOM**



Ex LIBRIS  
UNIVERSITATIS  
ALBERTAENSIS





Digitized by the Internet Archive  
in 2023 with funding from  
University of Alberta Library

<https://archive.org/details/Soukup1977>











65

THE UNIVERSITY OF ALBERTA

RELEASE FORM

NAME OF AUTHOR . . . Jan Soukup . . . . .

TITLE OF THESIS . A STUDY OF  $n$ - $n$  QUASI-FREE SCATTERING .  
IN A  $D(n, 2n)p$  EXPERIMENT . . . . .  
. . . . .

DEGREE FOR WHICH THESIS WAS PRESENTED. . . Ph.D. . . . .

YEAR THIS DEGREE WAS GRANTED . . . 1977 . . . . .

Permission is hereby granted to THE UNIVERSITY OF ALBERTA LIBRARY to reproduce single copies of this thesis and to lend or sell such copies for private, scholarly or scientific research purposes only.

The author reserves other publication rights, and neither the thesis nor extensive extracts from it may be printed or otherwise reproduced without the author's written permission.





THE UNIVERSITY OF ALBERTA

A STUDY OF  $n$ - $n$  QUASI-FREE SCATTERING  
IN A  $D(n,2n)p$  EXPERIMENT

BY



JAN SOUKUP

A THESIS

SUBMITTED TO THE FACULTY OF GRADUATE STUDIES AND RESEARCH  
IN PARTIAL FULFILLMENT OF THE REQUIREMENTS FOR THE DEGREE  
OF DOCTOR OF PHILOSOPHY

DEPARTMENT OF PHYSICS

EDMONTON, ALBERTA

SPRING, 1977





THE UNIVERSITY OF ALBERTA

FACULTY OF GRADUATE STUDIES AND RESEARCH

The undersigned certify that they have read, and recommend to the Faculty of Graduate Studies and Research, for acceptance, a thesis entitled A STUDY OF n-n QUASI-FREE SCATTERING IN A  $D(n,2n)p$  EXPERIMENT submitted by JAN SOUKUP in partial fulfillment of the requirements for the degree of Doctor of Philosophy .





## ABSTRACT

An investigation of neutron neutron scattering has been made in the framework of a kinematically complete  $D(n,2n)p$  experiment at 21.5 MeV incident energy where the three body breakup reaction was observed under n-n Quasi Free Scattering geometry.

To improve the low counting rate problem involved in the neutron induced reaction a cryogenic facility, capable of producing  $4 \times 10^7$  23 MeV neutrons/sr sec, was designed and commissioned in this project. A more effective use of the neutron flux produced was achieved by exposing to it an array of deuterium targets in the form of NE230 deuterated scintillators. A set of three such scintillators provided simultaneously, data at three different scattering geometries. Data at a total of nine different quasi-free scattering angle pairs have been obtained in three experimental runs.

The proton pulse in each target scintillator was used as a reference timing signal in the double time-of-flight spectrometer adding to a total of eight parameters processed in coincidence by the electronics for each event. Events from the different NE230 scintillators were sorted by means of four-way routing and recorded event-by-event on a magnetic tape.





The experimental results are reproduced reasonably well by a separable potential approximation of the exact three-body theory in contrast with up to 80% discrepancies reported earlier in the p-p quasi-free scattering experiments at this energy.



## ACKNOWLEDGEMENTS

I am very grateful to Dr. G. C. Neilson for the trust he expressed in me by suggesting a very challenging and also a very rewarding Ph.D. project. His always well thought advice and his active participation are greatly reflected in the success of this work.

I deeply appreciate the help of Dr. Cameron, who provided an up-to-date contact with the development in the few body problems. His reassuring presence and optimism created the healthy spirit needed to complete the project.

I wish to thank Dr. S. T. Lam for his reassurance during the frustrating periods when the project ran into a standstill.

I am also very grateful to Dr. H. W. Fielding for his everpresent cooperation throughout the productive part of the project. Few words, but both hands of efficient help were always present during the endless nights of setting up. I would like to thank the many people who have either cleared up questions, provided stimulating discussions or helped with computer programming, namely: Dr. Allen Anderson, Dr. Wolfgang Breunlich (Vienna), Dr. W. K. Dawson, Dr. David Hutcheon, Dr. W. J. McDonald, Dr. A. C. Miller, Dr. J. G. Rogers, and a group of experimentalists at the University of





Manitoba, namely Dr. W. T. H. van Oers, Dr. D. I. Bonbright and Dr. David Roberts who provided a great source of experience for me by letting me participate in a joint University of Alberta-University of Manitoba D(p,2p)n experiment.

A special thanks goes to the secretarial and technical staff of the Nuclear Research Centre and the Physics Department without whose skilled workmanship this project would be impossible. To name a few, I thank Jock Elliott, Lars Holm, Paul Karvonen, John Schaapman, Con Green, Henry Nielsen, Nick Riebeek.

I wish to thank Jim Pasos, the "Midnight Cowboy", for countless overnight shifts during the experimental runs. The same goes to my other colleagues Ahmed Hussein, Steve Leung and Dr. George Yu.

A very special thanks to Mrs. Lee Cech who did an excellent job of typing the manuscript.

I appreciate the financial assistance of the National Research Council of Canada and the University of Alberta.

Finally, My thanks to my wife and my children for their patience and faith with which they supported me during the long seven years this project took.

- To Hanna -





# TABLE OF CONTENTS

Chapter		Page
A	THEORY	1
A.1	THEORY OF NUCLEAR FORCES	1
A.1.1	Meson Exchange Theory of the Nucleon Nucleon Force	1
A.1.2	Principle of Charge Independence and Charge Symmetry	4
A.1.3	The Low Energy NN System	6
A.2	THREE-NUCLEON BREAK-UP OF THE DEUTERON	11
A.2.1	Kinematics of Three-Particle Reactions and the Differential Cross Section	12
A.2.2	Transition Amplitude $T_{fi}$ - The Exact Three Body Formalism	14
A.2.3	1. Final State Interactions	18
	2. Quasi-Free Scattering in the Deuteron Break-up	20
B	EXPERIMENTAL SYSTEM	25
B.1	INTRODUCTION	25
B.2	THE FAST NEUTRON PRODUCTION FACILITY	30
B.2.1	Description of the $^3\text{H}$ Target and Cryostat	30
B.2.2	Tritium Storage and Filling Manifold	41



Chapter		Page
B.3	DETECTORS AND GEOMETRY	49
B.3.1	Study of the C6D6 Scintillator; Pulse Shape Discrimination	49
B.3.2	Structure of the Double Header Neutron Detectors	56
B.3.3	The Geometry of the Experiment	57
B.4	ELECTRONICS	67
B.4.1	Neutron Time-of-Flight	68
B.4.2	C6D6 Detector Pulse Height (Proton Recoil Energy) and the Four-Way Routing	69
B.4.3	Pulse Shape Discrimination Circuits	70
B.4.4	The Eight-Fold Master Gate	71
B.4.5	The Monitors	72
B.5	THE DATA ACQUISITION PROGRAM	86
B.5.1	The On-Line Analysis Subroutine (ANALYZ)	89
B.6	THE DATA ANALYSIS PROGRAM	93
C	EXPERIMENTAL RESULTS	110
C.1	DEFINITION OF 8-PARAMETER WINDOWS	110
C.2	SOURCES OF BACKGROUND	117
C.3	PLAYBACK OF THE EVENT RECORDED DATA WITH ANALYSIS IN TERMS OF THE NEUTRON TIME-OF-FLIGHT	123
C.3.1	Run #1	124
C.3.2	Run #2	128
C.3.3	Run #3	132





Chapter		Page
C.4	OFF LINE ANALYSIS OF THE EVENT RECORDED DATA	136
C.4.1	Run #1	137
C.4.2	Run #2	139
C.4.3	Run #3	141
C.5	PROJECTION OF THE TWO-DIMENSIONAL DATA AND CALCULATION OF THE ABSOLUTE CROSS SECTION	143
C.5.1	Data Projection	143
C.5.2	The Differential Cross Section	143
C.5.3	Monitor Peak Summing	145
C.5.4	Neutron Detector Efficiency	149
C.5.5	Calculations and Results	151
C.6	DISCUSSION OF RESULTS - CONCLUSIONS	171
REFERENCES		176
APPENDIX 1	THE SAFETY SYSTEM	180



# LIST OF TABLES

Table		Page
1	$\pi$ , $\eta$ , $\rho$ , $\omega$ , $\phi$ Meson Properties	3
2	Absolute Differential Cross Section in Run #1, $\theta_1=\theta_2=35^\circ$ , $\phi_1=0^\circ$ , $\phi_2=180^\circ$	152
3	Absolute Differential Cross Section in Run #2, $\theta_1=\theta_2=23.8^\circ$ , $\phi_1=0^\circ$ , $\phi_2=180^\circ$	155
4	Absolute Differential Cross Section in Run #2, $\theta_1=\theta_2=25.0^\circ$ , $\phi_1=0^\circ$ , $\phi_2=180^\circ$	156
5	Absolute Differential Cross Section In Run #2, $\theta_1=\theta_2=26.3^\circ$ , $\phi_1=0^\circ$ , $\phi_2=180^\circ$	157
6	Absolute Differential Cross Section in Run #3, $\theta_1=\theta_2=28.7^\circ$ , $\phi_1=0^\circ$ , $\phi_2=180^\circ$	160
7	Absolute Differential Cross Section In Run #3, $\theta_1=\theta_2=30.0^\circ$ , $\phi_1=0^\circ$ , $\phi_2=180^\circ$	161
8	Absolute Differential Cross Section in Run #3, $\theta_1=\theta_2=31.4^\circ$ , $\phi_1=0^\circ$ , $\phi_2=180^\circ$	162
9	Run #2 Cross Section Averaged Around $25.0^\circ$ , $-25.0^\circ$ Geometry	165
10	Run #3 Cross Section Averaged Around $30.0^\circ$ , $-30.0^\circ$ Geometry	168
11	Summary of Possible Error Contributions in the Experimental Cross Section	174





## LIST OF FIGURES

Figure		Page
B.1.1	Schematic diagram of the experimental set-up in Run #1 with indication of the eight parameters processed by the electronics in eight-fold coincidence.	27
B.1.2	A photograph of the symmetric quasi-free scattering geometry set up in Run #2.	29
B.2.1.1	Cross section of a cryostat designed to cool a 1.5 mg/cm <sup>2</sup> tritium gas target to liquid nitrogen temperature and to provide safety against tritium gas leakage by means of a liquid helium cryopump.	32
B.2.1.2	Detail of the tritium gas cell housing.	35
B.2.1.3	Time-of-flight spectrum of direct neutrons at 0° produced by 6 MeV pulsed deuteron beam.	40
B.2.2.1	Cross section of the tritium storage and handling manifold.	43
B.2.2.2	Bottom view of the tritium storage and filling manifold.	47
B.2.2.3	Side view of the FNPF cryostat off beam-line with the tritium storage and handling manifold mounted at the bottom of the cryostat and connected to the gas cell inside the cryostat by a continuous stainless steel capillary (sheathed with plastic tube).	47
B.3.1.1	Recoil energy and pulse shape from 23 MeV neutron induced interactions only in NE230 scintillator.	54
B.3.1.2	A photograph of the three C6D6 detectors (right center) and the two neutron detectors (left) mounted in their stands (Run #2).	29



Figure		Page
B.3.3.1	A plane view of the three asymmetric scattering geometries running simultaneously - Run #1.	60
B.3.3.2	A plane view of the three symmetric scattering geometries simultaneously running in Run #3.	62
B.3.3.3	Light response of NE230 (C6D6) detector for recoiling protons and deuterons relative to electrons. (Compiled from: Sm-68, Pa-75 and Br-72 and verified by our experiment.)	64
B.3.3.4	A typical shape of the deuteron recoil peak, in a two-dimensional plot of time-of-flight versus C6D6 detector pulse height, produced by 35° elastic scattering of 21.5 MeV neutrons on deuterons in the C6D6 scintillator.	66
B.4.1	Eight-parameter electronics diagram. Fast and logic signals indicated by thin lines, linear signals indicated by heavy lines.	75
B.4.2	Time-of-flight circuit diagram.	77
B.4.3	Electronics circuit of C6D6 pulse height with four way routing.	79
B.4.4	Pulse shape discrimination circuits.	81
B.4.5	Eight-fold coincidence gate.	83
B.4.6	The electronics circuit of the monitors.	85
B.5.1	A block diagram of the data acquisition program.	88
B.5.2	A logic tree diagram of the Fortran subroutine 'ANALYZ' contained in the data acquisition program as the on-line analysis of the eight-fold coincidence data.	91
B.6.1	The link structure of the off-line data reduction program. Arrows indicate the access between individual links.	96





Figure		Page
B.6.2	Examples of the computer display "pages" included in the data reduction program. First row: calibration of the singles time-of-flight spectrum and definition of TOF and E limits. Second row: definition <sup>n</sup> of the neutron detector pulse shape windows.	98
B.6.3	Examples of the computer display "pages" included in the data reduction program. First row: TOF2/TOF1 histogram of "TRUE" events with an intensified locus (center) and an intensified broadening band around locus (right). Second row: TOF2/TOF1 "RANDOM" events (left), projection of the "RANDOM" events onto TOF1 axis (center) and projection of "TRUE" events onto TOF1 axis (right).	100
B.6.4	A logic tree of a subroutine 'ANALYZ' contained in link 9 of the off-line data reduction program.	107
C.1.1	A two-dimensional plot of pulse height versus pulse shape of an NE213 detector at the lower bias of $1 \times 10^6$ Co in Run #1.	111
C.1.2	A two-dimensional plot of pulse height versus pulse shape of an NE213 detector at the lower bias of $1/3^{22}\text{Na}$ in Runs #2 and 3 (top). The cross hatched area indicates a typical pulse shape window. A corresponding pulse height spectrum of a $^{22}\text{Na}$ source (bottom).	113
C.1.3	A two-dimensional plot of pulse height versus pulse shape of a C6D6 (NE230) detector at the lower bias of $1/4^{241}\text{Am}$ (inset). Routed $^{241}\text{Am}$ source - pulse height spectra in the three C6D6 detectors used simultaneously (under inset).	115
C.2.1	Various true and background coincidence loci (explained in Chapter C.2) as they appear in a TOF2 versus TOF1 plot.	119



Figure		Page
C.2.2	Various true and background coincidence loci (explained in Chapter C.2) as they appear in an $E_2$ versus $E_1$ plot.	119
C.3.1.1	TOF2 x TOF1 isometric plot of "TRUE" events in $35^\circ$ , $-35^\circ$ q.f.s. Run #1.	124
C.3.1.2	TOF2 x TOF1 scatter plot of "TRUE" events in $35^\circ$ , $-35^\circ$ q.f.s. Run #1.	125
C.3.1.3	TOF2 x TOF1 isometric plot of background coincidences in $35^\circ$ , $-35^\circ$ q.f.s. Run #1.	126
C.3.1.4	TOF2 x TOF1 scatter plot of background coincidences in $35^\circ$ , $-35^\circ$ q.f.s. Run #1.	127
C.3.2.1	TOF2 x TOF1 isometric plot of "TRUE" events in $25.0^\circ$ , $-25.0^\circ$ q.f.s. Run #2.	128
C.3.2.2	TOF2 x TOF1 scatter plot of "TRUE" events in $25.0^\circ$ , $-25.0^\circ$ q.f.s. Run #2.	129
C.3.2.3	TOF2 x TOF1 isometric plot of background coincidences in $25.0^\circ$ , $-25.0^\circ$ q.f.s. Run #2.	130
C.3.2.4	TOF2 x TOF1 scatter plot of background coincidences in $25.0^\circ$ , $-25.0^\circ$ q.f.s. Run #2.	131
C.3.3.1	TOF2 x TOF1 isometric plot of "TRUE" events in $30.0^\circ$ , $-30.0^\circ$ q.f.s. Run #3.	132
C.3.3.2	TOF2 x TOF1 scatter plot of "TRUE" events in $30.0^\circ$ , $-30.0^\circ$ q.f.s. Run #3.	133
C.3.3.3	TOF2 x TOF1 isometric plot of background coincidences in $30.0^\circ$ , $-30.0^\circ$ q.f.s. Run #3.	134
C.3.3.4	TOF2 x TOF1 scatter plot of background coincidences in $30.0^\circ$ , $-30.0^\circ$ q.f.s. Run #3.	135
C.4.1.1	$E_2$ x $E_1$ isometric plot of "TRUE" events in $35^\circ$ , $-35^\circ$ q.f.s. Run #1.	137



Figure		Page
C.4.1.2	E2 x E1 scatter plot of "TRUE" events in 35°, -35° q.f.s. Run #1.	138
C.4.2.1	E2 x E1 isometric plot of "TRUE" events in 25.0°, -25.0° q.f.s. Run #2.	139
C.4.2.2	E2 x E1 scatter plot of "TRUE" events in 25.0°, -25.0° q.f.s. Run #2.	140
C.4.3.1	E2 x E1 isometric plot of "TRUE" events in 30.0°, -30.0° q.f.s. Run #3.	141
C.4.3.2	E2 x E1 scatter plot of "TRUE" events in 30.0°, -30.0° q.f.s. Run #3.	142
C.5.3.1	The left and right monitor spectra corresponding to the entire runs #1, #2, and #3. The inset is showing the contribution of n-C elastic scattering into the n-D elastic monitor peak and the reconstruction of their superposition.	148
C.5.4.1	The neutron detector efficiency curves used in this work.	150
C.5.5.1	Comparison of experimental and theoretical differential cross sections for the reaction $n_0 + d \rightarrow n_1 + n_2 + p$ in the projection onto $E_{n_1}$ axis in Run #1. The dashed line indicates the proton energy (right scale).	154
C.5.5.2	Comparison of experimental and theoretical differential cross sections (solid line) for the reaction $n_0 + d \rightarrow n_1 + n_2 + p$ in projection onto the kinematical locus length S for the three angle pairs of Run #2.	159
C.5.5.3	Comparison of experimental and theoretical differential cross sections (solid line) for the reaction $n_0 + d \rightarrow n_1 + n_2 + p$ in projection onto the kinematical locus length S for the three angle pairs of Run #3.	164





Figure		Page
C.5.5.4	<p>Comparison of relevant energies and both experimental and theoretical differential cross sections for the reaction <math>n_0 + d \rightarrow n_1 + n_2 + p</math> at <math>E_0 = 21.5</math> MeV with <math>\phi_1 = 0^\circ</math>, <math>\phi_2 = 180^\circ</math>, <math>\theta_1 = \theta_2 = 25^\circ</math>.  (Upper) Absolute experimental data (step line) and theoretical curves.  (Lower) Relative energies <math>E_{n_1 p}</math>, <math>E_{n_2 p}</math>, <math>E_{n_1 n_2}</math> for f.s.i., proton energy <math>E_p</math> and the production angle <math>\theta_{n_1 n_2 \text{ c.m.}}</math> (dashed line, right scale).</p>	167
C.5.5.5	<p>Equivalent of Fig. C.5.5.4 for <math>\theta_1 = \theta_2 = 30^\circ</math>.</p>	170



## A. THEORY

### A.1 THEORY OF NUCLEAR FORCES

#### A.1.1 Meson Exchange Theory of the Nucleon Nucleon Force

The modern theory of nuclear forces explains the nucleon-nucleon nuclear or "strong" interaction in terms of exchange of mesons. A simplified illustration of this hypothesis can be given on the basis of Heisenberg's relations of uncertainty in the Quantum Mechanical micro-dimensions (He-27). Accordingly, the total energy  $E$  of an isolated nucleon is allowed to fluctuate with an uncertainty  $\Delta E$  related to its time duration  $\tau$  by

$$\Delta E \cdot \tau \approx \hbar \quad (\text{A-1})$$

$\hbar$  ... Planck's constant/ $2\pi$

$\Delta E$  can be expressed in terms of a rest energy  $mc^2$  of a particle, meson, which the nucleon can constantly emit and reabsorb within time intervals  $\tau$ . The meson is "allowed" to travel a distance

$$R = \tau \cdot v \approx \frac{\hbar}{mc} \cdot \frac{v}{c} \quad (\text{A-2})$$

during such interval if  $v$  is its speed. Thus the nucleon could be viewed as a "gallaxy" of mesons, the heavy hadrons concentrated in its centre core and the lightest mesons



thinning off at the longer ranges  $R$  from the center. If two nucleons move to within the meson emission range of each other a meson emitted by one nucleon can be absorbed in the other. The corresponding change in the state of each individual nucleon due to the meson exchange must then be described as their interaction in a two-nucleon system to conserve energy.

If  $v \approx c$  in equation (A-2), for orientation, one obtains:

$$R \approx \frac{\hbar}{mc} = \lambda_c \quad (A-3)$$

The range of nuclear interaction is thus equal to the Compton wave-length  $\lambda_c$  of the exchange particle. For  $R \approx r_0 = 1.4F$  (the observed range of nuclear forces) the corresponding rest mass of the exchanged meson is  $m \approx 270 m_{\text{electron}}$ , which is the known  $\pi$  meson.

A number of mesons of different masses which can be exchanged in the nucleon-nucleon interaction are known today ( $\pi$ ,  $\eta$ ,  $\rho$ ,  $\omega$ ,  $\phi$ ). (see Table 1)

Depending on the proximity of the two interacting nucleons one pion, two pions,  $\eta$ ,  $\rho$ ,  $\omega$ ,  $\phi$  mesons and their combinations can be exchanged in the interaction making its mathematical expression (Pa-70, Lo-68) correspondingly complex if not impossible.





TABLE 1  $\pi, \eta, \rho, \omega, \phi$  MESON PROPERTIES

<u>NAME</u>	<u><math>I^G(J^P)C_n</math></u>	<u>Mass (MeV)</u>
$\pi^\pm$	$1^-(0^-)+$	139.57
$\pi^0$		134.96
$\eta$	$0^+(0^-)+$	$548.8 \pm 0.6$
$\rho$	$1^+(1^-)-$	$773 \pm 3$
$\omega$	$0^-(1^-)-$	$782 \pm 0.3$
$\phi$	$0^-(1^-)-$	$1019.7 \pm 0.3$

J - particle spin

$\ell$  - orbital angular momentum

I - particle isospin

G - parity  $G = C_n(-1)^I$

P - particle parity  $P = -(-1)^\ell$

$C_n$  - charge conjugation parity eigenvalue

see (Re-76) for more information



The simplest of the exchange forces, the One Pion Exchange Potential (OPEP), is based on the derivation of Yukawa (Yu-35) who first hypothesized the meson exchange theory of nuclear forces. Yukawa's potential

$$U(r) = -g^2 \frac{e^{-\kappa r}}{r} \quad (A-4)$$

(where  $g$  is the strong pion-nucleon coupling constant and  $\lambda_c = \frac{1}{\kappa}$  the Compton wavelength of pion), assuming the exchange of one neutral pion, is applicable only for so called long range interaction, i.e., an interaction in which the two nucleons do not come closer than  $\approx 1.5F$ . At closer ranges combinations of simultaneous meson exchange modes alter the interaction drastically. The pseudoscalar or vector character of mesons in spin-isospin space included in the more recent theories is able to account for some observed features of nuclear forces, which Yukawa's central potential fails to explain, (e.g., the spin-dependence of nuclear forces their non-central character, the repulsive core of the potential, etc.). One of the most sensitive probes into the details of the meson exchange theory is to test the charge independence and charge symmetry of nuclear forces.

#### A.1.2 Principle of Charge Independence and Charge Symmetry

It is known that the hadronic part of the nucleon-nucleon force is not only charge symmetric but also charge independent (He-69). It is also known that these postulated



symmetries are proper to the strong or hadronic interaction alone. They are both broken by the electromagnetic and weak interactions. The strength of electromagnetic interactions is characterized by the fine structure constant  $\alpha = 1/137$ . As, on the grounds of the meson exchange theory, the hadronic part in the nucleon-nucleon interaction is always accompanied by long range or short range electromagnetic interactions, it is expected that, in general, the charge independence and charge symmetry of the nucleon-nucleon forces will be broken by a few percent.

Charge independence applied to the nucleon implies that once Coulomb and other small electromagnetic effects are removed, the n-n, n-p and p-p forces are equal in the same states.

Charge symmetry is weaker implying equality only of n-n and p-p forces.

The breaking of charge independence is primarily due to the electromagnetic mass differences of the exchanged mesons (e.g.,  $\pi^+$ ,  $\pi^0$ , see TABLE 1). These effects do not give rise to charge symmetry breaking.

Although there is a clear evidence for the violation of charge independence (He-69), this is not so for charge symmetry. On theoretical grounds, charge-symmetry violating effects must occur for nuclear forces, unless there are accidental cancellations. Such symmetry-breaking effects follow from the theoretically predicted





mixing of isoscalar and isovector mesons (Go-70).

There is indirect evidence for charge symmetry breaking (Ok-67, Ne-71) in low-energy nuclear physics. This comes primarily from the measured binding-energy differences of the mirror nuclei  ${}^3\text{He}$ - ${}^3\text{H}$  and  ${}^{41}\text{Sc}$ - ${}^{41}\text{Ca}$ . The theoretical analyses require an extra attraction of the low energy n-n system relative to the p-p system of roughly 1/2%.

Attempts to test the validity of charge symmetry through direct study of the low energy nucleon-nucleon system are described in the next chapter.

### A.1.3 The Low Energy NN System

The comparison of NN bound states and scattering cross sections, provides a direct test of charge symmetry and charge independence. Unfortunately, only the np system has a bound state, the deuteron, which occurs for an  $l=0$  spin triplet. At low energies (lab. kinetic energy  $\lesssim 10$  MeV) only s-state ( $l=0$ ) NN scattering is important and contributions from higher partial waves can be neglected. The corresponding spin-isospin states allowed by the Pauli principle are the spin singlet  ${}^1S_0$ -isospin triplet ( $T=1$ ) in the nn, np and pp scattering plus the spin triplet  ${}^3S_1$ -isospin singlet ( $T=0$ ) scattering in np system. The latter contribution can be easily removed from the np scattering amplitude with the help of slow-neutron coherent scattering in Hydrogen (Wi-63). Thus at low energies the cross



sections for the three  $T=1$  members of NN scattering can be compared in the same space-spin states  $^1S_0$ . One advantage of the low energy scattering is, that the scattering cross section can be expressed in terms of only  $\ell=0$  phase shift  $\delta_0$  as

$$\frac{d\sigma}{d\Omega} = \frac{1}{k^2} \sin^2 \delta_0(k) \quad (A-5)$$

$k$  ... C.M. momentum

Further advantage is, that this phase shift can be expressed at low energies by the expansion

$$K_0 \equiv k \cot \delta_0 = \frac{1}{a} + \frac{1}{2} r_0 k^2 (-Pr_0^3 k^4 + \dots) \quad (A-6)$$

The comparison of cross sections is thus reduced at low energies to a comparison of just two-parameters, the scattering length ( $a$ ) and the effective range ( $r_0$ ).

It is known experimentally that the nn, pn and pp force in the spin singlet  $^1S_0$  is attractive and the states are almost bound making the scattering length large and negative. Under such conditions a slight change  $\Delta V$  in the depth of nucleon-nucleon potential  $V$  reflects strongly magnified in the corresponding change  $\Delta a$  of the scattering length as the two variables are related by

$$\frac{\Delta a}{a} \approx \frac{a}{r_0} \frac{\Delta V}{V} \quad (A-7)$$



Since the scattering length  $a$  is about an order of magnitude larger than the effective range  $r_0$  of the NN potential in case of  $^1S_0$  state a large magnification of the charge dependent effects is provided by the comparison of nn, pp and np scattering lengths.

Unfortunately, two major hardships beset the direct experimental comparison of the three NN scattering states and these are responsible for existing uncertainty about the charge-symmetry of NN forces to date. These are: (i) the nonexistence of a free-neutron target for direct n-n scattering, and (ii) the presence of the Coulomb force in p-p scattering.

There is no long range electromagnetic force present in the n-p interaction. Careful analysis of the experimental data below 5 MeV, including epithermal neutron scattering, binding energy of the deuteron and coherent scattering of cold neutrons (No-68) yield

$$\left. \begin{aligned} a_{np} &= -23.7146 \pm 0.0127 \text{ F} \\ r_{np} &= 2.76 \pm 0.0127 \text{ F} \end{aligned} \right\} \quad (\text{A-8})$$

The p-p scattering experiment, being the easiest to perform, has been carried out to a great accuracy. The result (He-67)

$$\left. \begin{aligned} a_{pp} &= -7.804 \pm 0.006 \text{ F} \\ r_e &= 2.798 \pm 0.008 \text{ F} \end{aligned} \right\} \quad (\text{A-9})$$





was used as a basis for the theoretical prediction of the charge-dependent nn scattering length  $a_{nn}$  which incorporated the effects of  $\rho$ - $\omega$  and  $\eta$ - $\pi$  mixing in the meson exchange model (He-72). First, however, the presence of the long range electromagnetic interaction in result (A-9) has to be "turned off", which can only be done theoretically. The result of the theoretical subtraction of Coulomb and vacuum polarization, which is not model-independent, in the pp scattering length by Henley et al. (He-72) is:

$$a_{pp} = -17.10 \quad (\text{A-10})$$

The effective range is insensitive to Henley's correction. The uncertainty in result (A-10) was quoted by Henley as  $\pm 0.20$  F. However, in his recent study, Sauer (Sa-76) discloses that, the model dependence of the subtraction of the electromagnetic effects is, in fact, extremely serious. He concludes that the value of -17 F for the nuclear pp scattering length is still most probable, but its model dependence arising from different parametrization of the wave function at small relative distances is disappointingly large.

On the basis of result (A-10) Henley (He-72) made a theoretical prediction of two possible values for the charge dependent (i.e., such as should be found in experiment) neutron-neutron scattering length, depending on the sign of the ratio  $g_{\omega}/g_{\rho}$  of  $\omega$  and  $\rho$  meson strong coupling



constants, which could not be predicted by SU(3) symmetry,

$$a_{nn} = \begin{aligned} & - 17.9 \text{ F} \quad \text{if } g_{\omega}/g_{\rho} > 0 \\ & - 15.0 \text{ F} \quad \text{if } g_{\omega}/g_{\rho} < 0 \end{aligned} \quad (\text{A-11})$$

He then uses the evidence of an extra attraction needed in the n-n system over p-p system, to explain the  $^3\text{He}$ - $^3\text{H}$  and  $^{41}\text{Sc}$ - $^{41}\text{Ca}$  binding energy differences, as an argument for his final choice of the - 17.9 F value over - 15.0 F for the predicted  $a_{nn}$ . This value has to be verified experimentally to prove the validity of the meson exchange model used for the prediction. Henley's value of the nn effective range from the summary of present knowledge (He-69) is

$$r_{nn} = 3.2 \pm 1.6 \text{ F} \quad (\text{A-12})$$

Due to nonexistence of a free-neutron target the nn scattering parameters can only be obtained indirectly in many body (mainly few-particle breakup) reactions where the nn subsystem appears in the final state. The results of such analyses are dependent on, more or less justified, approximations accounting for the effect of the many body framework onto the semi-isolated n-n system. The simplest of the many-body reactions providing the same framework for the comparison of nn, np and pp interactions in its final states is the three body nucleon induced breakup of the deuteron.



## A.2 THREE-NUCLEON BREAK-UP OF THE DEUTERON

In recent years, interest in experimental and theoretical investigations of three-nucleon systems, especially the break-up reactions  ${}^2\text{H}(p,2p)n$  and  ${}^2\text{H}(n,2n)p$ , has been continuously increasing. The aim of all the studies on this subject has been three-fold (Sl-70):

- (i) A systematic analysis of the most important reaction mechanisms; that is, final-state interactions in two-nucleon subsystems (f.s.i.) and quasi-free nucleon-nucleon scattering (q.f.s.).
- (ii) A quantitative description of the data by approximate solutions of the exact three-body theory.
- (iii) The determination of nucleon-nucleon scattering parameters.

The advantage of the nucleon and deuteron three-body reaction is its ability to provide the comparison of the three charge states of the nucleon-nucleon  ${}^1S_0$  scattering under equal conditions in the form of  $n+d \rightarrow n+n+p$  or  $p+d \rightarrow p+p+n$  break-up. The presence of the three particle framework in the study of the nucleon-nucleon subsystem is not such a disadvantage since the exact three-body theory (Fa-61) and its solutions (Lo-64, Eb-72) have been developed. On the contrary, the study of the three-body system can reveal new information regarding details of the two-particle interactions, which cannot be readily observed in the study





of the two-body system. In particular the short range behaviour of the nuclear force, the off-shell effects and, in addition, the possible existence of the three-body force (Br-74) can be studied in the three-body system.

#### A.2.1 Kinematics of Three-Particle Reactions and the Differential Cross Section

We consider reactions of the following form:

$$0 + t \rightarrow 1 + 2 + 3$$

The nine scalar momentum components of the final state completely specify the kinematics of the system. Four components can be eliminated by applying conservation of energy and momentum. Thus the measurement of five independent scalar variables suffices.

In coincidence experiments, two of the particles (by our convention, particles 1 and 2) are detected at fixed angles. Thus six scalar variables are measured: the beam energy, two final-state particle energies, two angles with respect to the beam axis, and the azimuthal angle between the two detected particles. This constitutes a kinematic over specification of the system, which is useful in reducing background. Conservation of energy and momentum restricts the energies of the two detected particles to values given by the following equation:



$$\begin{aligned}
Q = & (1 + m_1/m_3)E_1 + (1 + m_2/m_3)E_2 - \\
& (1 - m_0/m_3)E_0 - 2\cos \theta_1 [(m_1 m_0/m_3^2)E_0 E_1]^{1/2} \\
& - 2\cos \theta_2 [(m_2 m_0/m_3^2)E_0 E_2]^{1/2} \\
& + 2\cos \theta_1 [(m_1 m_2/m_3^2)E_1 E_2]^{1/2}
\end{aligned} \tag{A-13}$$

where  $\cos \theta_{12} = \cos \theta_1 \cos \theta_2 + \sin \theta_1 \sin \theta_2 \cos (\psi_1 - \psi_2)$

The  $\theta_i$ ,  $\psi_i$ ,  $m_i$  and  $E_i$  are the polar angles, azimuthal angles, masses, and energies of particle  $i$ ;  $Q$  is the  $Q$ -value of the reaction. This is the equation of a fourth-degree curve in the  $E_1$ - $E_2$  experimental space (indicated as dotted and solid curves in the two-dimensional plots of Chapter C). Particle 3 is free to assume various momenta consistent with each  $E_1$ ,  $E_2$  solution of Eq. (A-13). Each point on the  $E_2 = f(E_1)$  curve corresponds to a definite relative energy between each pair of particles. The occurrence of a resonance at a particular relative energy results in an enhancement over the normal phase space or a peak in the three-body cross section at the appropriate point on the  $E_2 = f(E_1)$  curve. An experiment at fixed angles and fixed incident energy may contain several peaks corresponding to resonances at various internal relative energies (Figs. C.5.4, C.5.5).

The intensity distribution  $I(s, \Omega_1, \Omega_2)$  along the curve contains the full physical information. The experimen-



tal data are optimally analysed in terms of the arc length  $s(E_1, E_2)$  along this curve. The differential cross section is expressed by

$$\frac{d^5\sigma}{ds d\Omega_1 d\Omega_2} = \frac{2\pi}{h v_0} |T_{fi}|^2 \rho_s, \quad (A-14)$$

with the projectile velocity  $v_0$ , the transition amplitude  $T_{fi}$  and the phase space factor

$$\rho_s = \frac{m_1^2 m_2^2 v_1 v_2}{\left\{ \left(1 - \frac{v_3 \cdot v_2}{v_2^2}\right)^2 + \left(1 + \frac{v_3 \cdot v_1}{v_1^2}\right)^2 \right\}^{1/2}} \quad (A-15)$$

(including the particle masses  $m_1$ ,  $m_2$  and velocities  $v_1$ ,  $v_2$ ,  $v_3$ ).

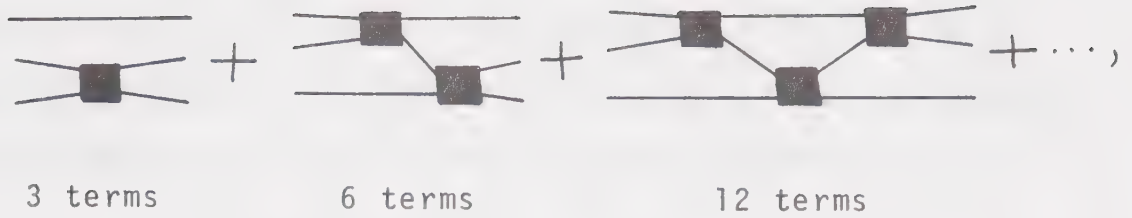
#### A.2.2 Transition Amplitude $T_{fi}$ - The Exact Three Body Formalism

Exact equations for the three-body transition amplitude were first given by Faddeev (Fa-61). He expressed the three-body transition operator formally as a multiple scattering series

$$T = \sum_{i=1}^3 t_i + \sum_{j \neq i} t_j G_0 t_i + \sum_{k \neq j \neq i} t_k G_0 t_j G_0 t_i + \dots \quad (A-17)$$

where  $G_0$  is the free-particle propagator. Diagrammatically:





Here  $t$  is a two-particle transition operator and the two-particle transition amplitude from a state of two particles with a relative momentum  $p$  to a state with relative momentum  $p'$  would be  $\langle p' | t(\epsilon) | p \rangle$ . Here  $\epsilon$  is the two-particle relative energy. If the two-particle bound state or a resonance exist the transition amplitude can be divided into a separable part ( $t^S$ ), which contains the pole at the bound state energy  $\epsilon = -\kappa^2$  or a sharp peak at  $\epsilon = 0$ , and the rest without any pole behaviour as:

$$\begin{aligned} \langle p' | t(\epsilon) | p \rangle &= \langle p' | t^S + t^{\text{rest}} | p \rangle \\ &= g(p') \tau(\epsilon) g(p) + \text{rest}(p', p, \epsilon) \end{aligned} \quad (\text{A-18})$$

Here  $g(p)$  are form factors and  $\tau(\epsilon)$  is a function carrying the pole behaviour in the relative energy of the two particles  $\epsilon$ . This can be diagrammatically symbolized as:

$$\text{[Diagram: Black square vertex]} = \text{[Diagram: Two white circle vertices connected by two lines]} + \text{[Diagram: Single vertex with four external lines]} \quad (\text{A-18a})$$





For a separable potential of Yamaguchi (Ya-54) type  $v(p',p) = \lambda g(p')g(p)$ , the remainder of Eq. (A-18) is identically zero. The Yamaguchi form factors are connected to the scattering length  $a$  and the effective range  $r_0$  by

$$\begin{aligned} g(p) &= N/(p^2 + \beta^2) \\ -\lambda N^2 &= \beta(\beta + \kappa)/\pi^2 \end{aligned} \quad (\text{A-19})$$

$$(\kappa + \beta)^2 (r_0 \beta - 1) - 2\beta^2 = 0$$



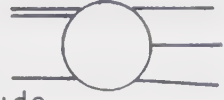
$$(\kappa - \frac{1}{2} r_0 \kappa^2) = \frac{1}{a}$$

Solutions of the Faddeev equations (A-17) with local nucleon-nucleon potentials are not available for the break-up reaction, whereas a separable potential expansion (Lo-64), especially in the reformulation of the Faddeev equations by Sandhas et al., (Sa-67) has led to numerical calculations of the absolute differential cross section, (Ca-71, 72; Eb-72).

The solvable coupled integral equations for the breakup transition amplitude in the Sandhas' rearrangement, for separable potentials only, can be expressed by the following diagram:

$$\text{Diagram (A-20)}: \text{A circle with two incoming lines labeled } i \text{ and two outgoing lines} = \sum_{i \neq j} \text{Diagram 1} + \sum_{i \neq j} \text{Diagram 2} \quad (\text{A-20})$$



where  and  are defined by (A-18a) and  symbolizes the breakup transition amplitude.

The solution of integral "equation" (A-20) by Ebenhöh (Eb-72), the theoretical predictions of which were used in this work, has been obtained with the following important restrictions to the three-particle interaction:

- (i) Only two-particle S-wave interactions in triplet and singlet states of the two-nucleon subsystems are taken into account.
- (ii) The Coulomb repulsion of the p-p subsystem is not included (it, however, does not appear in the  $d(n,2n)p$  reaction).
- (iii) Separable potentials of Yamaguchi type fitted to low-energy effective range parameters are used to solve the coupled integral equations numerically.

### A.2.3 Previous Studies of Deuteron Break Up Reactions

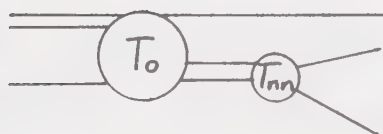
So far, experimental studies of three-nucleon breakup reactions have shown enhanced differential cross sections for certain kinematical situations only, namely for a small relative energy  $E_{NN}$  of any two nucleons (Final State Interaction) and for a minimum momentum transfer to one nucleon bound in the deuteron (Quasi-Free Scattering). Most of the experimental studies of deuteron breakup reac-



tions performed up to date concentrated on these semi two-body effects under kinematical conditions, where they would dominate the breakup and give enhanced cross sections.

#### A.2.3.1 Final state interactions

Under kinematical conditions where two outgoing nucleons from the breakup have small relative energy while their energy with respect to the third particle is large, or if the third particle cannot effect the interaction of the first two particles in the final state, the breakup transition amplitude is fully dominated by the two-particle interaction. In the approximation of the Watson-Migdal model (Wa-52, Mi-55) the probability of all but one two-particle final state is neglected and the transition amplitude is expressed by the sequence (e.g., in  $n + d \rightarrow n + n + p$ )



(A-21)

where the production amplitude  $T_0$  is assumed constant for fixed angles of detection and  $T_{nn}$  has a pole behaviour at the  $p_{nn}=0$  relative momentum. This reflects in factorization of the cross section as





$$\frac{d^5\sigma}{dE d\Omega_1 d\Omega_2} \sim |T_0|^2 B_W(p_{nn}) \rho_E \quad (A-22)$$

where

$$B_W(p) = \frac{1}{(-1/a + 1/2 r_0 p^2)^2 + p^2}$$

is an enhancement factor. As a f.s.i. dominates the breakup process very strongly under appropriate kinematic conditions there is relatively little deviation between the values of the scattering length  $a$ , as deduced from experiments by "exact" calculations and those obtained with the W.M. approximation (Bo-69). While the experiments reproduce the established value of  $a_{np}$  and the Coulomb corrected  $a_{pp}$ , there existed large discrepancies in the earlier, so called kinematically, incomplete experiments in the value obtained for  $a_{nn}$  (Sh-73 references in there). These experiments did not collect enough kinematical variables for a complete definition of the breakup. Instead, they detected one particle, analysing a forward direction peak in its angular distribution. This corresponded to the case where all available kinetic energy is transferred to this particle, leaving the remaining two with zero absolute and thus also zero relative energy. Approximate solution methods, like Born Approximation and W.M. model, used in the analysis of these experiments before the advent of the "exact" calculations, proved inadequate to cope with the interference of many effects involved in such reactions. The  $a_{nn}$  values obtained vary from -13 F to -25 F.



The results of more recent, kinematically complete, experiments (Eg., Ze-70, 72) cluster in the range between  $a_{nn} = -14.5 \text{ F}$  to  $-18.0 \text{ F}$ . The summary of these experiments by Vranic et al. (Vr-74) assigns the nn effective range parameter values to  $a_{nn} = -16.4 \pm 0.9 \text{ F}$ ,  $r_{nn} = 3.4 \pm 0.6 \text{ F}$ . The kinematically complete experiment which is best satisfying the assumptions of the W.-M. approximation is the reaction  $\pi^- + d \rightarrow \gamma + 2n$ . This has been studied by Haddock et al. (Ha-65). The result, corrected by Nygren (Ny-68), was  $a_{nn} = -18.42 \pm 1.53 \text{ F}$ . The analyses of f.s.i. experiments appear to be rather insensitive to the effective range  $r_{nn}$  and its value is usually taken as equal to  $r_{pp}$  (2.8 F) in calculations.

#### A.2.3.2 Quasi free scattering in the deuteron break up

At high incident nucleon kinetic energies ( $\gtrsim 100 \text{ MeV}$ ), where the Compton wavelength of the bombarding nucleon is small enough to resolve the two nucleons bound in the deuteron, quasi-free scattering can simply be explained as almost-free scattering of two of the three nucleons involved in the deuteron break up, under kinematic conditions where the "spectator" particle is left without any share of the available kinetic energy. This explanation, however, is not so applicable at low energies ( $\sim 10\text{-}30 \text{ MeV}$ ) where the deuteron binding energy of 2.225 MeV is not negligible. The effect spreads into a coherent contribution of a number of coupled



multiple scattering terms in the three-body transition matrix which involve interactions of all the three nucleons. In any case, a broad enhancement peak is observed in the low energy deuteron breakup at the geometry, which corresponds to the quasi-free scattering, and the process retains predominance of the on-shell two-body scattering.

The semi-two-nucleon kinematics, perturbed by the binding of the spectator nucleon in the deuteron, changes the laboratory angle between the scattered nucleons from  $\sim 90^\circ$  (which would correspond to a free two-nucleon scattering) to a slightly smaller angle, depending on the ratio of the C.M. energy to the deuteron binding energy. Typically, the geometry of the quasi-free scattering at  $\sim 20$  MeV incident nucleon energy in the laboratory system is  $\theta_1 = 41.5^\circ$ ,  $\theta_2 = -41.5^\circ$  for the two outgoing nucleon scattering angles in the laboratory system.

The multiple scattering contributions involved in the low energy q.f.s. extend the dominance of this effect both onto a large range of scattering angles around the pure q.f.s. geometry as well as onto a large region, along the kinematical locus  $E_2=f(E_1)$ , corresponding to one particular q.f.s. geometry.

The study of q.f.s. has mostly been done for the  $D(p,2p)n$  reaction in a broad range of bombarding energies (4.5 - 60 MeV; Va-71, Du-71, Pe-70). The broad peak due to



the p-p q.f.s. observed in these experiments is reproduced, in general, satisfactorily by the "exact" theoretical predictions, unlike the calculations based on the plane-wave impulse approximation (Ku-61) and the modified simple impulse approximation (Br-71, Ma-70, Mc-71) which failed to predict the amplitude and shape, and the amplitude of the cross section peak respectively. However, unlike the study of f.s.i., many significant discrepancies were observed between the "exact" theory prediction and the experiment in the p-p q.f.s. For example, Klein et al., who examined the  $D(p,2p)n$  break up at 16 keV incident proton energy and several experimental geometries where both the f.s.i. peaks as well as the q.f.s. peak appeared on the same locus curve, found a systematic overprediction up to 30%, of the q.f.s. peak magnitude by the Ebenhöf code.

A whole summary of disagreements observed between the theory and experiments in the  $D(p,2p)n$  q.f.s. is given in the paper of Anzelton et al. (An-72). It is found, in their work, that this disagreement (up to 80%) is a function of incident energy and the C.M. angle. The largest discrepancy is found at 23 MeV bombarding energy.

Theoretical studies of Brayshaw (Br-74) and a thorough analysis of Petersen et al. (Pe-74) find that q.f.s. shows very little sensitivity to off-shell properties of the two-nucleon potential. Consequently, speculations were made





(Br-74, An-72, Kl-73, Ma-71) that the existing disagreement is due to inadequate subtraction of the Coulomb effect in the p-p interaction and due to the lack of inclusion of higher partial waves  $L > 0$  (only s wave potentials included) in the theoretical calculations.

The unanimous conclusion of all these studies is the call for an accurate  $D(n,2n)p$  q.f.s. experiment where the Coulomb effect ambiguities are absent. Suggested are n-n q.f.s. experiments at energies and geometries of the largest observed p-p q.f.s. disagreements (An-72). Studies of assymmetric q.f.s. scattering angles are suggested as particularly sensitive to the higher partial wave effects (Ma-71).

Since the q.f.s. was found to be insensitive to off-shell effects it can be used to determine the on-shell parameters of the nucleon-nucleon potential, i.e., the scattering length and the effective range. An interesting analysis in this direction was made by Vranic et al. (Vr-74) who found that, while the sensitivity of q.f.s. to the scattering length is poor, it is very sensitive to the effective range variations. Since this situation is reversed in the f.s.i. experiments, a conclusion could be drawn, that  $a_{nn}$  value should be deduced from f.s.i. experiments while the effective range  $r_{nn}$  could best be obtained from q.f.s. experiments.



Only two  $D(n,2n)p$  kinematically complete q.f.s. experiments have been made up to date (Sl-71, Fo-74). Both of these experiments were performed at 14 MeV incident energy and  $30^\circ$ ,  $-30^\circ$  q.f.s. geometry. The latter, (Fo-74) added a  $40^\circ$ ,  $-40^\circ$  scattering geometry. Unfortunately, due to the difficulties involved in the n-n quasi-free scattering experiments (see Part B), both studies contain large uncertainties, namely a statistical error of  $\sim 30\%$ , disallowing any significant conclusions.

In view of the experience summarized in this chapter we decided to study neutron neutron quasi-free scattering in a kinematically complete  $D(n,2n)p$  experiment at the incident neutron energy close to the "controversial" 23 MeV (the reason for choosing 21.5 MeV incident energy is explained in Chapter B.2.1). To study the effect of the higher partial waves, not included in the "exact" theory, we proposed to obtain an angular distribution of the q.f.s. cross section with the inclusion of assymmetric angle pairs.



## B. EXPERIMENTAL SYSTEM

### B.1 INTRODUCTION

The experimental setup used in the kinematically complete study of quasi-free scattering is shown in Fig. B.1.1. 21.5 MeV neutrons were used to bombard an array of three deuterated liquid scintillators (C6D6) which served as deuterium targets. The break-up proton from the  $D(n,2n)p$  reaction was stopped in the scintillator while the two outgoing neutrons were detected in two NE213 neutron detectors positioned at various angles with respect to the incident neutron direction.

Each of the three C6D6 detectors made a different pair of scattering angles with respect to the two shared neutron detectors. Thus three independent experimental geometries were run simultaneously in each run (utilizing more effectively the bombarding neutron flux). Runs were taken including assymetric QFS geometries (as shown in Fig. B.1.1) and later sets of symmetric geometries (see Fig. B.1.2).

A description of the individual components of the experimental setup as well as a more detailed description of the experimental geometry will be given in the next two chapters.





Figure B.1.1 Schematic diagram of the experimental set-up in Run #1 with indication of the eight parameters processed by the electronics in eight-fold coincidence.



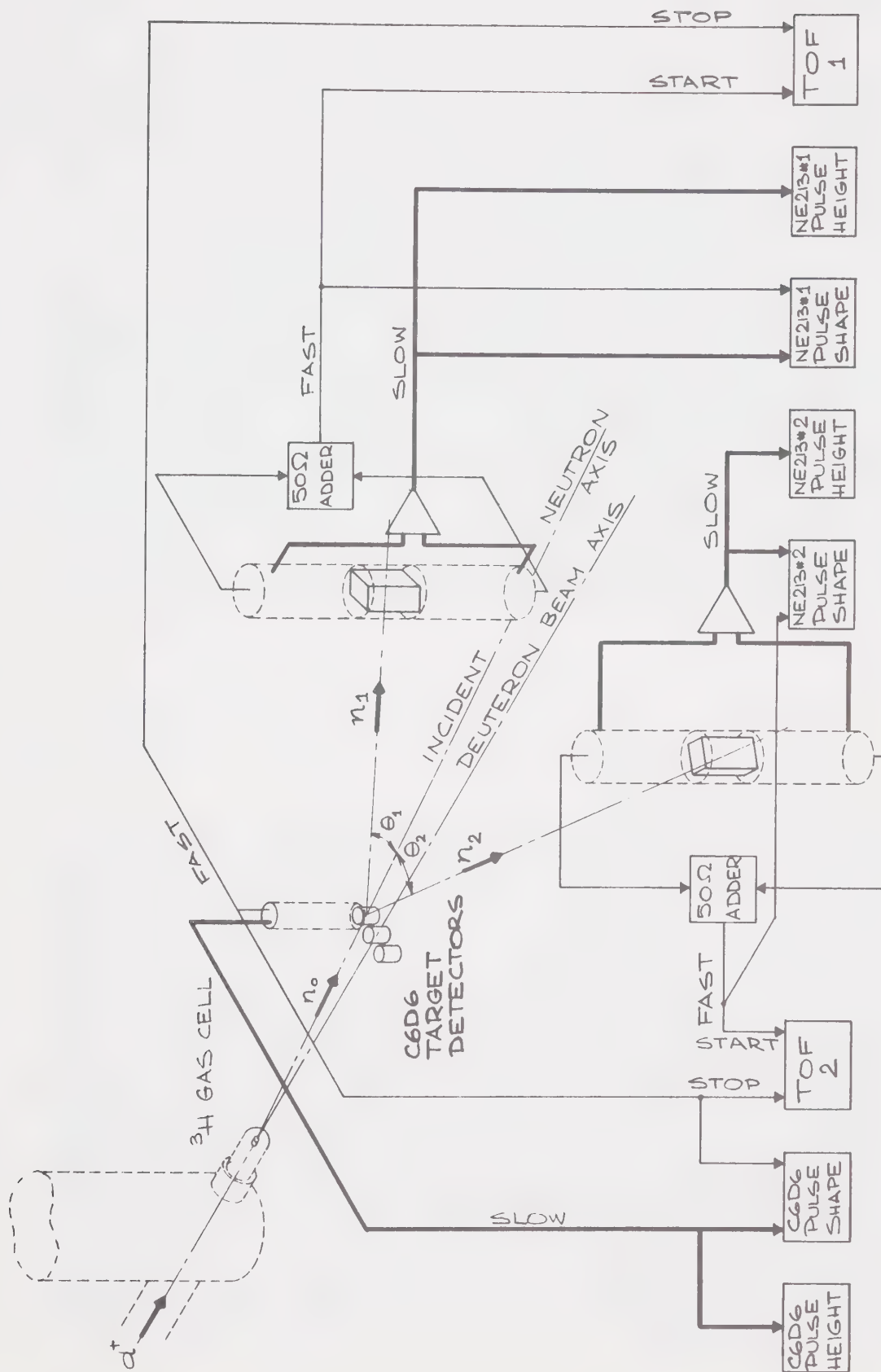
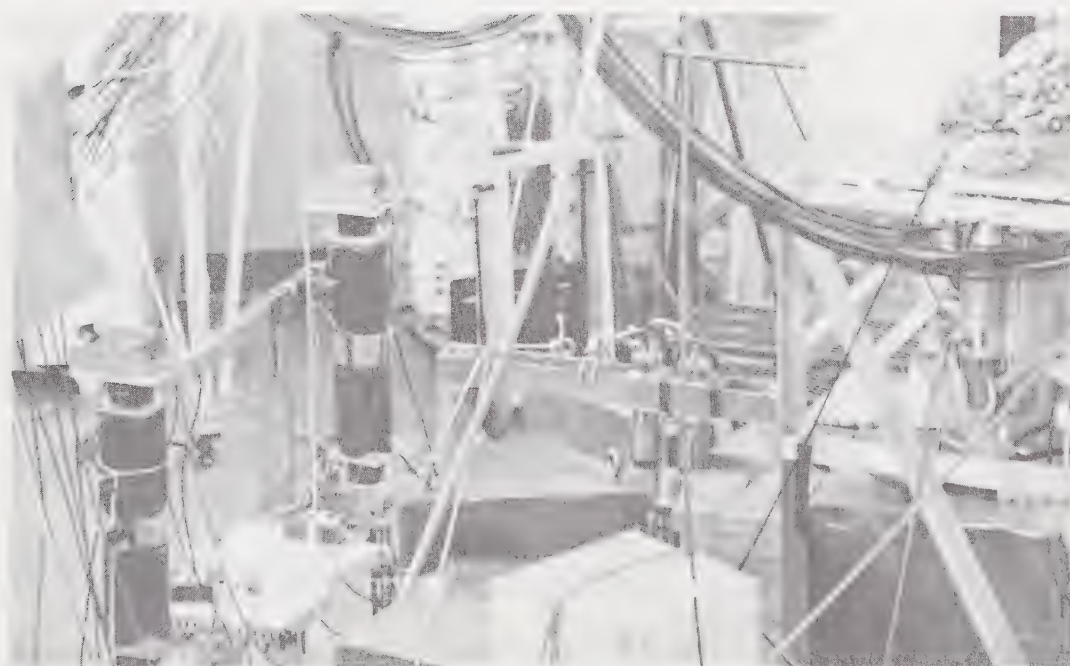






Figure B.1.2 A photograph of the symmetric quasi-free scattering geometry set up in Run #2.

Figure B.3.1.2 A photograph of the three C6D6 detectors (right center) and the two neutron detectors (left) mounted in their stands. (Run #2).





## B.2 THE FAST NEUTRON PRODUCTION FACILITY

A liquid nitrogen cooled tritium gas target facility, capable of producing  $4 \times 10^7$ /sr. sec fluxes of 23 MeV neutrons from the  ${}^3\text{H}(\text{d},\text{n}){}^4\text{He}$  reaction has been designed and commissioned as part of this project. The design, which will be described here was made to optimize the performance, safety, economy and reliability under the conditions existing in the Nuclear Physics Laboratory of the University of Alberta.

The demand for high energy (23 MeV) polarized neutrons, raised by proposals for a kinematically complete study of fast neutron induced break up of the Deuteron, as well as polarized fast neutron scattering experiments, using the University of Alberta 7 MeV Van de Graaff could only be met with the  ${}^3\text{H}(\text{d},\text{n}){}^4\text{He}$  reaction. The high positive Q-value of this reaction ( $Q = +17$  MeV) yields the required neutron energy (23 MeV with the use of a 6 MeV deuteron beam). This reaction, furthermore, gives high neutron polarization ( $P \simeq 0.50$  at  $30^\circ$  and  $P \simeq -0.50$  at  $90^\circ$ , see Wa-70).

### B.2.1 Description of the ${}^3\text{H}$ Target and Cryostat

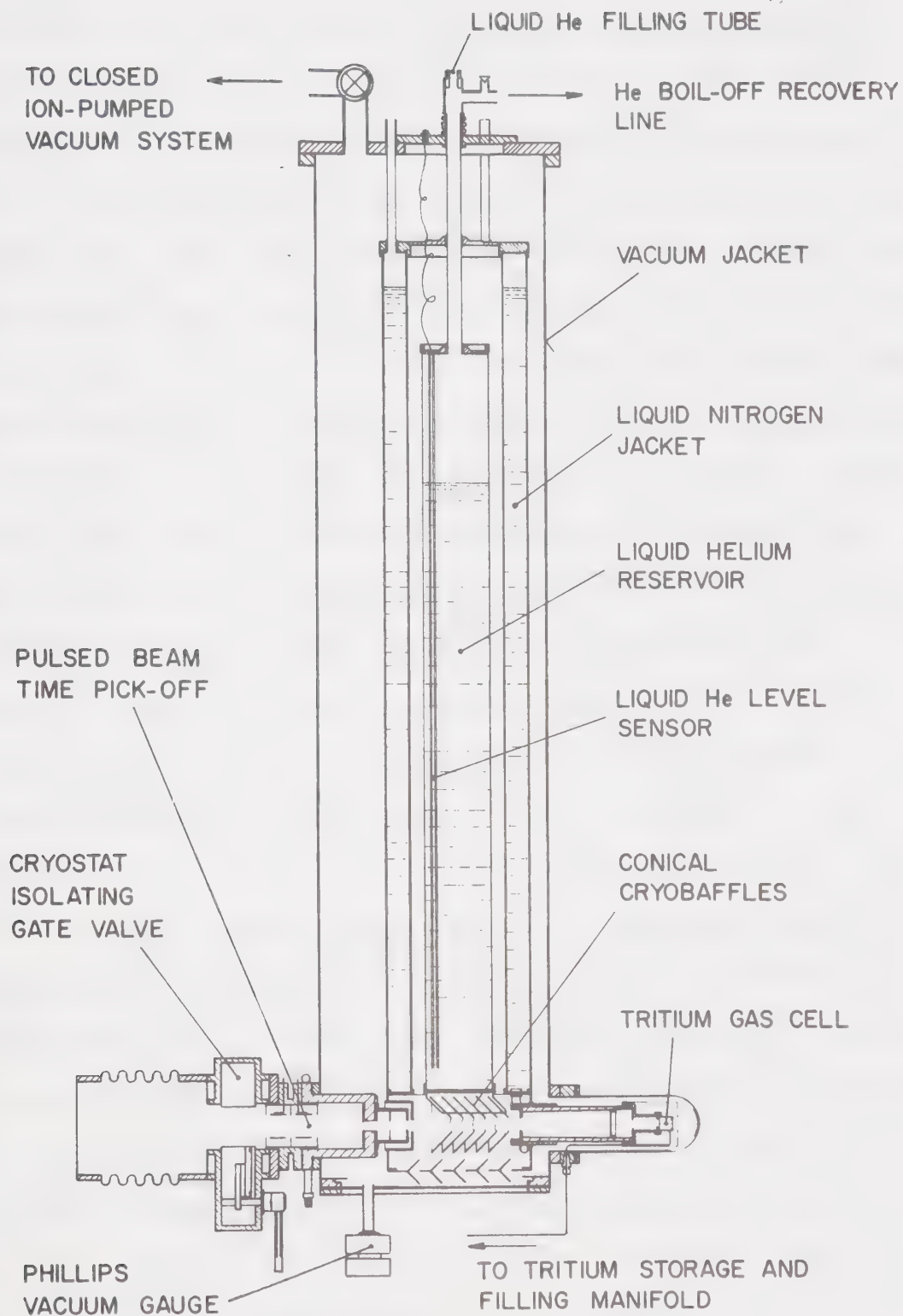
The relatively small thickness of the tritium target (about  $1.5 \text{ mg/cm}^2$ ), dictated by the low energy loss required for the low energy deuterons (5 to 6 MeV),







Figure B.2.1.1 Cross section of a cryostat designed to cool a  $1.5 \text{ mg/cm}^2$  tritium gas target to liquid nitrogen temperature and to provide safety against tritium gas leakage by means of a liquid helium cryopump.





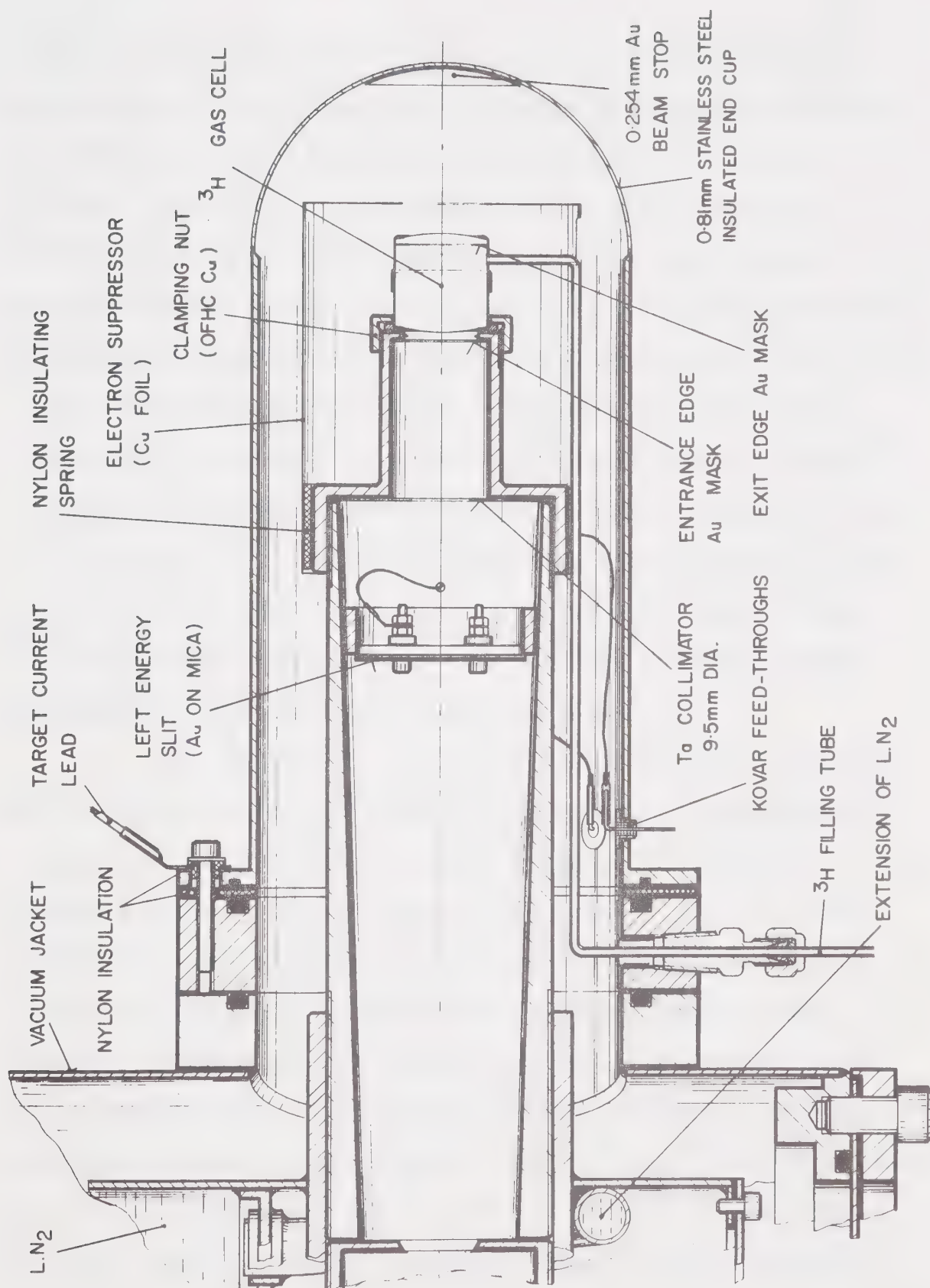
eliminated the possibility of using the tritium target in forms other than as a gas. The physical thickness of  $^3\text{H}$  solid or liquid corresponding to  $1.5 \text{ mg/cm}^2$  would be only about 0.07 mm which would be extremely difficult to maintain. However, the lower the temperature of the gas the lower its required pressure and the smaller the required length of the cell. The advantages of such a situation are obvious: lower gas pressure means increased safety against gas cell rupture; shorter target brings the target geometry closer to a point source. The compact size of the target is particularly important in the polarized neutron experiments where fast neutrons leaving the cell at  $30^\circ$  to the deuteron beam direction are used. The shorter passage of the slow deuterons through the gas also reduces the timing spread in the pulsed deuteron beam experiments. The  $^3\text{H}$  target of the FNPF consists of a cylindrical gas cell maintained at the liquid nitrogen temperature. The low temperature reduces the dimensions of the cell to 1.5 cm dia. x 1.5 cm length and the gas pressure to just below 1 ata to produce the required  $1.5 \text{ mg/cm}^2$  target thickness. To reduce the heat load on the cell, the deuteron beam is entered and also exited from the gas cell through 0.00525 mm Molybdenum windows. The deuterons were stopped on a gold lined beam stop beyond the cell (see Fig. B.2.1.2) depositing only  $\sim 0.7 \text{ W}$  of heat in the target. This arrangement allows a very efficient metal





Figure B.2.1.2 Detail of the tritium gas cell housing.







connection of the gas cell directly to a liquid nitrogen bath while the beam current is collected on an insulated end cup maintained at room temperature by an air jet on the outside. The body of the cell, made from 0.25 mm wall thickness stainless steel tube, consists of two halves bonded together after the two precisely punched Moly windows are epoxied into each half-cell from the inside and each half individually tested for leaks. The epoxy used in the construction of the cell is a high conductivity silver loaded epoxy (EPOTEC E-32). The back half of the cell has a 1.6 mm O.D. x 0.8 mm I.D. stainless steel capillary welded into the wall (see Fig. B.2.1.2) providing an uninterrupted  $^3\text{H}$  gas filling tube between the gas cell and the tritium storage and handling manifold (see Chapter B.2.2.1).

The entire gas cell is enclosed in the vacuum of a cryostat in which the liquid nitrogen bath, extended as a heat sink to the gas cell, functions as a radiation shield around a liquid Helium cryopump (see Fig. B.2.1.1). The presence of the cryopump provides a high degree of safety against tritium gas spreading beyond the volume of the cryostat in case of its leakage from the gas target. The cryopumping surfaces consist of series of conical copper baffles soldered to the bottom of the liquid Helium reservoir and are strategically positioned between the gas cell and the beam entrance to the cryostat. Any tritium, escaping



from the gas cell, would have to go around these surfaces before entering the beam line. The combined action of the baffles, the cryopumping and the large expansion volume of the cryostat (50ℓ) are calculated to shatter, stop and freeze the shock wave of Tritium resulting from possible gas cell window failure. Series of tantalum collimators and gold masks screen the cryopumping surfaces and all constrictions in the beam passage, between the entrance of the cryostat and the target, to avoid unwanted heat loads and background. The collimators are converging toward the target in keeping with the 3° horizontal focussing angle of the Mobley pulse compression system. The epoxied edges of the gas cell windows are masked with gold collimators, one being placed inside the cell (see Fig. B.2.1.2).

The cryostat is mounted on an independent structure which also supported the local shielding of water, lead and parafin. Mallory 2000 heavy metal collimators were placed around the neutron exit ports. The structure provides alignment of the cryostat on the beam line and contains a self explaining control panel for the sealed vacuum system, tritium manifold controls and automatic liquid nitrogen refilling controls. The beamline immediately in front of the cryostat contains a 400ℓ/sec ion pump and a system of vacuum baffles providing efficient differential pumping between the relatively poor vacuum  $\sim 10^{-6}$  Torr in the beam



line and the high vacuum in the cryostat  $\sim 10^{-8}$  Torr (see diagram in Appendix 1). This reduces both, the possibility of spreading the tritium into the beamline, as well as collection of mercury and hydrocarbons from the beamline on the cryopumping surfaces. The safety system, monitored by the interlock panel, and the fast acting valve are described in Appendix 1.

The cryogenic gas target facility had undergone a three year period of development and tests with hydrogen and deuterium gas before the tritium gas was finally introduced into the system. The tests included simulated gas cell ruptures and complete gas cell filling cycles. The functions of the cryopump were found excellent. The liquid He consumption rate with  $1.0 \mu\text{A}$  of beam, incident on the gas cell, is about  $0.25\text{L/hr}$ , in good agreement with the design calculations. The current gas cell has been found quite rugged. It has been bombarded by  $1 \mu\text{A}$  of 5 MeV deuteron beam for approximately 2160 hours to date, running for weeks at a time. The target was subjected to beam currents of up to  $4 \mu\text{A}$  and pressures up to 2 ata for short periods of time. Preliminary runs, to look at the neutron energy spectra as a function of incident deuteron energy, showed, that up to 5 MeV, most neutrons observed were due to  $d + {}^3\text{H}$  reactions. However, above  $E_d \approx 5$  MeV the reactions







start to produce copious amounts of low energy neutrons, in addition to those from  $d + {}^3\text{H} \rightarrow n + {}^4\text{He}$ . This is not a problem in elastic scattering experiments as detector biases are usually set well above these low energy neutrons. In our investigation of  $n + d \rightarrow n + n + p$  quasi-free scattering, however, it was necessary to have a very low bias in the C6D6 "target" scintillators. Therefore, to lower the countrate in these detectors, the deuteron beam energy had to be kept below 5 MeV. With 1 ata of  ${}^3\text{H}$  gas in the cell at 77°K the target thickness is about  $1.53 \text{ mg/cm}^2$ . This corresponds to about 80 keV energy loss for the 5 MeV deuterons in the gas up to the middle of the cell. With the inclusion of 300 keV beam energy reduction in the first Moly foil of the cell the reaction produced 21.5 MeV neutrons at zero degrees. A spectrum of 21.5 MeV neutrons obtained at 0° with the 5 MeV deuteron beam is shown in Fig. B.2.1.3.

The yield at zero degrees from the  ${}^3\text{H}(d,n){}^4\text{He}$  reaction is  $4 \times 10^7$  neutrons/sr.sec. At a laboratory angle of 30 degrees the yield decreases to about 60% of this value, and with  $E_d = 6.5 \text{ MeV}$  a polarization of the neutron beam  $P_n = 0.50$  is obtained.



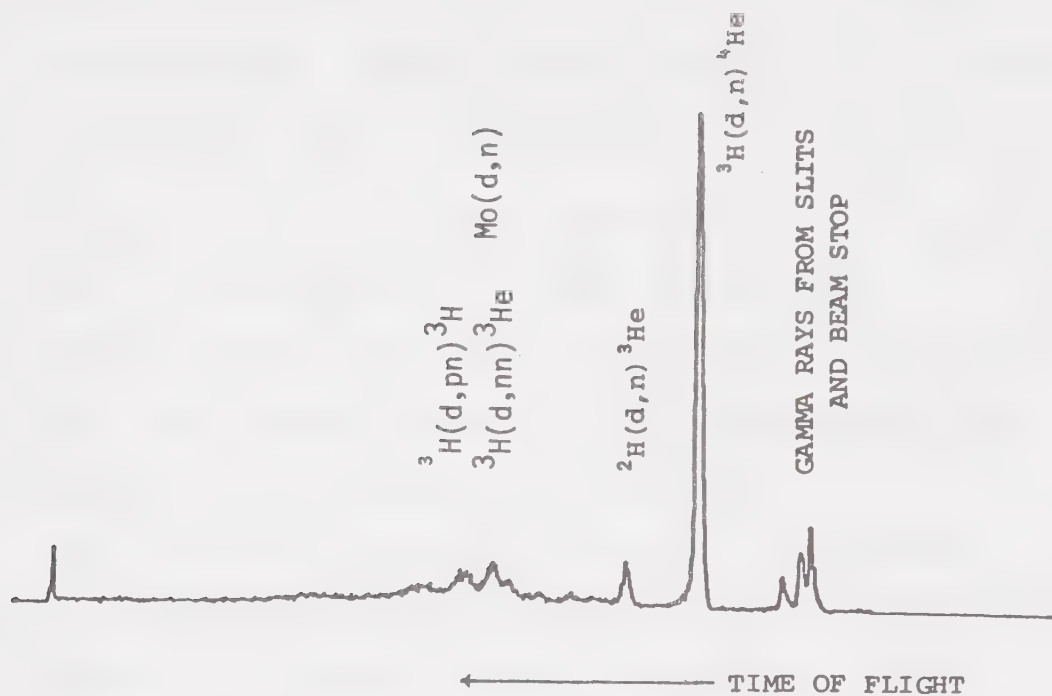


Figure B.2.1.3 Time-of-flight spectrum of direct neutrons at  $0^\circ$  produced by 6 MeV pulsed deuteron beam.



A set of energy slits, built into the cryostat just in front of the gas cell (Fig. B.2.1.2), with a feedback to the accelerator voltage control, proved very efficient in holding the beam steady on the target.

### B.2.2 Tritium Storage and Filling Manifold

A tritium storage and filling manifold was designed for the purpose of safe filling of the target with tritium gas to the needed pressure for the experimental run, and safe storage of the gas between experiments.

The tritium is normally contained in a storage furnace, in deoxydized uranium powder, to which the tritium is bound chemically, forming uranium tritide  $UT_3$ . This compound, stable at room temperature, breaks up completely at temperatures around  $450^{\circ}C$  (Ka-51, Ma-71). Thus heating the powder in the furnace to  $450^{\circ}C$  evolves the available tritium gas, on cooling the powder, the tritium is re-absorbed. This simple principle allows a pumpless closed connection between the storage furnace and the gas target.

The tritium manifold consists of two such furnaces (Fig. B.2.2.1). These are the working furnace #1 and the backup furnace #2 (for added absorption speed in case of failure) with individual seal-off valves #1 and #2 respectively. As the activated uranium can react very violently with oxygen and even nitrogen, and also to enable purification of the tritium, the two storage furnaces are

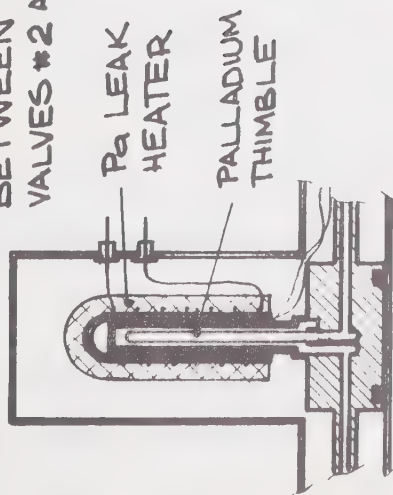




Figure B.2.2.1 Cross section of the tritium storage and handling manifold.



# VERTICAL SECTION THROUGH Pa LEAK BETWEEN VALVES #2 AND #5



STAINLESS STEEL - CERAMIC  
THERMOCOUPLE VACUUM GAUGE  
(RANGE UP TO 20mm Hg)

FRESH  
SUPPLY  
PORT

Pa LEAK  
HEATER  
PALLADIUM  
THIMBLE

Fe - CONST.  
THERMOCOUPLE  
JUNCTION

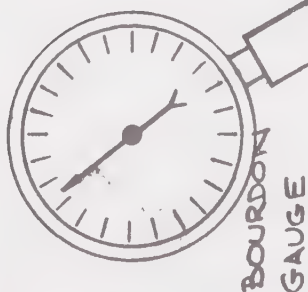
TO MONITORED  
VACUUM PUMP

FURNACE HEATER

PYREX  
WOOL

2mg OF  
URANIUM  
POWDER

TO SEALED  
VACUUM SYSTEM



BOURDON  
GAUGE

GAS CELL  
FILLING  
TUBE



separated from the rest of the manifold by a palladium leak which, when heated, lets only hydrogen isotopes diffuse through. There is also a provision for the bypass of the leak by opening valve #3 and the bypass valve #4 (Fig. B.2.2.1).

The manifold contains three additional branches with their valves:

Valve #5 - gas target port with a Bourdon combined range vacuum-pressure gauge.

Valve #6 - connection to a vacuum pump and a leak detector.

Valve #3 - fresh gas supply port to load the manifold and, in connection with valve #4, a bypass of the palladium leak.

There are two heater elements; one for the uranium furnace and a second for the palladium leak. The furnace heater can be moved from one furnace to the other, as needed. Both furnaces and the palladium leak have thermocouples to determine the temperature.

Uranium powder is held in the ends of the inner 1/4" bores of the stainless steel furnaces by pyrex wool preventing the particles from travelling beyond the reach of the furnace heater. The wool also efficiently fills the dead space of the furnace, thus reducing the amount of tritium, necessary in the system to fill the gas cell to the required pressure.



The entire inner volume of the manifold was minimized to limit the necessary amount of tritium. Most inner passages have 1.6 mm inner diameter while the filling capillary, connecting the manifold to the gas cell, has 0.8 mm inner bore. This does not seriously impede the gas transfer processes as compared to the relatively slow rate of absorption and release of the gas. All vessels, which contain tritium in any stage of tritium transfer between the storage furnaces and the gas cell, including the connection from the manifold to the gas cell (plastic tube sheath) are double walled (and ports double closed) with the intermediate space either evacuated or vented and monitored for tritium leaks. The entire manifold is enclosed in its own compact fume hood (its outer stainless steel case). This is evacuated and tritium leak monitored. The hand knobs of the six all stainless steel welded bellows valves are protruding outside the case (vacuum sealed through the bottom) for ease and simplicity of operation (see Fig. B.2.2.2).

The manifold docks into a holding mechanism at the bottom of the cryostat (see Fig. B.2.2.3) and can be moved with the cryostat as one unit off the beamline, without breaking the filling tube connection, or can be removed and stored separately for other operations (So-73).



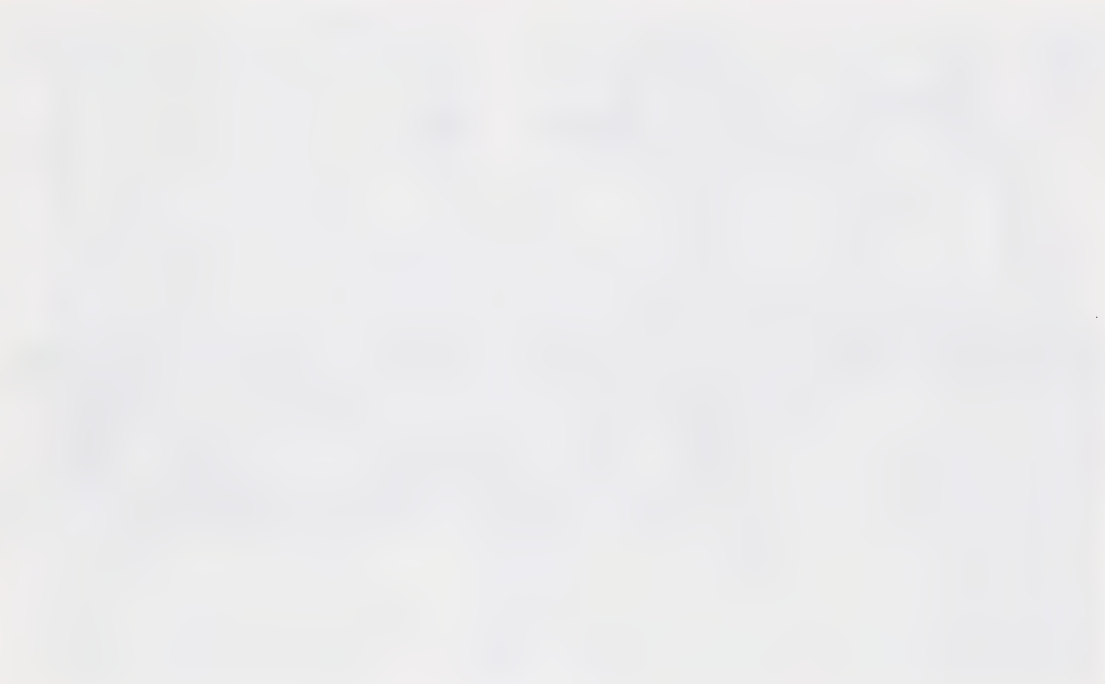
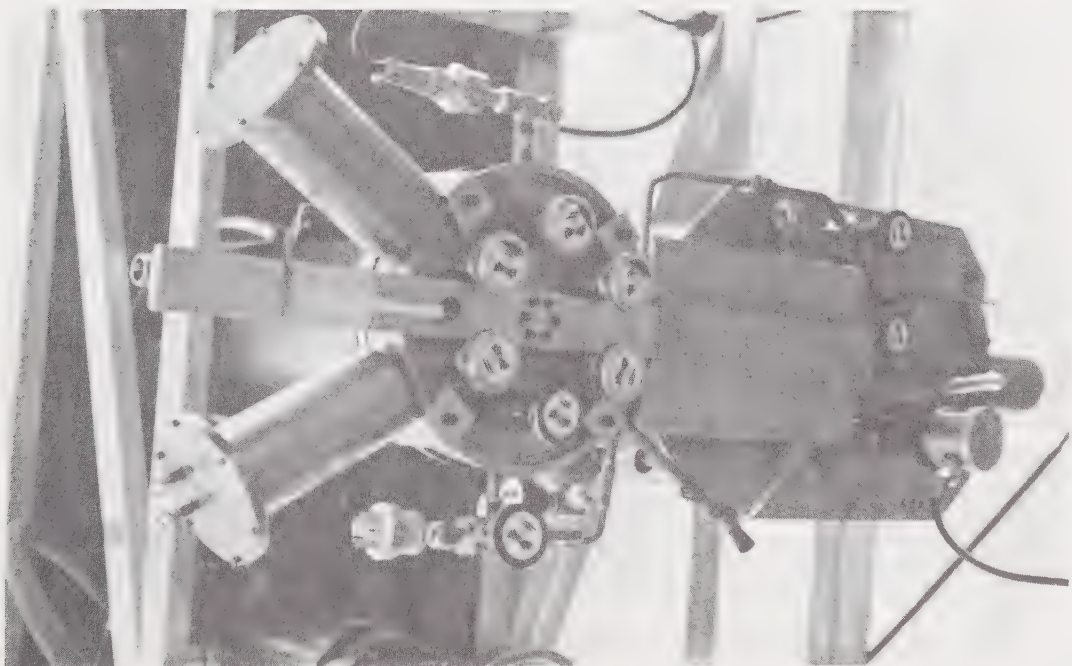
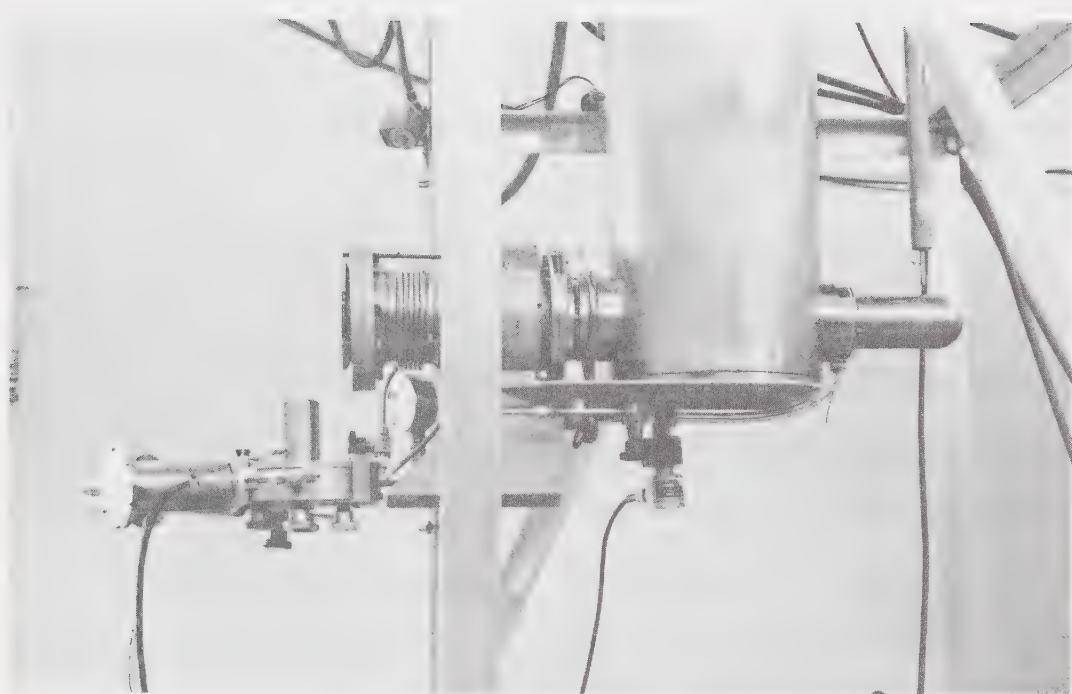


Figure B.2.2.3 Side view of the FNPF cryostat off beam-line with the tritium storage and handling manifold mounted at the bottom of the cryostat and connected to the gas cell inside the cryostat by a continuous stainless steel capillary (sheathed with plastic tube).

Figure B.2.2.2 Bottom view of the tritium storage and handling manifold.







The tritium furnaces had been flushed with hydrogen gas (many times repeated absorption and release of hydrogen from the uranium powder) before tritium was loaded into furnace #1. This process is necessary to clean the surface of active uranium and improve the gas release and absorption rates.

The use of the palladium leak had to be terminated after many cycles due to its gradual contamination and eventual impermeability. This effect is well known and described in literature (Da-64). Allegedly, it could be avoided by the use of 23% silver-palladium alloy instead of pure palladium. The palladium leak bypass (valves #3 and #4) is presently being used in the tritium transfer processes.

The system has been used for at least 100 fillings of the target to date and found very satisfactory. The time required to fill the cell to 1 ata is about one hour. The reabsorption time is only  $\sim 15$  min.



### B.3 DETECTORS AND GEOMETRY

Two kinds of detectors were used in the kinematically complete study of the  $D(n,2n)p$  breakup.

(1) C6D6 liquid scintillators (NE230) were used as deuterium targets.

(2) NE213 liquid scintillators were used to detect neutrons following the breakup.

#### B.3.1 Study of the C6D6 Scintillator; Pulse Shape Discrimination

As mentioned earlier, five kinematical variables fully define a kinematically complete three-body breakup event. Thus, knowing the incident neutron energy, the directions of the two breakup neutrons and the energy of one of them should be sufficient for a kinematically complete  $D(n,2n)p$  experiment. However, the count rate in this type of experiment, being proportional to the product of two nuclear crosssections ( $^3\text{H}(d,n)^4\text{He}$  and  $D(n,2n)p$ ) is very low and random coincidences are a serious problem. Overspecification of the three-body event by collecting additional parameters then becomes useful in separation of true events from the random background.

Use of the deuterated scintillator as the deuterium target allowed detecting of the recoil proton and obtaining its recoil energy and a fast timing signal for the neutron time-of-flight measurement.



The two deuterated liquid scintillators available today are NE230 on deuterated benzene basis ( $C_6D_6$ ) and NE232 on deuterated cyclohexane basis ( $C_6D_{12}$ ). Earlier studies reported excellent pulse shape discrimination properties of NE230 (Bo-72) and a higher light output than NE232 scintillator. Although, the latter has a higher ratio of deuterons to carbon atoms in a unit volume, the importance of higher light output and better pulse shape discrimination resulted in the choice of NE230 scintillators as targets.

A thorough study of the pulse shape properties of the  $C_6D_6$  scintillator was made (So-74) prior to the proposed deuteron breakup experiments to investigate the possibility of discriminating different neutron induced interactions in the liquid in addition to the basic neutron-gamma ray discrimination.

Liquid organic scintillators are normally used to allow the identifications of neutrons and gamma rays. A charged particle, produced in the scintillator by the neutron or gamma ray causes emission of light quanta by the atoms along its path by means of excitation and ionization of their electron levels. The light produced is converted into a stream of electrons on a photocathode, optically coupled to the scintillator, and multiplied into an electronic pulse by a photomultiplier. The amplitude of the produced light pulse, in relation to the energy of the charged particle, and its





time characteristics depends on the history of its production in the scintillator. A light charged particle, like electrons, mostly excites the electrons bound in the surrounding molecules and their prompt deexcitation produces light with the wavelength in the range of sensitivity of the photocathode. Heavier nuclear particles, on the other hand, produce a great deal of complete ionization of the surrounding molecules and the light conversion on the photocathode depends correspondingly on the effect of wavelength shifting additives in the scintillator. These complex organic molecules break up the more energetic ultraviolet quanta, produced by recombination of ions, into several softer ("visible to photocathode") quanta through their own decomposition and recombination. Such light response arrives relatively later and its production is less efficient, as part of the energy is always lost in the wavelength conversion process. The proportion of the slower and less efficient component of the light response is thus higher, the heavier and slower the particle and the higher its density of ionization. The charged particles, available for the conversion of a neutron or a gamma ray interaction into a light pulse in most liquid organic scintillators, are given by the chemical composition of the scintillator. Consisting almost exclusively of Hydrogen and carbon, their interaction with the gamma ray is by the Compton effect (electron) and the neutron interaction is mostly by n-p



elastic scattering with only small contributions from n-C nuclear processes up to about 20 MeV neutron energy. The heavily ionizing Carbon is inefficient in production of light and the energy of its lighter breakup fragments like  $\alpha$  particles is reduced by the Q-value and by the multiple sharing of the kinetic energy.

The proton is replaced by a deuteron in the deuterated scintillator and thus two light producing particles detect the neutron interaction. In addition to the recoil deuteron from n-d elastic scattering it is also the proton, produced in the inelastic n-d breakup.

The decay time of the fast component of the light response in the liquid organic scintillators is about 6 nsec while the slow part typically decays in 200-400 nsec. For recoil protons produced in the scintillator by neutrons the amplitude of the slow component is about 2% of the fast components, whereas for electrons produced by gamma rays the slow component is only about 1% as large as the fast component. The corresponding subtle difference in the shape of the electronic pulse derived from such superposition of the fast and slow components is magnified by a suitable pulse shape discrimination circuit and used to distinguish the gamma and neutron induced events in the scintillator.

Several pulse shape discrimination circuits were tested with the C<sub>6</sub>D<sub>6</sub> scintillator (So-74). The selection used in this project is shown in Fig. B.4.4. A 5 cm x 3.8 cm



dia. NE230 scintillator was mounted on an RCA8575 photomultiplier tube coupled to an ORTEC270 tube base. The zero-crossing time of the doubly differentiated linear signal, with respect to the delayed fast timing output of the detector as the reference time, was converted into an analog pulse in a time-to-amplitude converter (TAC). Its amplitude is the measure of the rise time of the linear pulse and is called Pulse Shape signal in this work. At the same time, the singly differentiated linear pulse, the amplitude of which is the measure of the charged particle recoil energy in the scintillator, was collected in coincidence with the pulse shape. The two parameters were displayed as a 64 x 64 channel two-dimensional histogram by the Honeywell 516 on-line computer.

The tests were performed with a Pu-Be neutron source and the monoenergetic 23 MeV neutrons from the  $^3\text{H}(d,n)^4\text{He}$  reaction. The countrate effect on the pulse shape discrimination was studied by adding radiation sources close to the detector. Reliable n- $\gamma$  pulse shape discrimination was obtained up to 100 KHz. A two dimensional, 64 x 64 channel, energy versus pulse shape plot displaying only the pulse shape ridge corresponding to the neutron interactions with the atoms of the C6D6 scintillator is displayed in Fig. B.3.1.1. The energy of the recoil particle runs from the bias of 130 keV Compton electrons at the top of the plot





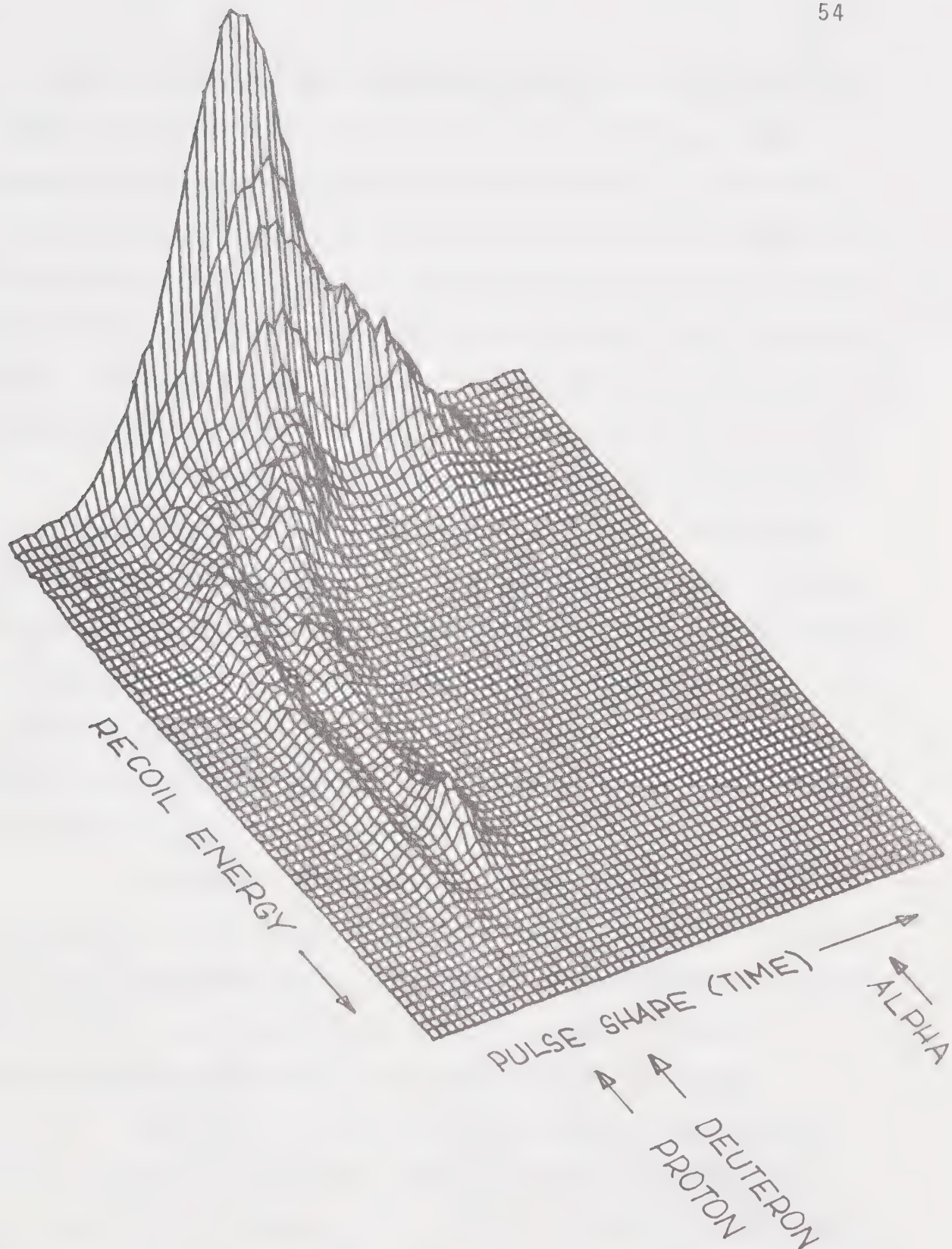


Figure B.3.1.1 Recoil energy and pulse shape from 23 MeV neutron induced interactions only in NE230 scintillator.





to the maximum neutron energy of 23 MeV from the  ${}^3\text{H}(\text{d},\text{n}){}^4\text{He}$  reaction at the bottom of the picture. By moving the gamma ridge off scale on the left it was also possible to identify the splitting of the neutron interaction ridge into the  $\text{D}(\text{n},2\text{n})\text{p}$  breakup ridge (PROTON) and the deuteron ridge (DEUTERON), terminated by the characteristic back scattering peak. Further on the right is the alpha-particle ridge (ALPHA) from the inelastic n-C interactions.

The experience gained in the study of the C6D6 pulse shape properties gave confidence in the use of this detector to obtain two additional parameters useful in the examination of the n-d breakup. These are the breakup proton energy and the pulse shape. The proton energy and its direction are defined exactly in the kinematically complete experiment and a window can thus be set on the C6D6 energy parameter around the calculated value.

Although, the pulse shape was limited to n- $\gamma$  discrimination in the quasi-free scattering region, as the resolution becomes poor at extremely low energies, it would be useful in eliminating extraneous events at other n-d breakup geometries where the proton energy is higher.

For really sensitive pulse shape discrimination, such as needed to separate recoil protons and deuterons, one must use two dimensional display of energy versus pulse shape. Adjusting the walk on the zero-crossing discriminator



(TSCA) for pulse shape allows one to adjust the particle ridges parallel with the energy axis. Some residual curvature in the ridges always remains, however, especially at the low energy. This curvature smears up the projected one dimensional pulse shape spectrum and thus reduces the potential resolution.

Collecting the data event by event on tape, and defining two dimensional curved pulse shape boundaries, as done in this experiment, preserves maximum sensitivity of the pulse shape discrimination. A periodic recording of two-dimensional spectra for updating the pulse shape windows is necessary as a protection against shifts in electronics. To reduce this possibility, electronic delays were replaced with cable delays wherever possible and periodic checks were made of all parameters susceptible to shifts. Cable delays also reduced the dead time at high counting rates. The use of three small detectors (3.8 cm dia. x 5 cm height) was also dictated by the high counting rate problem.

The detectors were clamped in a universal stand, during the experiment, allowing their repositioning in all three space dimensions (Fig. B.3.1.2).

### B.3.2 Structure of the Double Header Neutron Detectors

NE213 liquid scintillators were used as neutron detectors because of their good pulse shape discrimination properties. Because of the low counting rate problem the



detectors had to be made large. The width and the height of the detector were chosen so that they contributed equally to the finite geometry energy spread in the data. The detectors were rectangular, 7.6 cm wide, 16.2 cm high and 6.35 cm thick. To improve the timing resolution of the detector two RCA 4522 photomultiplier tubes were mounted, one on the top, one on the bottom of each detector, and the two fast outputs were added, after passing through matching delays, in a  $50\Omega$  adder (Fig. B.1.1). The linear signals from the two ends of each detector were also added at the preamplifier input.

The neutron detectors were mounted on a mobile stand allowing changes in angles and neutron flight distances for each detector individually (see Fig. B.3.1.2).

### B.3.3 The Geometry of the Experiment

The angles, at which the neutron detectors were positioned in the experiment, were selected to depict the enhancement of the three body  $D(n,2n)p$  break up cross section due to the Quasi-free scattering mechanism.

Although in the exact quasi-free scattering process, in which the proton is left with zero kinetic energy, occurs at  $41.5^\circ$ ,  $-41.5^\circ$  neutron angles for an incident energy of 21.5 MeV, the break up is dominated by the effect over a wide range of angles around this geometry. Here the proton is left with non-zero share of the total kinetic energy.



In this work, the angles were limited by the need to obtain a detectable proton recoil in the C6D6 target detector. Quasi Free Scattering data from nine different pairs of neutron angles were collected in three separate runs. Three angle pairs were collected simultaneously in each run.

The geometry of the first run is displayed in Figs. B.1.1 and B.3.3.1. One symmetric ( $35^\circ$ ,  $-35^\circ$ ) and two asymmetric ( $43.1^\circ$ ,  $-28.3^\circ$ ;  $52.0^\circ$ ,  $-21.2^\circ$ ) angle pairs were studied. The neutron detectors were set at unequal distances from the D target. Detector #1 was set at 75 cm to increase the eight fold coincidence countrate, while detector #2 was set at 150 cm to preserve the neutron time-of-flight resolution with the intention of later projecting the data onto the neutron #2 energy axis.

In the next two runs a symmetric geometry was used. The neutron detectors were set at equal distances (130 cm average) from the C6D6 detector, symmetrically about the deuteron beam axis (Fig. B.3,3.2) with the plan of projecting the data onto the kinematical locus. The angle pairs studied were:  $23.8^\circ$ ,  $-23.8^\circ$ ;  $25.0^\circ$ ,  $-25.0^\circ$ ;  $26.5^\circ$ ,  $-26.5^\circ$  in the second run and  $28.7^\circ$ ,  $-28.7^\circ$ ;  $30.0^\circ$ ,  $-30.0^\circ$ ;  $31.4^\circ$ ,  $-31.4^\circ$  in the third run.

Attempts to keep the conditions as close as possible to the ideal Quasi Free Scattering in the first run







Figure B.3.3.1 A plane view of the three asymmetric scattering geometries running simultaneously - Run #1.

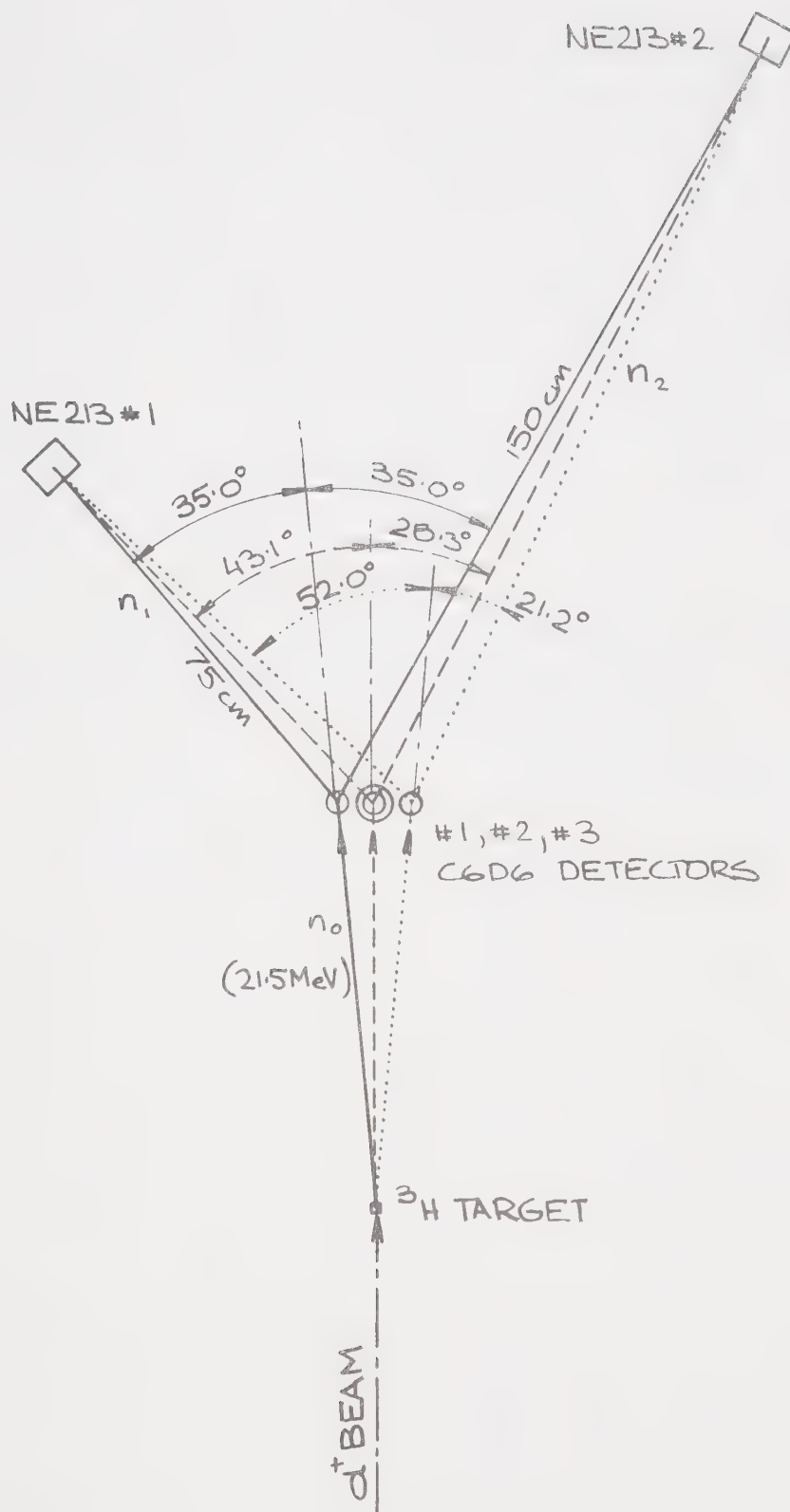
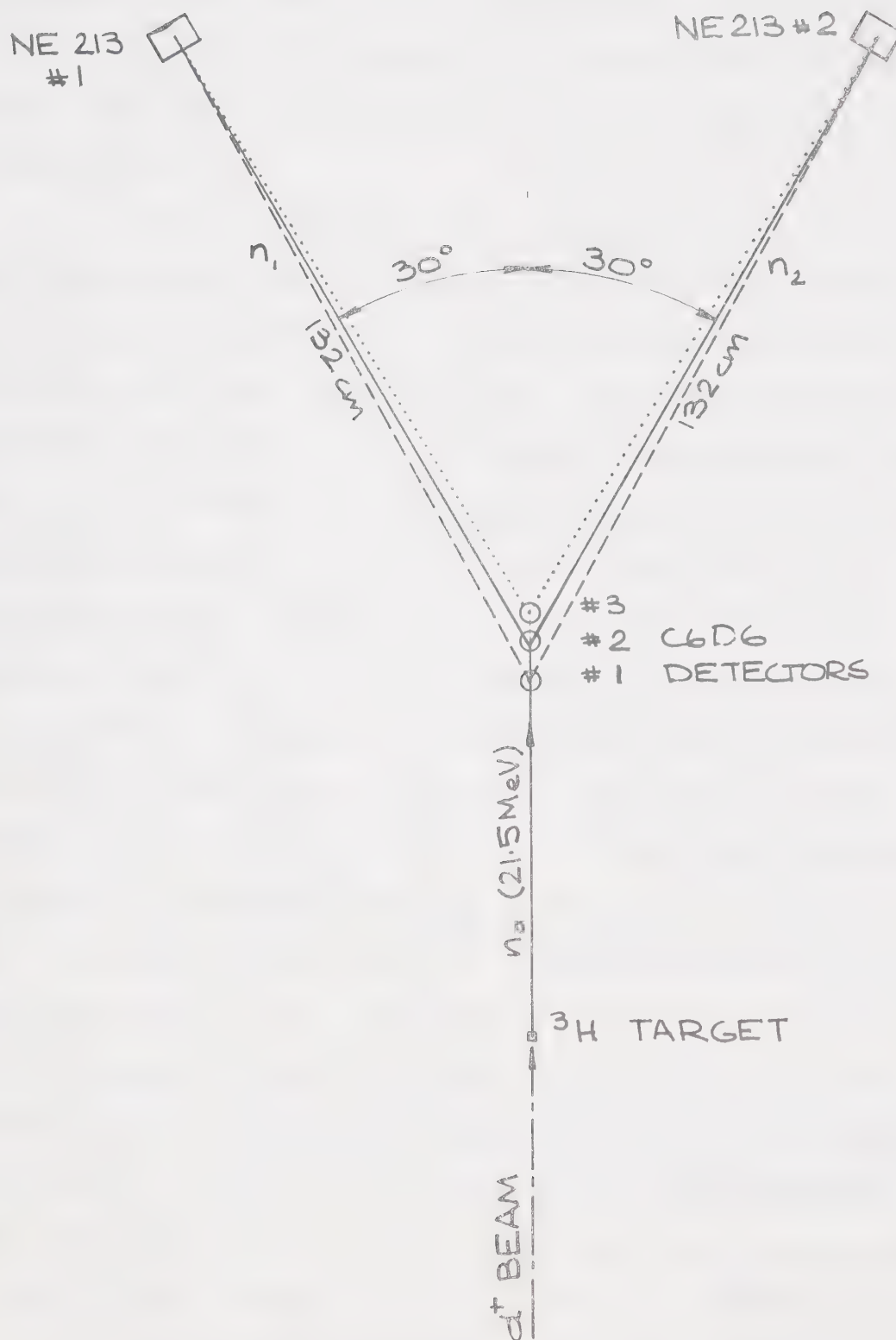






Figure B.3.3.2 A plane view of the three symmetric scattering geometries simultaneously running in Run #3.







resulted in many challenging experimental problems associated with running the C6D6 detectors at an extremely low energy bias. This was set at 1/4 of  $^{241}\text{Am}$  x-ray peak energy (see Chapter B.4).

As the relative light response of the proton in the C6D6 scintillator to that of the electron is virtually unknown and unpublished for these extremely low energies it was discovered only after the run, when we made our own deuteron and proton recoil calibration measurements, that the 1/4  $^{241}\text{Am}$  electron energy corresponds to  $\sim 170$  keV proton energy (Fig. B.3.3.3). At the same time, the minimum breakup proton energy in the three geometries studied in the first run is 173 keV, 114 keV and 40 keV respectively. Obviously, the number of counts in the QFS peak area, where the proton energy drops to the minimum, is reduced by the effect of the bias in these three geometry settings. An attempt was made to correct the cross-section for this effect by multiplying the data with the ratio of the total area of the measured resolution peak of the proton recoil energy in the C6D6 to the part of the area above the detector bias. The position and the width of the resolution peaks were obtained by fitting a known energy deuteron recoil peak with the Gaussian shape. The recoil peaks were obtained in n-d elastic scattering runs at various scattering angles.

The C6D6 energy recoil pulse was collected in a two dimensional histogram with the scattered neutron time-



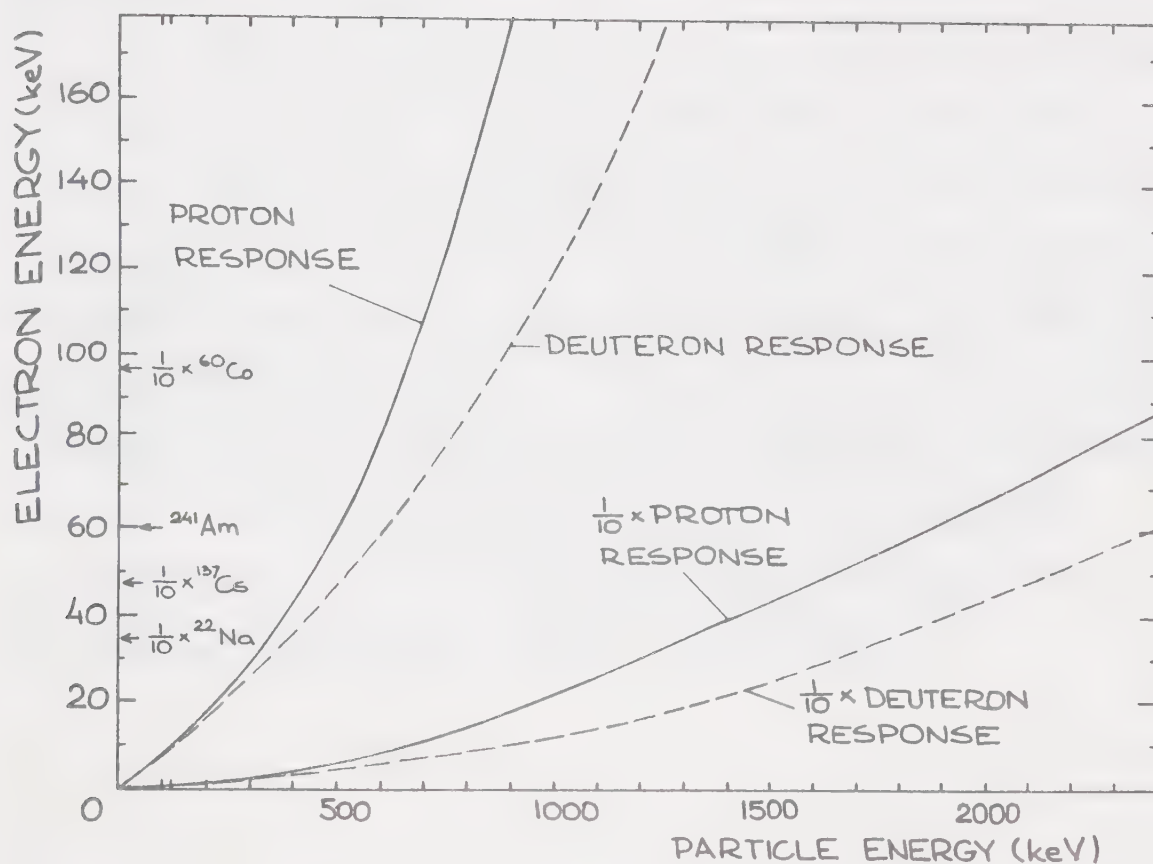


Figure B.3.3.3 Light response of NE230 (C6D6) detector for recoiling protons and deuterons relative to electrons. (Compiled from: Sm-68, Pa-75, and Br-72 and verified by our experiment.)



of-flight (Fig. B.3.3.4). The two dimensional spectrum was truncated to include only the time-of-flight region corresponding to the n,d elastic scattering peak, background fitted, subtracted from the data and this projected onto the recoil energy axis.

While the application of this correction can only be regarded as reasonable in the  $35^\circ$ ,  $-35^\circ$  geometry set all the three sets of data from the first run were valuable in learning about the effect of the C6D6 bias at extremely low proton recoils in the C6D6 scintillator. This experience was used in the setting up for the next runs. There the kinematically defined minimum proton energy was 680 keV and 370 keV respectively. In both cases the entire finite resolution peak around this minimum proton energy was above the C6D6 detector bias setting.



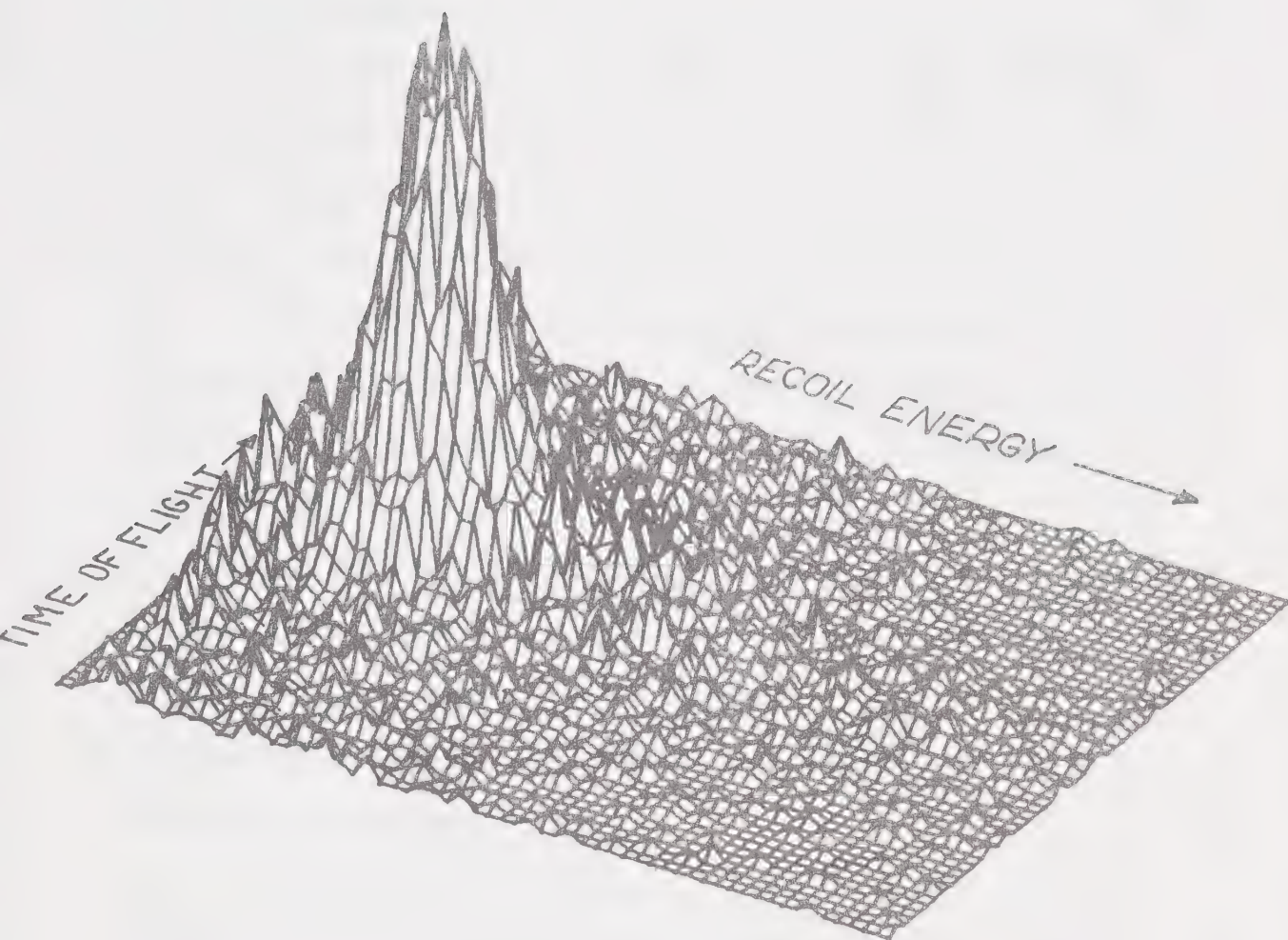


Figure B.3.3.4 A typical shape of the deuteron recoil peak, in a two-dimensional plot of time-of-flight versus C6D6 detector pulse height, produced by  $35^\circ$  elastic scattering of 21.5 MeV neutrons on deuterons in the C6D6 scintillator.





## B.4 ELECTRONICS

As discussed in Chapter B.3.1, eight parameters were collected for each event in the kinematically complete  $D(n,2n)p$  experiment. The parameters in excess of the five variables, required for the kinematically complete definition of the event provided additional constraints which were useful in the separation of the true events from the background. The type and origin of these parameters is indicated in Fig. B.1.1. They were:

- (1) Neutron #1 time of flight - TOF 1
- (2) Neutron #2 time of flight - TOF 2
- (3) Neutron detector #1 pulse height
- (4) Neutron detector #1 pulse shape
- (5) C6D6 detector pulse height
- (6) C6D6 detector pulse shape
- (7) Neutron detector #2 pulse height
- (8) Neutron detector #2 pulse shape

All these eight parameters were processed by the electronics (see diagram B.4.1) in eight-fold coincidence and converted into eight digital words by the eight analog-to-digital converters, P, Q, R, S, T, U and V respectively, of the Tennelec interface to a Honeywell 516 computer. The data were recorded on magnetic tape event by event and display monitored, at the same time, by the on-line analysis routine (Chapter B.5).



All three C6D6 detectors were treated as one by the electronics fanning together their fast and summing their slow signals. The identity of the C6D6 detector involved in the event was coded into the C6D6 pulse height parameter by means of a four-way routing (Fig. B.4.3).

The two neutron time-of-flight spectra were collected as singles at the same time in an additional pair of analog-to-digital converters (ADC A and ADC B). These spectra, containing the n,d elastic scattering peak, were used as monitors to normalize the breakup cross-section using published values of the n+d differential cross-section (Se-72), thus eliminating the need for the exact knowledge of target thickness, beam current, incident neutron flux, etc.

The characteristic parts of the eight fold coincidence circuit (Fig. B.4.1) are further described individually with the diagrams of the corresponding parts of the entire circuit diagram B.4.1. The fast timing signals and the slow logic signals in all of these diagrams are displayed as thin lines while the slow linear signals are indicated by thick lines.

#### B.4.1 Neutron Time of Flight

The fast anode outputs from the two headers on each neutron detector were time matched by nanosecond delays and added in a simple  $50\Omega$  adder. These signals then



were fed to an ORTEC 453 Constant Fraction Timing Discriminator (CFTD) with the fraction set to 0.5 and the output used to start ORTEC 437A Time-to-Amplitude Converters (TAC). Delayed discriminator outputs from the ORTEC 270 tube bases of the C6D6 detectors were used as the stop pulse on each TAC.

The three C6D6 detector timing signals were fanned together by a fast EG&G logic OR-module and later unfolded in the analysis by the routing bit of the C6D6 pulse height word. Pile up events, defined by the occurrence of fast outputs from two different C6D6 detectors within 500 nsec resolving time, were eliminated by an anticoincidence input into the eight fold master gate (Fig. B.4.5).

#### B.4.2 C6D6 Detector Pulse Height (Proton Recoil Energy) and the Four-Way Routing

The linear outputs of the ORTEC 270 tube bases were fed into ORTEC 460 Delay line amplifiers. The singly differentiated unipolar output signals were summed by a summing amplifier and converted in ADCT, which set the routing bit of the digital word according to the combination of two logic signals on its routing inputs A and B. There are four such combinations, which was sufficient to distinguish the three C6D6 detectors. The fourth routing channel was used for a C6H6 (normal benzene) detector in later experiments.

The routing logic signals were derived from the



C6D6 fast signals converted into slow logic signals by a CFTD. The high rate of the routing signals due to extremely high counting rate ( $\sim 80$  kHz in each of the C6D6 detectors) was reduced by a coincidence requirement of at least one simultaneous neutron detector output.

Four routing signals 1, 2, 3, 4 were converted into a combination of two routing bit A and B signals by a four-way routing module built in our laboratory.

The energy bias on the C6D6 detectors was set at  $1/4$   $^{241}\text{Am}$  source energy in the first and the third runs and to  $1/3$   $^{241}\text{Am}$  energy in the second run. The bias setting in the neutron detectors was  $1 \times$   $^{60}\text{Co}$  in the first run and  $1/3$   $^{22}\text{Na}$  Compton electron energy in the second and third runs.

#### B.4.3 Pulse Shape Discrimination Circuits

The pulse shape discrimination circuit used with the C6D6 detectors was of the type discussed in Chapter B.3.1. The doubly differentiated (bipolar) output of the same ORTEC 460 Delay line amplifier, as used in the C6D6 pulse height, produced a fast timing signal in an ORTEC 450 Timing Single Channel Analyzer (TSCA). This was derived from its zero-crossing time. This signal was used as the start of a time-to-amplitude converter and the delayed C6D6 fast output used as the stop of the TAC. To cope with the high counting rate in the C6D6 detectors only cable delays ( $\sim 1$   $\mu\text{s}$ ) were used on the fast C6D6 signal.





Further possible dead time due to a busy TAC was avoided by gating the TAC with the neutron detector event (dashed line). The DDL amplifiers were set to their shortest integration time (0.004 setting). The three pulse shape signals were summed by a summing amplifier and converted on ADCU.

The neutron detector pulse shape circuit was identical to that of the C6D6 detectors except for the use of a Gate and Delay Generator (G&DG) in place of the cable delay, as the counting rate in these detectors was low.

#### B.4.4 The Eight-Fold Master Gate

Diagram B.4.5 indicates the logic used to define the eight fold coincidence gate. In addition to the double coincidence of the two time of flight signals the presence of the pulse height and pulse shape parameters from both neutron detectors was demanded. These two logic signals were obtained by application of a fully open single channel analyzer window on the neutron detector pulse shape TAC outputs.

It should be noticed, that only the presence of the C6D6 fast signal was demanded, via the requirement of the time-of-flight TAC outputs, while the C6D6 pulse shape and pulse height requirements were relaxed. This allowed us to record on tape even the events where the proton recoil energy signal in the C6D6 scintillator was below the slow



bias, but still above the fast bias (as the fast bias was always set slightly below the slow one) and thus save the events where the C6D6 pulse shape signal was missing. This also saved events which would be otherwise lost due to the C6D6 pulse shape TAC being busy. Such events, classified as "zero data" by the data acquisition program (see Chapter B.5) were distinguished from the regular eight parameter events by a negative number in place of the missing word.

As mentioned above, events having C6D6 detector outputs within  $0.5 \mu$  sec were cancelled by an anticoincidence input overlapping the three coincidence inputs in the main triple coincidence. This signal was derived from the double coincidence of two valid outputs from any two C6D6 detectors.

#### B.4.5 The Monitors

The monitor circuit is shown in Fig. B.4.6. The two Time of flight signals, converted into two singles TOF spectra via ADCA and ADCB, were obtained in the same electronics circuit as the eight-parameter events without the eight fold coincidence requirement. Two features were different from the original circuit. An analog window was set on n- $\gamma$  pulse shape discrimination using a single channel analyzer on each neutron and C6D6 #1 pulse shape TAC output. These logic signals were used to open gates on the ADC's. Secondly, the C6D6 pulse shape discrimination circuit was duplicated for the monitors as the dynamic range of the DDA



amplifier, set for the low energy proton recoils, would not cover the elastic deuteron recoil energy in the first run geometry. The two different dynamic ranges were not necessary in the next two runs, where the proton energy was higher and the deuteron recoil lower at the smaller scattering angles. Only one C6D6 detector was used in the monitor circuit.





Figure B.4.1 Eight-parameter electronics diagram. Fast and logic signals indicated by thin lines, linear signals indicated by heavy lines.



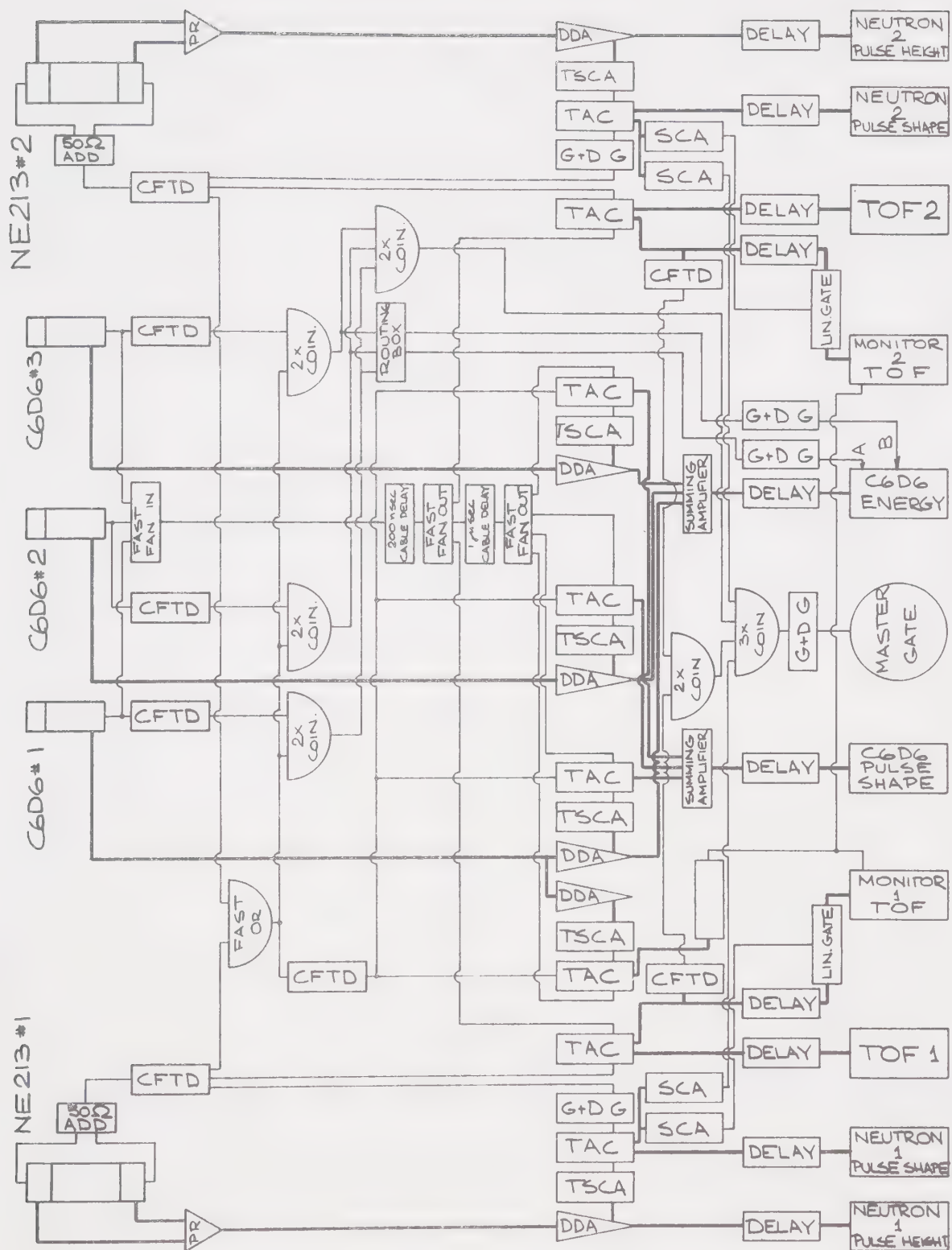






Figure B.4.2 Time-of-flight circuit diagram.

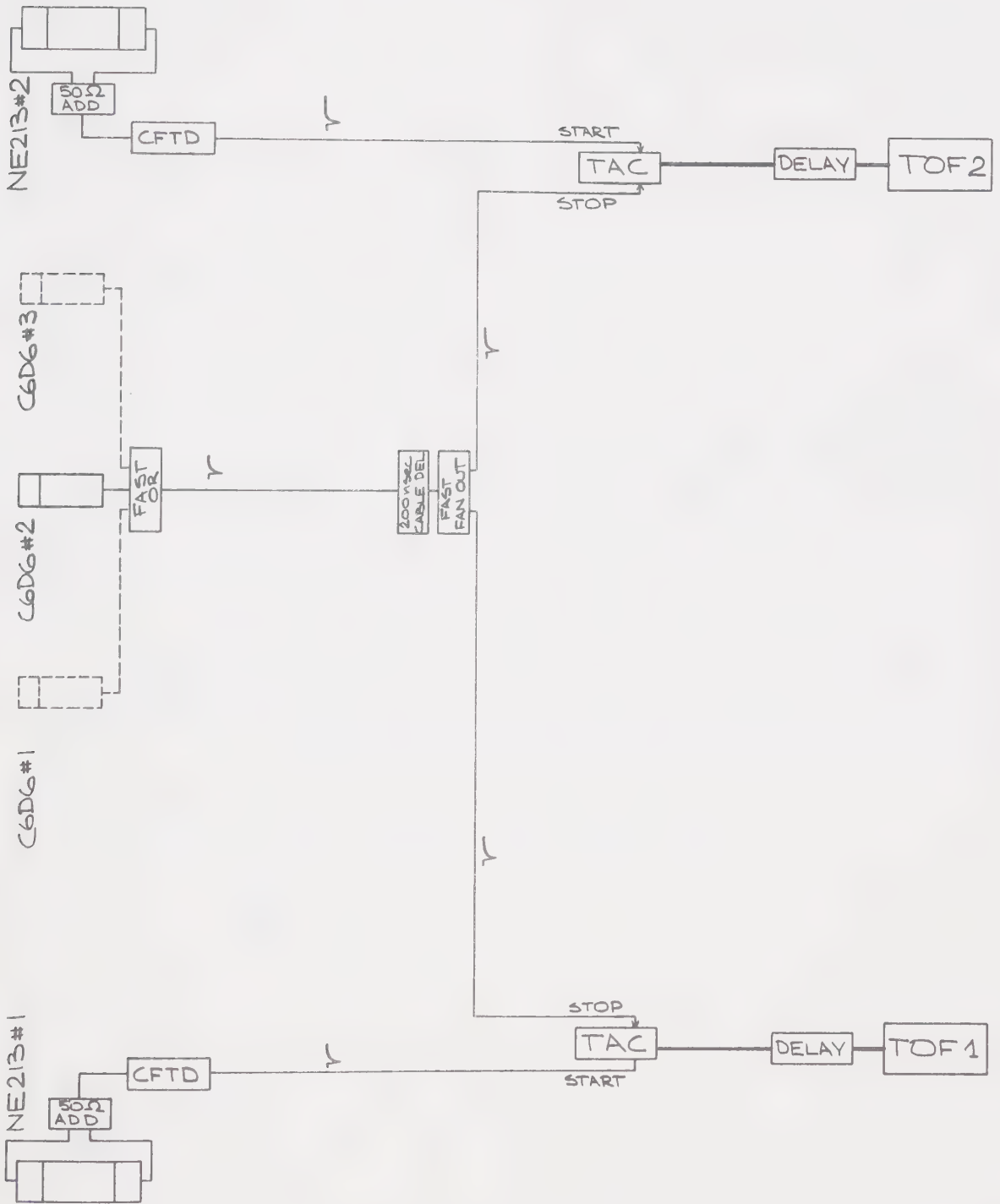






Figure B.4.3 Electronics circuit of C6D6 pulse height  
with four way routing.



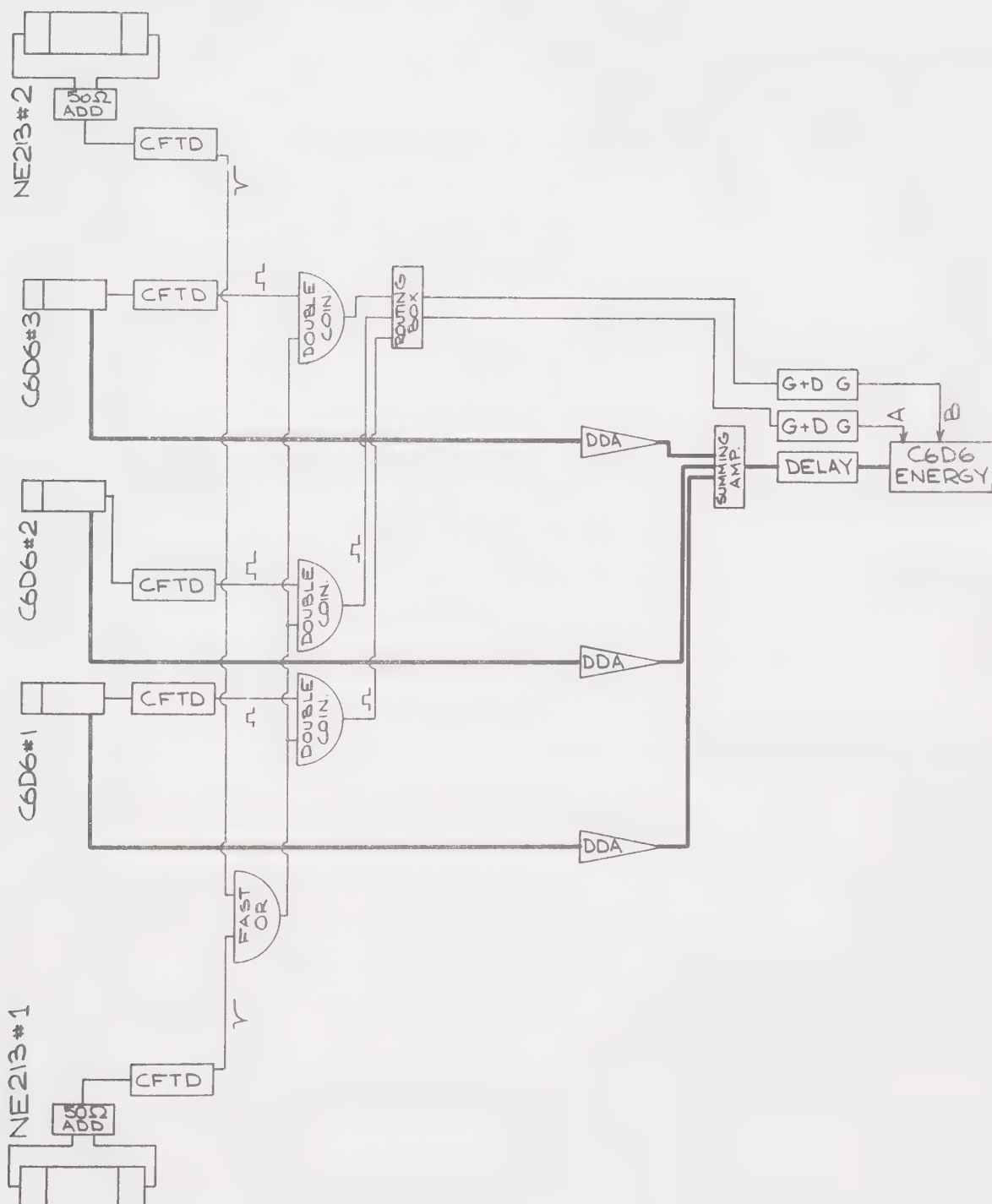






Figure B.4.4 Pulse shape discrimination circuits.

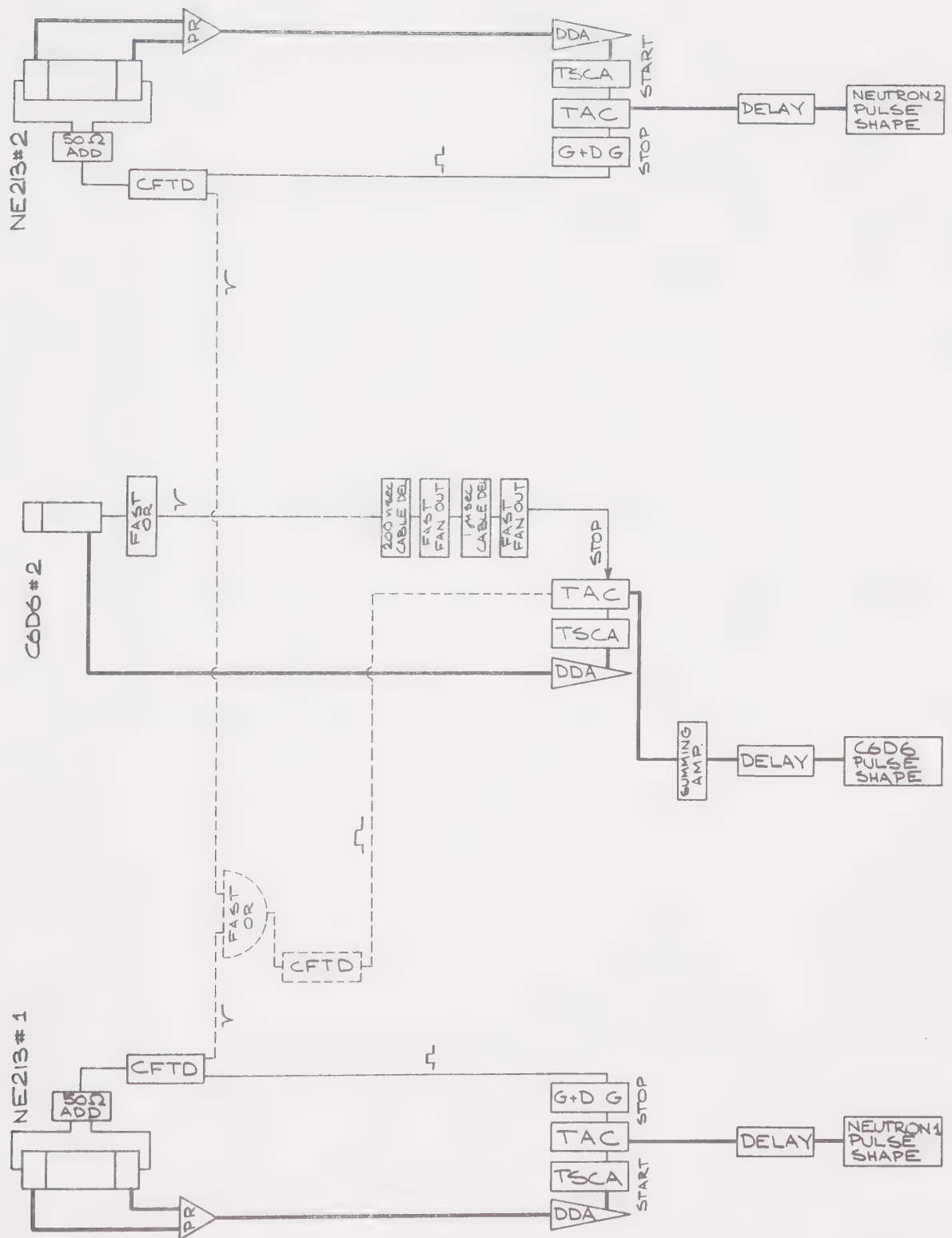






Figure B.4.5 Eight-fold coincidence gate.



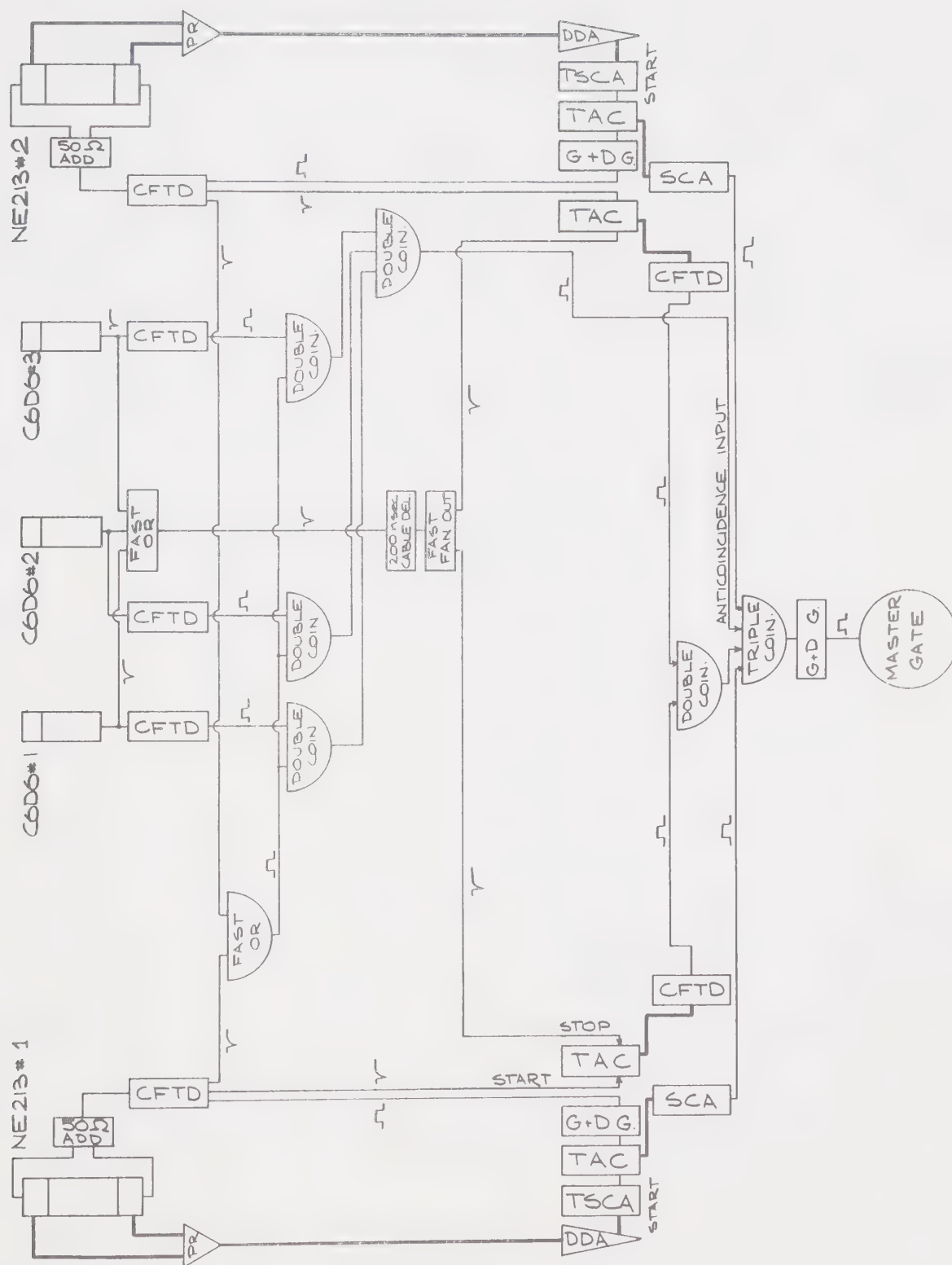
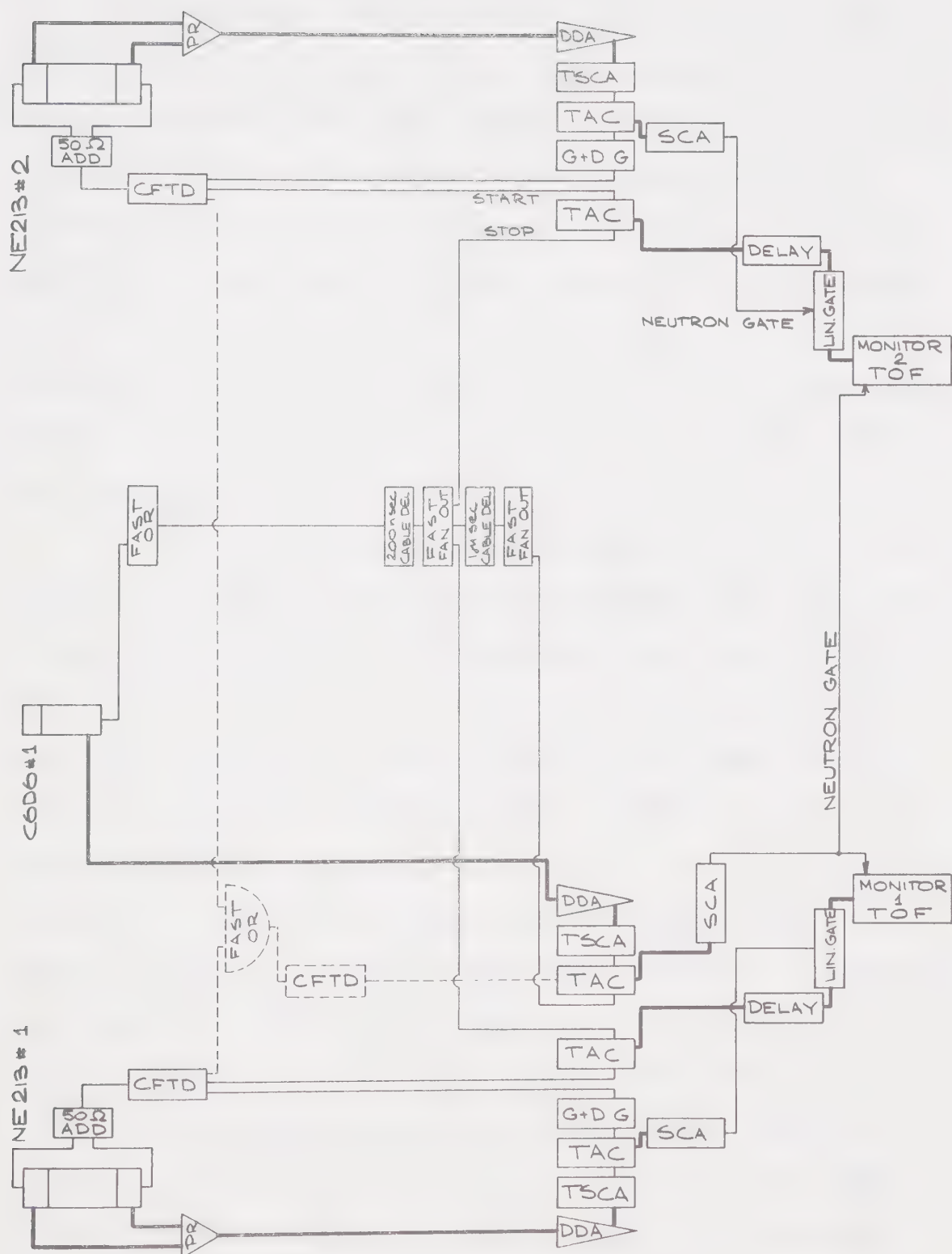






Figure B.4.6 The electronics circuit of the monitors.





## B.5 THE DATA ACQUISITION PROGRAM

The General Purpose Kick Sorter software system (GPKS)(ref. Da-70 ), available at the University of Alberta Nuclear Research Centre for general on line data acquisition with the Honeywell 516 computer, was extended for eight-parameter event-by-event recording on a magnetic tape and modified to adapt "user" Fortran subroutines. The compiled program for the on line D(n,2n)p data acquisition "OLINA" consisted of selected GPKS routines and Fortran subroutines for data collecting initialization and for a simple on-line data analysis.

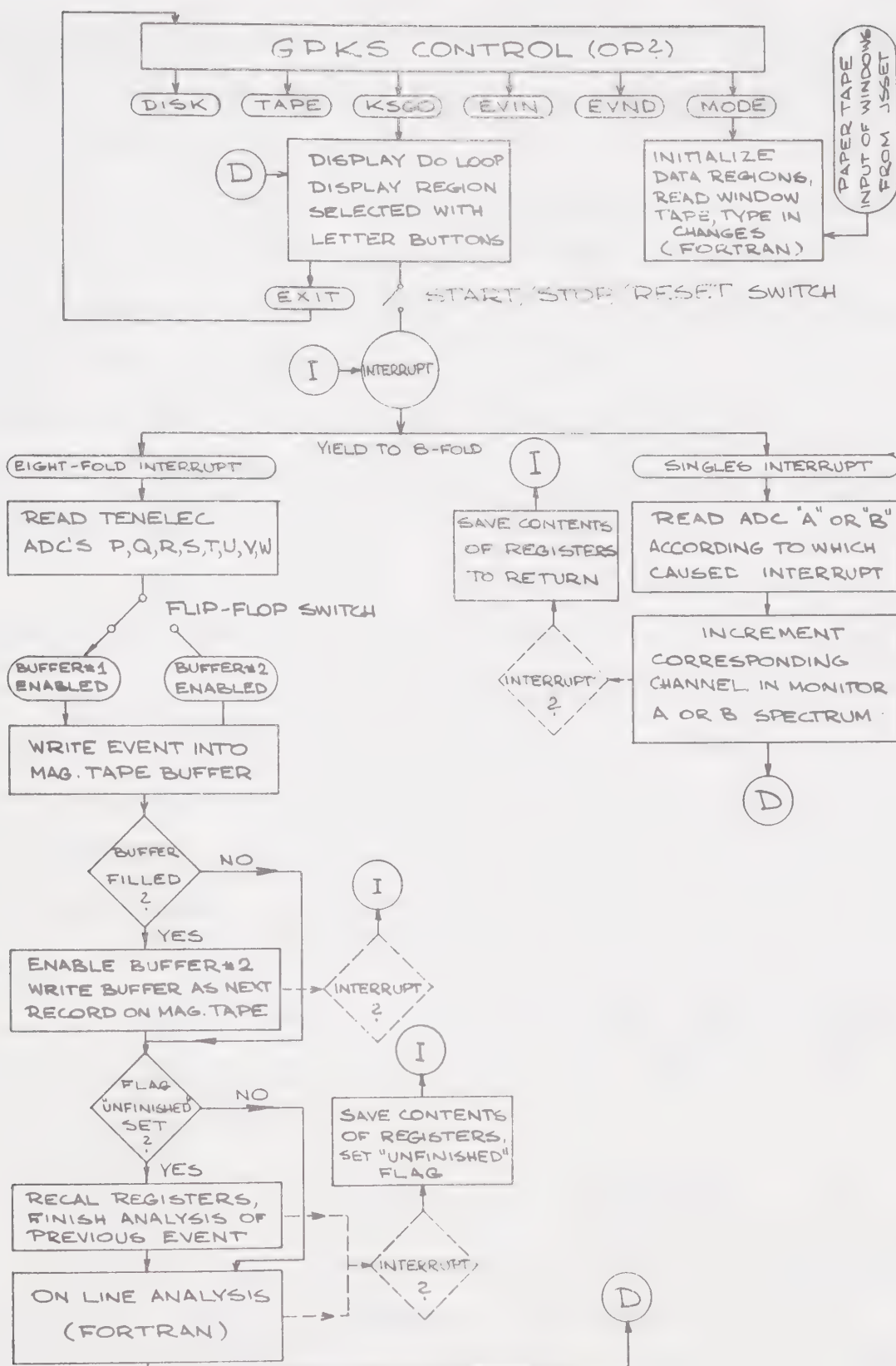
The block diagram of the program is shown in Fig. B.5.1. The teletype GPKS control dispatched the access to various GPKS functions. The important ones were: KSGO, EVIN, EVND, TAPE and DISK. EVIN opened a new event recording file on the tape. EVND terminated the event recorded file by a tape mark. TAPE and DISK allowed writing of whole spectra regions on magnetic tape or disk as well as reentering data from these peripherals into the memory core. KSGO readied the ADC's waiting for an event interrupt and started the display of data with the data region selected by a letter switch. The continuous display "DO" loop was only exited by a display interrupt or by an event interrupt from the ADC's. The display interrupts, controlled by a light pen and display switches included a number of functions, such as cropping and expanding of the display, summing of







Figure B.5.1 A block diagram of the data acquisition program.





peaks, etc. The displayed image could also be rotated and tilted - a feature particularly convenient when displaying two dimensional histograms.

Two kinds of event interrupts existed. The eight-fold coincidence interrupt occurred when the eight-fold coincidence master gate logic pulse arrived at the Tennelec event input. A singles interrupt occurred when a monitor singles time-of-flight signal arrived at ADCA or ADCB. The eight-fold coincidence interrupt had priority over the singles interrupt.

Storing of events in a buffer for the event recording on tape was part of the eight fold coincidence interrupt routine and thus it had priority over the computer background routines, which included the on line analysis. Two 512 word buffers, enabled by a flip-flop switch, assured fast recovery of the computer to accept the next event after writing on tape. 59 events, together with their delimiter words, filled one buffer.

The on line analysis of an event, unfinished due to the interrupt, was completed when the computer background was again available.

#### B.5.1 The On-Line Analysis Subroutine (ANALYZ)

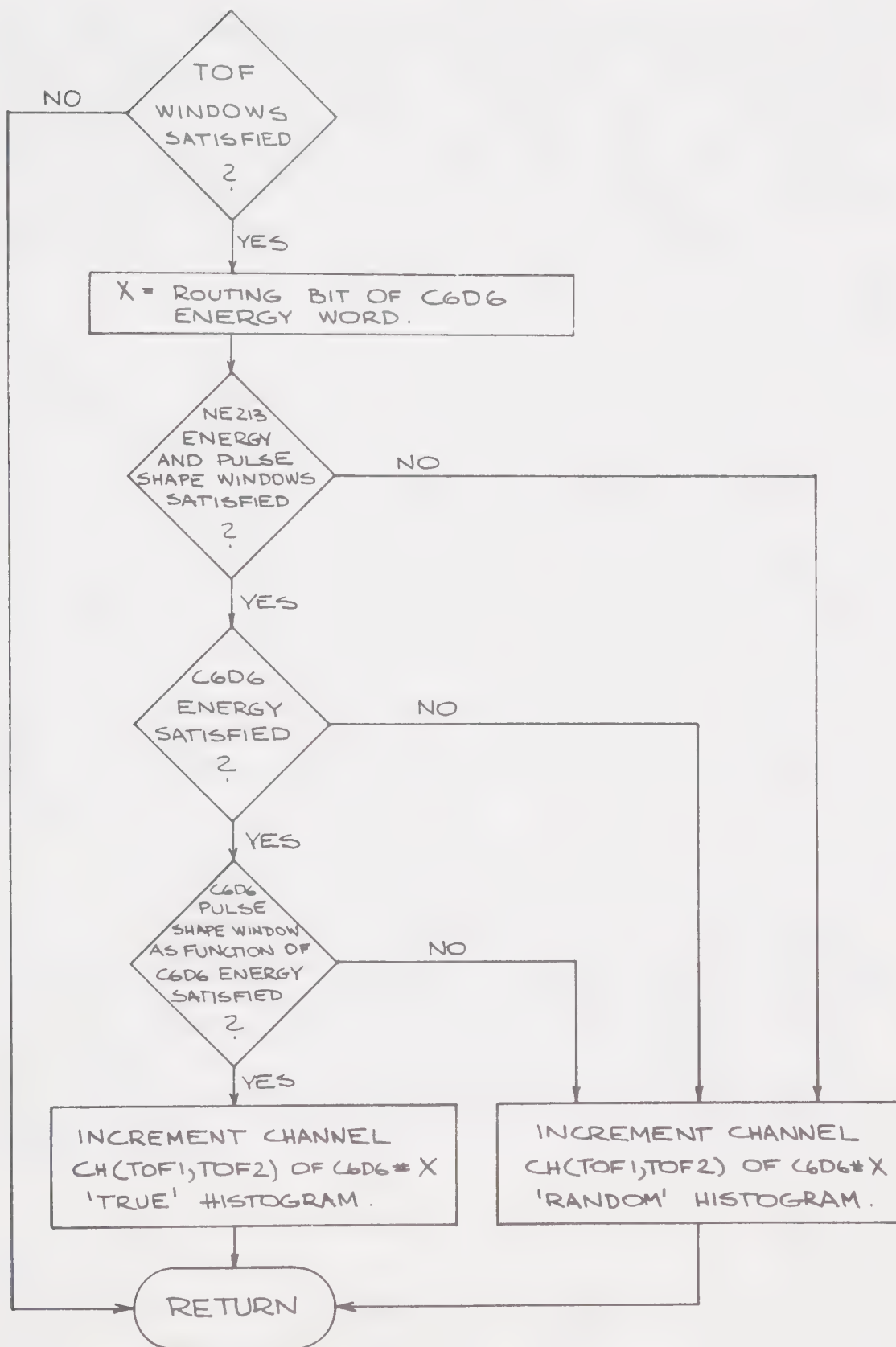
The eight fold coincidence events were accumulated in 32 x 32 channel two dimensional histograms of TOF 2 versus TOF 1 by the ANALYZ subroutine. Events were sorted





Figure B.5.2 A logic tree diagram of the Fortran subrouting 'ANALYZ' contained in the data acquisition program as the on-line analysis of the eight-fold coincidence data.







into eight such spectra, two for each C6D6 geometry. (The fourth C6D6 routing channel was unused.) The two regions for each C6D6 detector were separating into those called "TRUE" which satisfied a set of eight parameter windows and those, which did not, in regions called "RANDOM".

The eight parameter windows were defined by light pen in a separate program called JSSET and then they were punched on a paper tape. This tape was then read in OLINA in its initialization MODE subroutine (Fig. B.5.1).

The spectra, accumulated periodically in the program JSSET, for the definition of the windows and their updating, were also written as intermittent files on the event recording tape. They were later used, in a more sophisticated way, for chronological updating of windows during the playback of events in the off-line analysis program.

The OLINA and JSSET programs are described in detail in (So-76). The C6D6 pulse shape discrimination windows for the on-line analysis were defined, using light pen, as curved boundaries, intensified in the two dimensional pulse height vs. pulse shape display (as suggested in Chapter B.3.1).



## B.6 THE DATA ANALYSIS PROGRAM

A General Off-Line Deuteron breakup Package of Analysis (GOLDPAN) was written in Fortran language as part of this project for the off-line  $D(n,2n)p$  data reduction on an SDS 940 computer.

The package consists of twelve different callable programs, each new program overlaying the former program in the memory by means of Fortran Linking procedure included in the MONARCH software system of the SDS 940 computer. The programs, linked in the GOLDPAN package, contain all routines encountered in the process of the  $D(n,2n)p$  data reduction. These include: definition of the eight parameter windows; calibration of the neutron time-of-flight and its conversion into neutron energy; calculation and display of the kinematical locus and the kinematically allowed broadening band around it; playback of the event recorded data from a nine-track magnetic tape with forming and display of two-dimensional histograms; projections of histograms subject to two-dimensional cuts; storing and recall of analyzed data sets; plotting of the analyzed data as one-dimensional or two-dimensional histograms and scatter plots by a Houston Omnigraphic Plotter. The main interactive user control of the program is accomplished by a light pen and an RCT display. A teletype is used as an I/O device for tape file labels and change of variable values only. An "AUTOMATIC PILOT" feature is included in the package, which allows the



user to switch the command input to a card reader, where the sequence of commands for the entire analysis can be accumulated in a deck of punched cards. This was found very useful, since the analysis is usually repeated many time, changing only the window set and C6D6 detector numbers. There are seven principal links in the package, which have direct mutual access via the "JOB JUNCTION" (Fig. B.6.1). The remaining five are mere extension segments of the principal links, where these became too large to be contained in the directly addressable memory. They always return to the link from which they were called with the exception of link 11. This returns control to link 1. The interactive control in the principal links and link 11 is based on a system of display pages branching into a "tree" from the first page in each link. Some examples of the display pages are shown in Figs. B.6.2 and B.6.3. Each display page consists of an alphanumeric message at the top and an eventual data display. The alphanumeric message contains a heading in the first line and function branch labels in the following rows. A light pen hit in the message brings another display page according to the label hit. A hit in the heading line returns to the previous page. A light pen hit in the data display executes functions of the current page. These involve intensification of channel points or intervals of the data display in most cases. The







Figure B.6.1 The link structure of the off-line data reduction program. Arrows indicate the access between individual links.

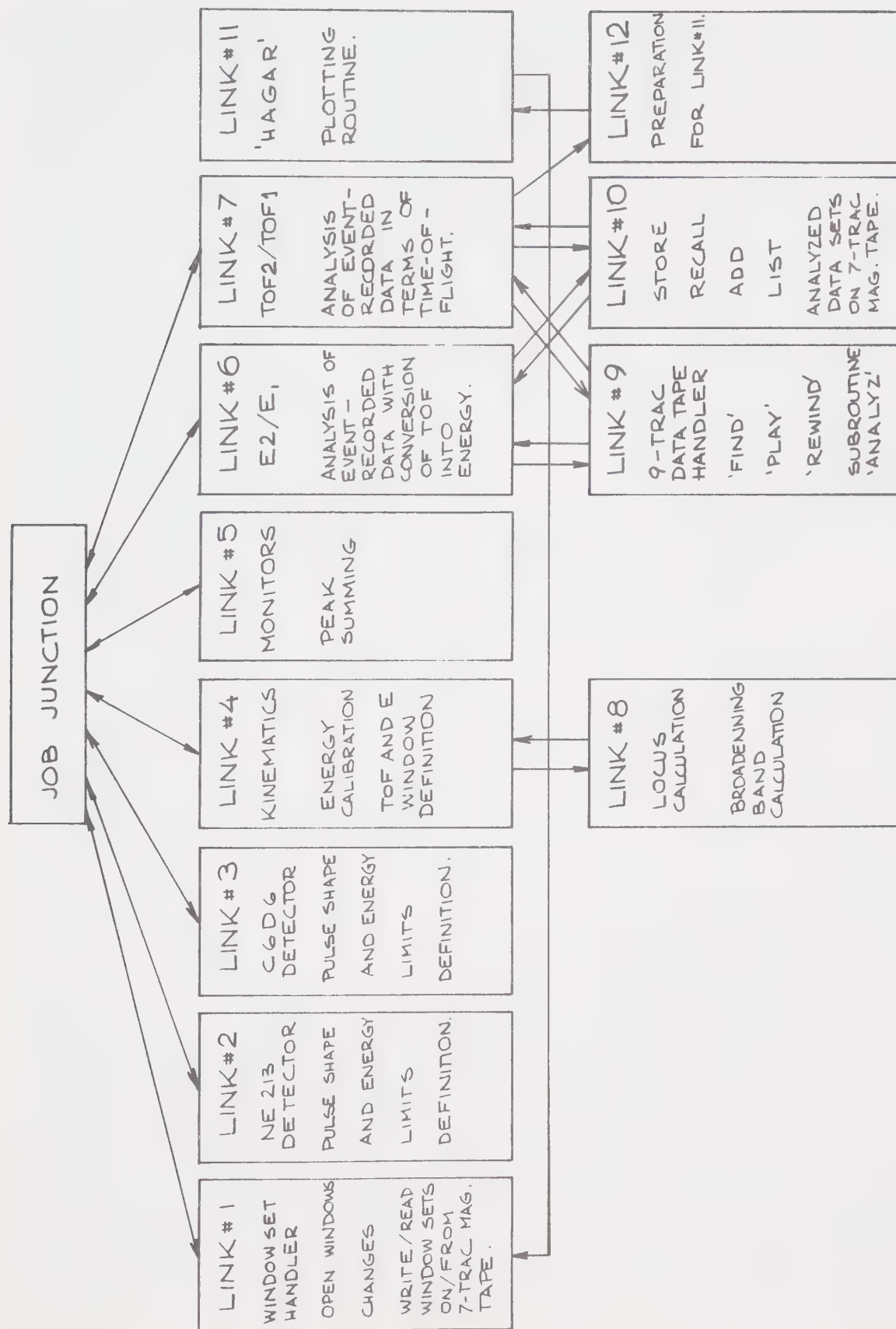






Figure B.6.2 Examples of the computer display "pages" included in the data reduction program. First row: calibration of the singles time-of-flight spectrum and definition of TOF and  $E_n$  limits. Second row: definition of the neutron detector pulse shape windows.

NOTICE: See page 100.

1 HAZARD DET. MINOR (2)  
2 HAZ. W/INSTR. DETECTION  
3 CAL. ALARM DEFECTION  
4 TOP SPEED 135  
5 HONKOR-BELL'S  
6 KNOCK-OUT BY ENEMY FOR  
7 KNOCK-OUT BY ENEMY FOR

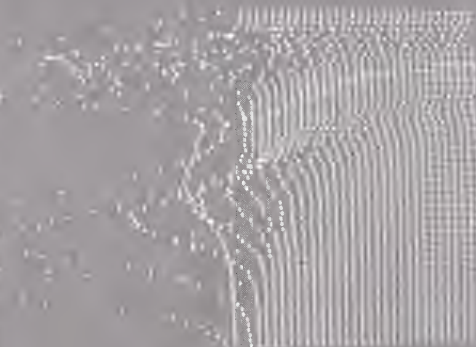
1980 SINGLES CHART



TOP	00000000000000000000
LOWER	00000000000000000000
UPPER	00000000000000000000
TOTAL	00000000000000000000
LOWER	00000000000000000000
UPPER	00000000000000000000
TOTAL	00000000000000000000



1993, 1994, 1995, 1996, 1997, 1998, 1999, 2000, 2001, 2002, 2003, 2004, 2005, 2006, 2007, 2008, 2009, 2010, 2011, 2012, 2013, 2014, 2015, 2016, 2017, 2018, 2019, 2020, 2021, 2022, 2023, 2024, 2025, 2026, 2027, 2028, 2029, 2030, 2031, 2032, 2033, 2034, 2035, 2036, 2037, 2038, 2039, 2040, 2041, 2042, 2043, 2044, 2045, 2046, 2047, 2048, 2049, 2050, 2051, 2052, 2053, 2054, 2055, 2056, 2057, 2058, 2059, 2060, 2061, 2062, 2063, 2064, 2065, 2066, 2067, 2068, 2069, 2070, 2071, 2072, 2073, 2074, 2075, 2076, 2077, 2078, 2079, 2080, 2081, 2082, 2083, 2084, 2085, 2086, 2087, 2088, 2089, 2090, 2091, 2092, 2093, 2094, 2095, 2096, 2097, 2098, 2099, 2100, 2101, 2102, 2103, 2104, 2105, 2106, 2107, 2108, 2109, 2110, 2111, 2112, 2113, 2114, 2115, 2116, 2117, 2118, 2119, 2120, 2121, 2122, 2123, 2124, 2125, 2126, 2127, 2128, 2129, 2130, 2131, 2132, 2133, 2134, 2135, 2136, 2137, 2138, 2139, 2140, 2141, 2142, 2143, 2144, 2145, 2146, 2147, 2148, 2149, 2150, 2151, 2152, 2153, 2154, 2155, 2156, 2157, 2158, 2159, 2160, 2161, 2162, 2163, 2164, 2165, 2166, 2167, 2168, 2169, 2170, 2171, 2172, 2173, 2174, 2175, 2176, 2177, 2178, 2179, 2180, 2181, 2182, 2183, 2184, 2185, 2186, 2187, 2188, 2189, 2190, 2191, 2192, 2193, 2194, 2195, 2196, 2197, 2198, 2199, 2200, 2201, 2202, 2203, 2204, 2205, 2206, 2207, 2208, 2209, 2210, 2211, 2212, 2213, 2214, 2215, 2216, 2217, 2218, 2219, 2220, 2221, 2222, 2223, 2224, 2225, 2226, 2227, 2228, 2229, 2230, 2231, 2232, 2233, 2234, 2235, 2236, 2237, 2238, 2239, 2240, 2241, 2242, 2243, 2244, 2245, 2246, 2247, 2248, 2249, 2250, 2251, 2252, 2253, 2254, 2255, 2256, 2257, 2258, 2259, 2260, 2261, 2262, 2263, 2264, 2265, 2266, 2267, 2268, 2269, 2270, 2271, 2272, 2273, 2274, 2275, 2276, 2277, 2278, 2279, 2280, 2281, 2282, 2283, 2284, 2285, 2286, 2287, 2288, 2289, 2290, 2291, 2292, 2293, 2294, 2295, 2296, 2297, 2298, 2299, 2300, 2301, 2302, 2303, 2304, 2305, 2306, 2307, 2308, 2309, 2310, 2311, 2312, 2313, 2314, 2315, 2316, 2317, 2318, 2319, 2320, 2321, 2322, 2323, 2324, 2325, 2326, 2327, 2328, 2329, 2330, 2331, 2332, 2333, 2334, 2335, 2336, 2337, 2338, 2339, 2340, 2341, 2342, 2343, 2344, 2345, 2346, 2347, 2348, 2349, 2350, 2351, 2352, 2353, 2354, 2355, 2356, 2357, 2358, 2359, 2360, 2361, 2362, 2363, 2364, 2365, 2366, 2367, 2368, 2369, 2370, 2371, 2372, 2373, 2374, 2375, 2376, 2377, 2378, 2379, 2380, 2381, 2382, 2383, 2384, 2385, 2386, 2387, 2388, 2389, 2390, 2391, 2392, 2393, 2394, 2395, 2396, 2397, 2398, 2399, 2400, 2401, 2402, 2403, 2404, 2405, 2406, 2407, 2408, 2409, 2410, 2411, 2412, 2413, 2414, 2415, 2416, 2417, 2418, 2419, 2420, 2421, 2422, 2423, 2424, 2425, 2426, 2427, 2428, 2429, 2430, 2431, 2432, 2433, 2434, 2435, 2436, 2437, 2438, 2439, 2440, 2441, 2442, 2443, 2444, 2445, 2446, 2447, 2448, 2449, 2450, 2451, 2452, 2453, 2454, 2455, 2456, 2457, 2458, 2459, 2460, 2461, 2462, 2463, 2464, 2465, 2466, 2467, 2468, 2469, 2470, 2471, 2472, 2473, 2474, 2475, 2476, 2477, 2478, 2479, 2480, 2481, 2482, 2483, 2484, 2485, 2486, 2487, 2488, 2489, 2490, 2491, 2492, 2493, 2494, 2495, 2496, 2497, 2498, 2499, 2500, 2501, 2502, 2503, 2504, 2505, 2506, 2507, 2508, 2509, 2510, 2511, 2512, 2513, 2514, 2515, 2516, 2517, 2518, 2519, 2520, 2521, 2522, 2523, 2524, 2525, 2526, 2527, 2528, 2529, 2530, 2531, 2532, 2533, 2534, 2535, 2536, 2537, 2538, 2539, 2540, 2541, 2542, 2543, 2544, 2545, 2546, 2547, 2548, 2549, 2550, 2551, 2552, 2553, 2554, 2555, 2556, 2557, 2558, 2559, 2560, 2561, 2562, 2563, 2564, 2565, 2566, 2567, 2568, 2569, 2570, 2571, 2572, 2573, 2574, 2575, 2576, 2577, 2578, 2579, 2580, 2581, 2582, 2583, 2584, 2585, 2586, 2587, 2588, 2589, 2590, 2591, 2592, 2593, 2594, 2595, 2596, 2597, 2598, 2599, 2600, 2601, 2602, 2603, 2604, 2605, 2606, 2607, 2608, 2609, 2610, 2611, 2612, 2613, 2614, 2615, 2616, 2617, 2618, 2619, 2620, 2621, 2622, 2623, 2624, 2625, 2626, 2627, 2628, 2629, 2630, 2631, 2632, 2633, 2634, 2635, 2636, 2637, 2638, 2639, 2640, 2641, 2642, 2643, 2644, 2645, 2646, 2647, 2648, 2649, 2650, 2651, 2652, 2653, 2654, 2655, 2656, 2657, 2658, 2659, 2660, 2661, 2662, 2663, 2664, 2665, 2666, 2667, 2668, 2669, 2670, 2671, 2672, 2673, 2674, 26



WORLD • 1999

1576  
MILLER | MILLER







Figure B.6.3 Examples of the computer display "pages" included in the data reduction program. First row: TOF2/TOF1 histogram of "TRUE" events with an intensified locus (center) and an intensified broadening band around locus (right). Second row: TOF2/TOF1 "RANDOM" events (left), projection of the "RANDOM" events onto TOF1 axis (center) and projection of "TRUE" events onto TOF1 axis (right).





system is described in detail in (So-76a) (Nuclear Research Center). Only the basic operations will be described here. The main functions of the principal links are the following.

LINK 1 - Window Set Handler: This allows initial opening of the eight parameter windows by setting the lower limits to channel zero and the upper limits to 1023, which was the maximum span in all eight parameter values. The link facilitates writing or reading of the defined window sets together with all other variables of the "common" space onto or from a seven-track magnetic tape (unit #3). (The window vector is a part of the common space of each link which stays undisturbed in the memory on link changing.)

The window tape routine automatically checks the current position of the tape and moves the tape in the right direction for reading of the requested window set. It automatically moves the tape to its recorded end and assigns a new file label (window set number) when writing a new window set. The routines of Link 1 also include changing of the individual window values from the teletype. The last three routines always end by printing the values of the current window set on a line printer, including the window set number, for easy checks and keeping of reference. Link 1 does not include any data display.

LINK 2 - This allows definition of the lower and the upper limits of the neutron detector pulse height and pulse



shape. The user branches to different display pages, which contain one-dimensional NE213 pulse height spectra or two-dimensional 32 x 64 channel pulse height (energy) versus pulse shape spectra (see Fig. B.6.2, second row). All of these spectra are read (within the link) from a nine track data tape, where they were recorded as intermittent files in a chronological sequence with the event-by-event recorded files during the experiment. The definition of a circuit is accomplished by penning labels "LOWER" or "UPPER" and a subsequent channel hit. Both, the NE213 and C6D6 pulse shape windows are pulse height dependent (curved boundaries) in the off-line analysis, unlike the on-line analysis, where the NE213 pulse shape limits were defined as a single window for all pulse heights. The current values of the limits are displayed as a line of intensified points during the procedure. The whole area of the data display currently enclosed between the "LOWER" and the "UPPER" boundaries is intensified following a light pen hit of label "TOTAL". A typical "TOTAL" NE213 pulse shape window is shown in Fig. B.6.2 and as the crosshatched area in Fig. C.1.2.

Link 3 is the exact analogy of link 2 for the C6D6 detectors.

Link 4 involves both two-body and three body kinematics calculations to enable calibration of the time-of-flight spectra and its conversion into energy. These were also used to define the windows on the neutron time-of-flight and/or on the neutron energy.





The program accepts input of kinematical variables like incident deuteron beam energy, bombarding neutron and the scattered neutron angles, neutron flight distances, etc. as well as the nsec/channel time-of-flight calibration obtained with a time calibrator during the experiment. The program facilitates comparison of calculated values with the shape of the singles time-of-flight spectra from ADCP and Q. These were recorded as intermittent files on the data tape during the experiment and read from the tape within link 4. There were five more or less pronounced peaks in each of these spectra, corresponding to the  $\gamma$ -peak and the elastic n-d and n-c scattering peaks, each for two different neutron energies, 21.5 MeV and 7.9 MeV. The 7.9 MeV group of neutrons (see Fig. B.2.1.3) resulted from the  $D(d,n)^3\text{He}$  reaction on deuterium impurity in the tritium target and on deuterium imbedded in the collimators and beam stop.

Penning a certain peak of the spectrum with its subsequent identification by penning the corresponding label (gamma, De1 22 MeV, Ce1 22 MeV, De1 7.9 MeV, Ce1 7.9 MeV - see Fig. B.6.2, first row) caused intensification of channels corresponding to the calculated position of the remaining four peaks. This gave a very sensitive check of the correct calculation of the zero time-of-flight channel and its correct conversion into energy. This routine is followed by the definition of the time-of-flight and energy



windows in a way similar to that of links 2 and 3.

Finally, a calculation of the three-body kinematical locus points and its allowed limits in terms of TOF or energy is made, with respect to the time-of-flight or energy display cropping windows and stored in the "common" vector. Link 5 contains routines for the processing of the monitor spectra recorded on the 9 track data tape after each event recorded run. Routines include reading of the spectra from tape, light pen definition of the beginning and end channels of the n-d elastic peak with additional points to define the average background on the left and on the right of the peak. The channel contents within the defined peak interval are summed up and the background is interpolated under the peak area. The raw sum of the peak, the net sum (raw sum minus background) and the sum of background inside the peak area are printed out, together with the statistical errors of the sums. At the same time a peak centroid is calculated and the monitor A and monitor B spectra from the individual runs are being added into corresponding monitor spectra for the whole experiment at one geometry. The centroids of the n-d peaks are lined up into one channel for the adding. Final processing of the monitor peaks was done in these added spectra as the statistical error there was very small.

Links #6 and #7 differ only in the event playback analysis. Spectra in link 7 are formed in terms of neutron time-of-flight while in link 6 the time of flight is con-



verted into neutron energy and the spectra formed in terms of neutron 1 energy (E1) and neutron 2 energy (E2).

Eight histograms are found during the playback analysis in each of these two links. These are:

- (1) 64 x 64 channel two-dimensional display of E2 versus E1 for events which satisfied the eight parameter windows ("TRUE").
- (2) 64 x 64 channel E2 versus E1 display of background events, which failed the window tests ("RANDOM").
- (3) Spectrum of C6D6 recoil energy (pulse height) corresponding to the "TRUE" events within the allowed broadening band around the calculated kinematical locus.
- (4) Spectrum of C6D6 pulse heights for all the "RANDOM" events and for "TRUE" events lying outside the band around the locus.
- (5) and (7) Projections of "TRUE" events within the band onto the E1 and E2 axes respectively.
- (6) and (8) Projections of the "RANDOM" events and of "TRUE" events outside the band onto E1 and E2 axes respectively.

Items (1), (2) and (5) to (8) would read TOF in place of E in Link 7.

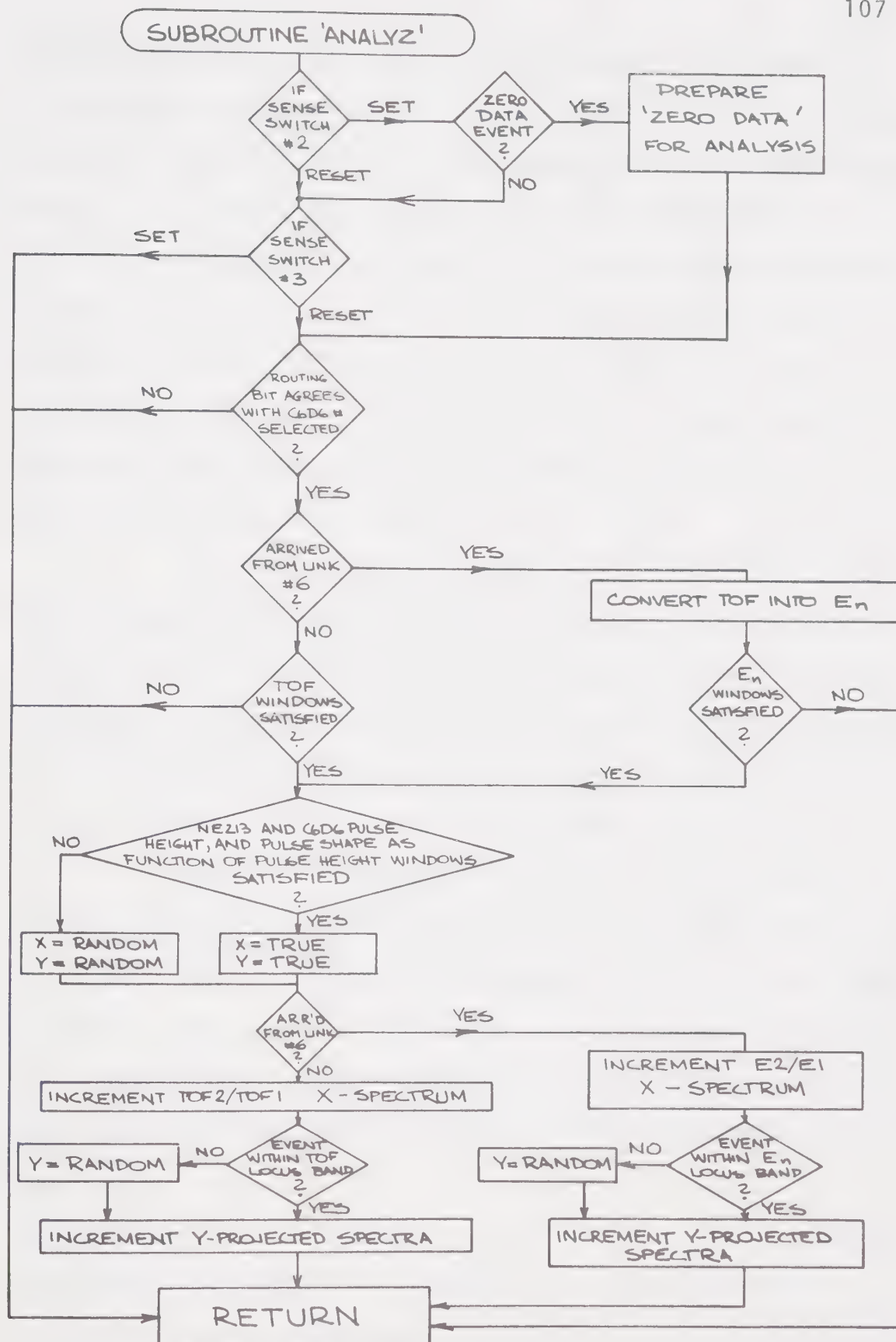
These data histograms are stored in the upper memory of the computer (indirectly accessible 16K memory core) and thus they are undisturbed by changing the links and even when other independent programs (not using upper





Figure B.6.4 A logic tree of a subroutine 'ANALYZ'  
contained in link 9 of the off-line  
data reduction program.







memory) are executed. A data histogram is selected by a light pen hit in the list of histograms on the first display page of link 6 or link 7. This transfers the selected data region into the display buffer from the upper memory.

Light pen hits can also intensify the calculated locus over the data display in histograms #1 and #2 of links 6 or 7 as well as intensify or change the band around the locus (Fig. B.6.3, first row). The locus and the band are calculated in terms of energy in link 6 and in terms of time-of-flight in link 7.

The whole sets of eight histograms can be stored on a seven track magnetic tape. Individual histograms from this tape can be added (or subtracted) with arbitrary multiplication coefficients to the corresponding histograms in the memory core according to the scheme:  $CORE = C * CORE + T * TAPE$ . The C and T are teletype input values.

The light pen control routines also include projection of the "TRUE" E2 versus E1 data within the locus band onto the locus line and grouping of the projected data into bins of 1 MeV or other size. All data sets displayed in links 6/7 can also be dumped in a matrix form on a line printer. The "AUTOMATIC PILOT" option is selected in these two links.

Link 11 contains a "HAGAR" (An-76) plotting routine modified for plotting of the kinematical locus and/or the broadening band around it. The plotter offers options of



plotting the two-dimensional data histograms as three-dimensional isometric plots or as scatter plots with optional characters corresponding to various count number levels (see Chapter C - results). It also plots one-dimensional spectra as step-like histograms, line plots, dotted line or character plots.



## C. EXPERIMENTAL RESULTS

### C.1 DEFINITION OF 8-PARAMETER WINDOWS

As mentioned earlier, different C6D6 and neutron detector biases were set in the three different experimental geometry runs. The C6D6 detector biases were set at 1/4 of the  $^{241}\text{Am}$  x-ray energy in the first run (assymmetric geometry angle pairs  $35.6^\circ$ - $34.3^\circ$ ;  $43.1^\circ$ ,  $-28.3^\circ$ ;  $52.0^\circ$ - $21.2^\circ$ ) and in the third run (symmetric angles  $28.6^\circ$ ,  $-28.6^\circ$ ;  $30.0^\circ$ ,  $-30.0^\circ$ ;  $31.4^\circ$ ,  $-31.4^\circ$ ) while in the second run (symmetric pairs  $23.8^\circ$ - $23.8^\circ$ ;  $25.0^\circ$ ,  $-25.0^\circ$ ;  $26.2^\circ$ ,  $-26.2^\circ$ ) the C6D6 bias was set at 1/3  $^{241}\text{Am}$  energy. The 1/4  $^{241}\text{Am}$  energy is equivalent to a light amplitude produced by about a 170 keV proton (Fig. B.3.3.3), whereas the 1/3  $^{241}\text{Am}$  bias is equivalent to about 220 keV proton energy. The neutron detector bias was set at  $1 \times {}^{60}\text{Co}$  Compton edge, which is equivalent to 3.5 MeV neutron energy, in the first run and at 1/3  $\text{Na}^{22}$  annihilation gamma ray Compton edge corresponding to about 1 MeV neutron energy in the second and third runs.

The lower C6D6 and NE213 pulse height window limits were defined (by light pen in the GOLDPAN program) at the electronics cut-off channels corresponding to the above biases. Fig. C.1.1 shows a typical neutron detector pulse height versus pulse shape spectrum at the  ${}^{60}\text{Co}$  bias in the first run. Fig. C.1.2 displays such spectrum at the 1/3  $\text{Na}^{22}$





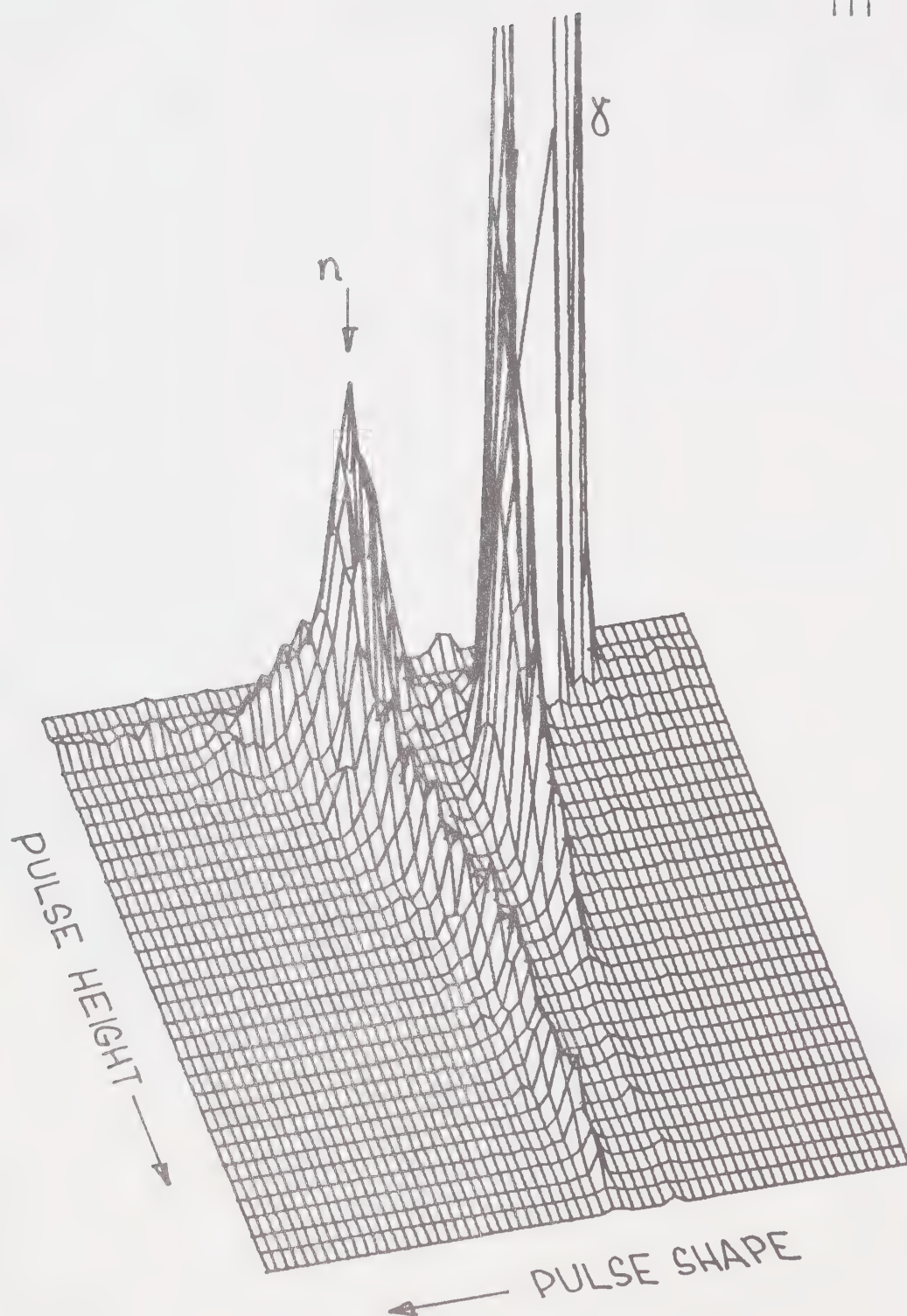


Figure C.1.1 A two-dimensional plot of pulse height versus pulse shape of an NE213 detector at the lower bias of  $1 \times {}^{60}\text{Co}$  in Run #1.





Figure C.1.2 A two-dimensional plot of pulse height versus pulse shape of an NE213 detector at the lower bias of  $1/2$   $^{22}\text{Na}$  in Runs #2 and #3 (top). The crosshatched area indicates a typical pulse shape window. A corresponding pulse height spectrum of a  $^{22}\text{Na}$  source (bottom).

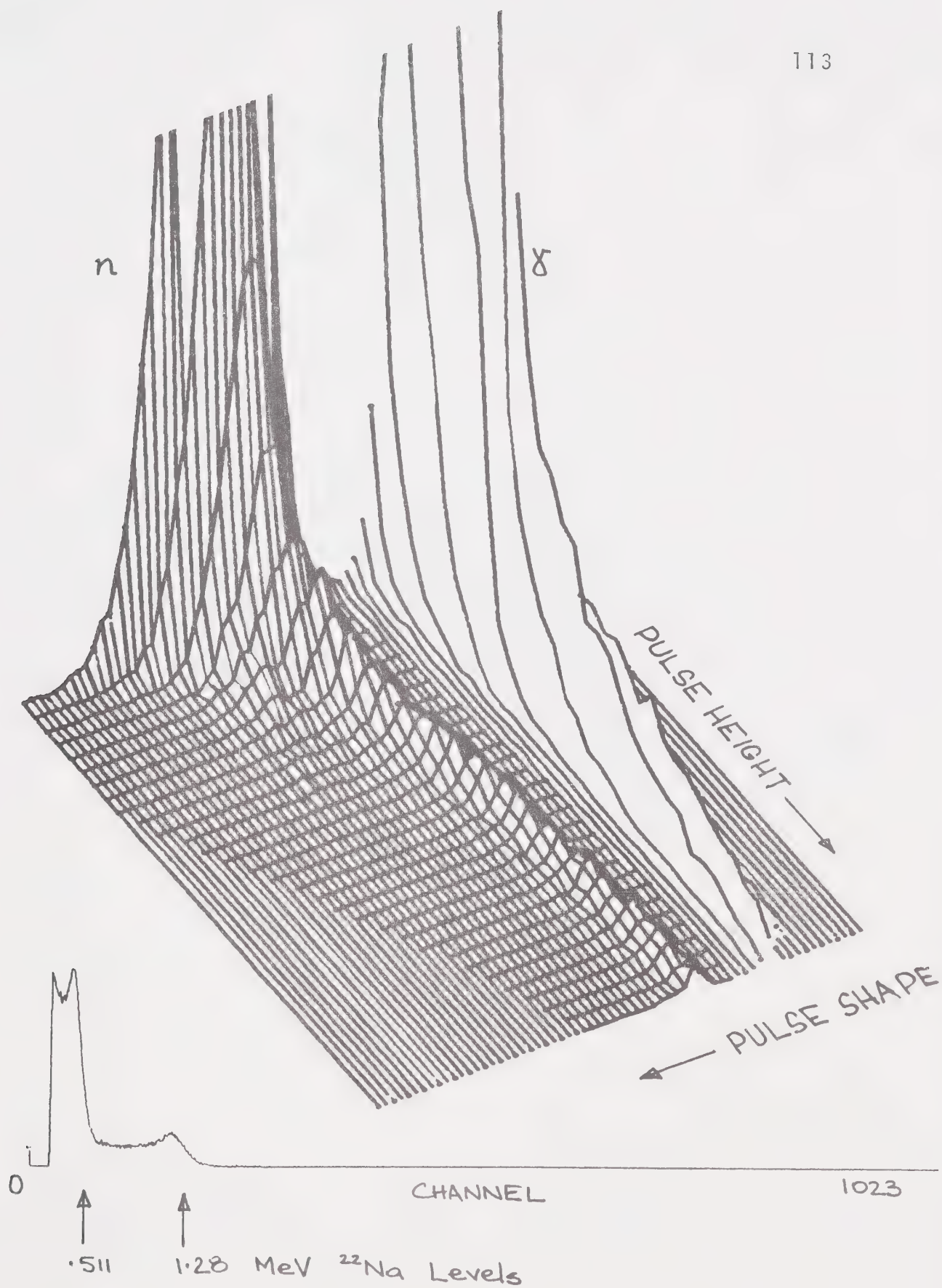
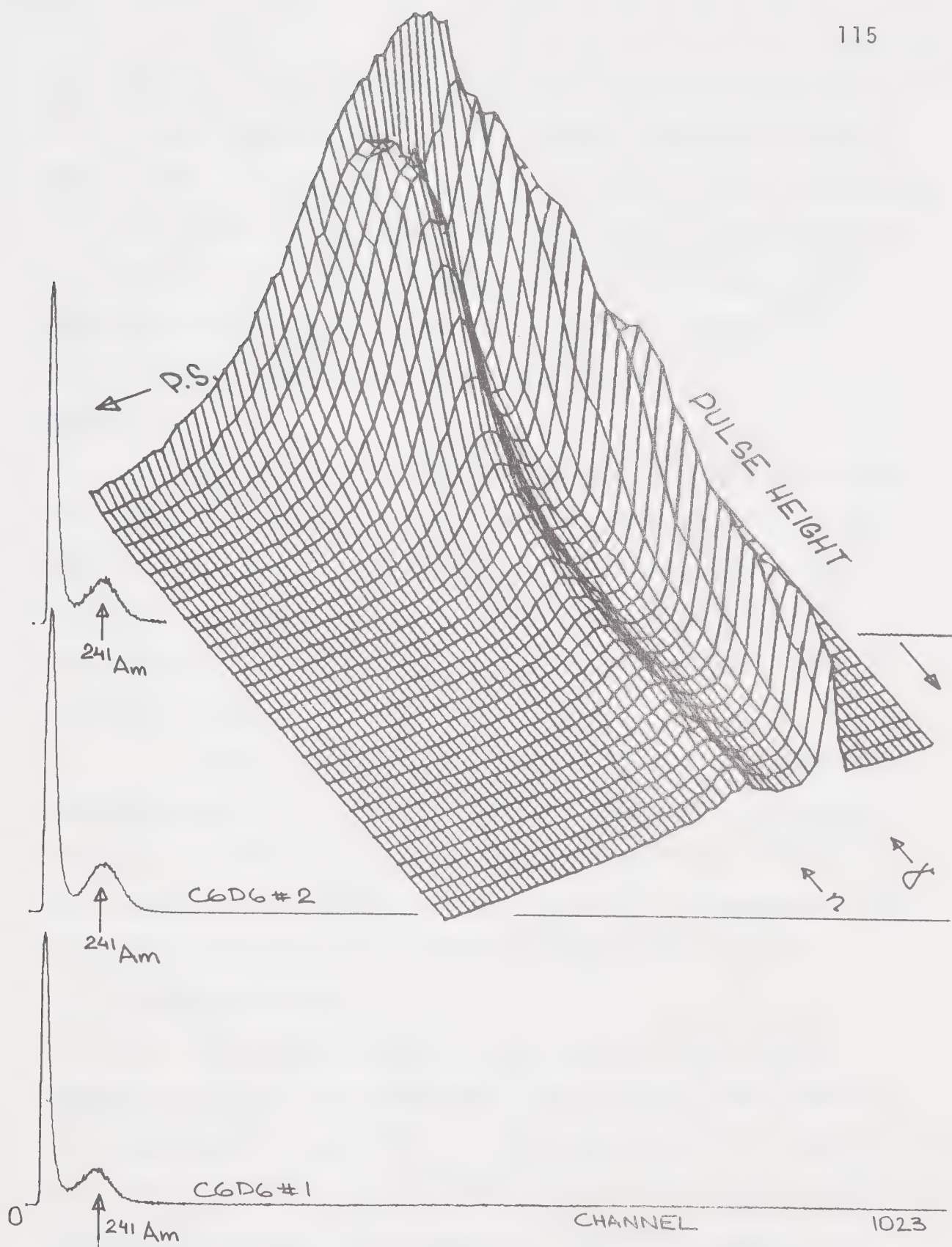






Figure C.1.3 A two-dimensional plot of pulse height versus pulse shape of a C6D6 (NE230) detector at the lower bias of  $1/4$   $^{241}\text{Am}$  (inset). Routed  $^{241}\text{Am}$  source - pulse height spectra in the three C6D6 detectors used simultaneously (under inset).







bias setting, the cross hatched area in the energy versus pulse shape spectrum indicating a typical neutron detector pulse shape window. In addition, it shows the one dimensional  $^{22}\text{Na}$  pulse height spectrum in the lower part of the picture. Fig. C.1.3 shows a typical C6D6 pulse height versus pulse shape spectrum together with the 3-detector routed  $^{241}\text{Am}$  source pulse height calibration spectra at  $1/4 \times ^{241}\text{Am}$  bias setting.

The time-of-flight windows were defined to crop out the region of interest extending from 2 MeV neutron energy in the first run and 1 MeV neutron energy in the second run up to beyond the gamma ray peak. This corresponded to approximately a 400 channel region in each time-of-flight spectrum which was grouped into 64 channels.

In the conversion of time of flight into energy the neutron energy limits were defined to cover a 16 MeV range from 2 to 18 MeV in the first run and from 1 to 17 MeV in the second and third runs. Thus 4 channels corresponded to a 1 MeV bin in the E2 versus E1 histograms and in their  $E_{1,2}$ -axes projections.

The neutron detector pulse shape restrictions together with the three detector bias settings were found sufficient in the rejection of background, while no appreciable effect has been observed due to the C6D6 detector pulse shape restrictions. Thus these were left wide open.



## C.2 SOURCES OF BACKGROUND IN THE EXPERIMENT

In addition to the "TRUE"  $D(n,2n)p$  break up events confined to a kinematical locus in the TOF2 versus TOF1 plot, indicated as curve #1 in Figs. C.2.1 and C.2.2, a number of background processes produce random coincidence bands and areas in the TOF2 versus TOF1 or E2 versus E1 plots. Appreciable ones are the following:

- (a) A random coincidence of an elastically scattered neutron from a Deuteron or Carbon nucleus, in the C6D6 detector ( $D(n,n)D$  or  $C(n,n)C$ ), detected in one neutron detector, with a generally uncorrelated gamma ray (mostly) or a neutron from the target room background in the other neutron detector. While the energy or time of flight of the elastically scattered neutron are confined to one value, given by the incident energy and the scattering angle of the detector, the time-of-flight corresponding to an uncorrelated pulse in the other neutron detector can have any value. The result are two crossing straight bands parallel to the TOF or energy axes at the energy or TOF value corresponding to the  $n$ -D elastic scattering. They are indicated as lines #2, #3 in Fig. C.2.1 and C.2.2.
- (b) A similar pair of crossing bands is caused by the random coincidence of a gamma ray, originating in the C6D6 detector and detected in one neutron detector, with a generally uncorrelated pulse in the other neutron detec-

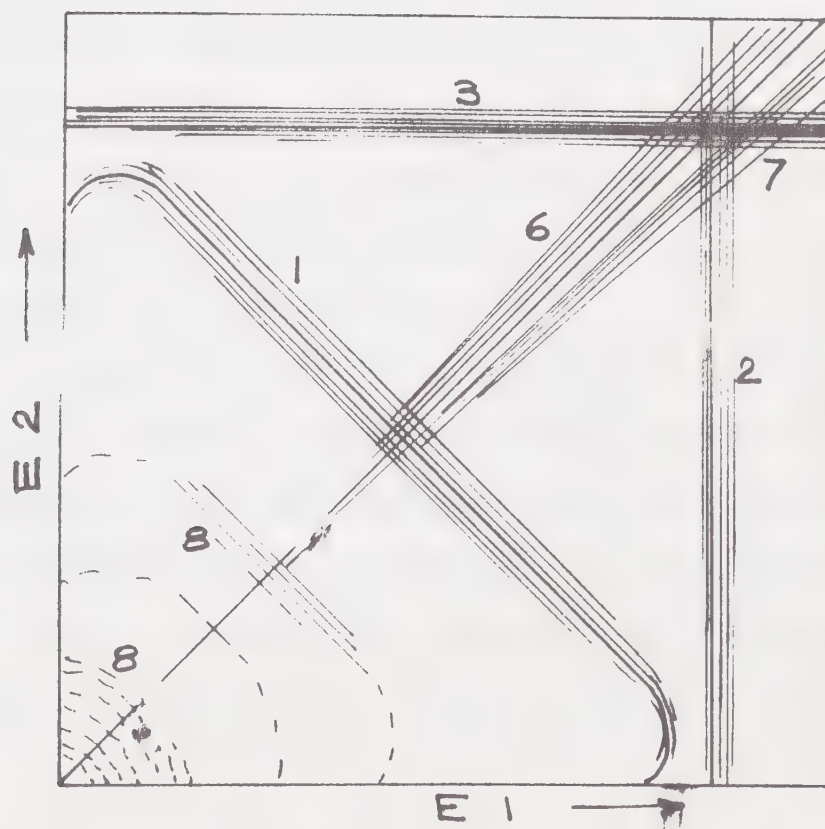
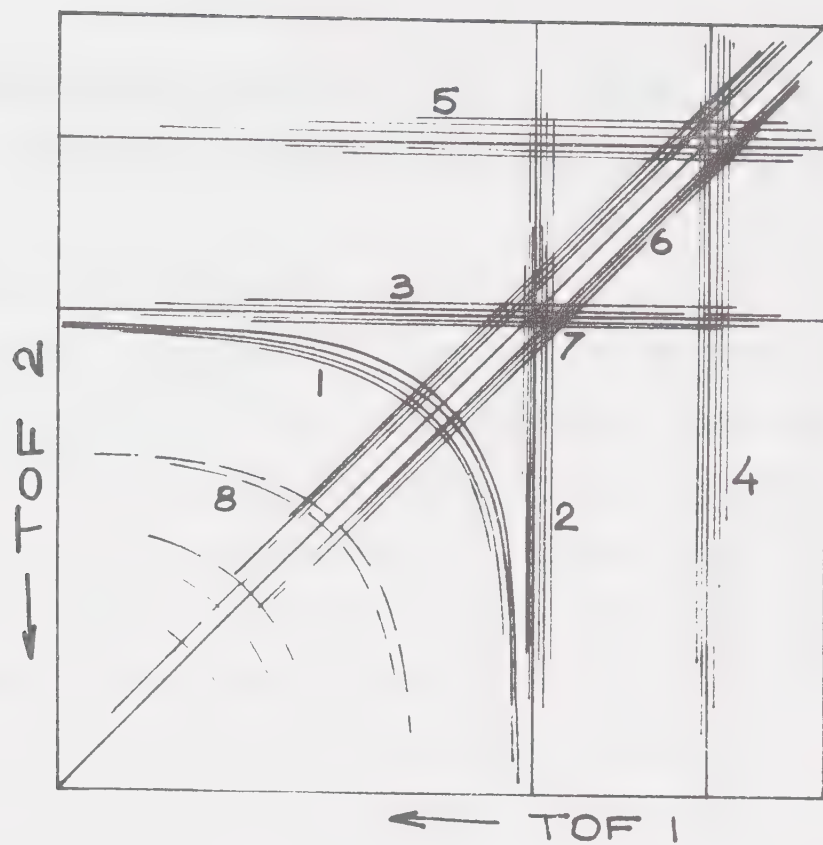




Figure C.2.1 Various true and background coincidence loci (explained in Chapter C.2) as they appear in a TOF2 versus TOF1 plot.

Figure C.2.2 Various true and background coincidence loci (explained in Chapter C.2) as they appear in an  $E_2$  versus  $E_1$  plot.







tor. Such bands (#4, #5 in Fig. C.2.1) intersect the TOF axes at the TOF values corresponding to the gamma ray peak.

- (c) A coincidence caused by the sequence of a neutron scattering in the C6D6 detector and its  $C(n, n' - \gamma)$  or  $C(n, 3\alpha - \gamma)$  inelastic interactions in one of the neutron detectors with the gamma ray produced hitting the other neutron detector. The same can occur with a gamma ray originating in the C6D6 detector and subsequently Compton scattering from one neutron detector to the other. As the time-of-flight of the gamma ray from one neutron detector to the other is negligible, effectively a coincidence event with equal time-of-flight values from both neutron detectors is created. In case of a symmetric neutron detector geometry these events will lie on a diagonal line  $TOF_2 = TOF_1$  or  $E_2 = E_1$ , respectively (#6 in Fig. C.2.1 and C.2.2). More precisely, these should be two parallel diagonal lines separated by the gamma ray time-of-flight between the two neutron detectors.

The background coincidence probability is higher where the bands described intersect each other causing a background enhancement at such locations (see Fig. C.3.2.4). One of these peaks was used in the analysis as an added check of the correct energy calibration. The calculated crossing position of the two n-D elastic scattering bands (#7 in Fig.



C.2.1, C.2.2) was intensified as a three channel corner together with the calculated  $D(n,2n)p$  locus in the TOF2-TOF1 or E2/E1 display spectra (Fig. B.6.3, first row, center).

Background sources a, b and c were somewhat suppressed in the first run as compared to runs #2 and #3; a - because of the C6D6 dynamic range excluding the elastic deuteron recoil, b and c - because the higher neutron detector bias in this run wiped out lower energy secondary  $\gamma$ -events and the assymmetric geometry dissolved whatever was left to create the diagonal band.

(d) The above discussed bands can also occur for other incident neutron energy groups if present in the bombarding neutron spectrum. This includes the corresponding additional  $d(n,2n)p$  loci parallel to the main breakup energy locus (#8 in Fig. C.2.1, C.2.2). In our case the bombarding neutron spectrum contained a small impurity of 7.9 MeV discrete energy and a low energy continuum groups (see Fig. B.2.1.3).

While the background sources a, b, c can be rejected very efficiently by the neutron detector pulse shape restrictions (these events mostly involve at least one  $\gamma$ -ray) the additional breakup background source d can not be easily rejected by the eight-parameter windows as these events are pure  $d(n,2n)p$  events, at different incident energy. However, the impurity of other neutron groups was almost negligible and, more over, the additional bands were well separated kinema-



tically in the E2/E1 spectrum. They were excluded in the projection of the data by defining a kinematically allowed broadening band around the main breakup locus and projecting the data only from this band. The corresponding projection band is displayed as the cross hatched area in the isometric plots of the data in the following chapters.





### C.3 PLAYBACK OF THE EVENT RECORDED DATA WITH ANALYSIS IN TERMS OF THE NEUTRON TIME-OF-FLIGHT

Typical 64 x 64 channel TOF2 versus TOF1 two-dimensional data histograms are presented in two forms:

a - as three-dimensional isometric plots

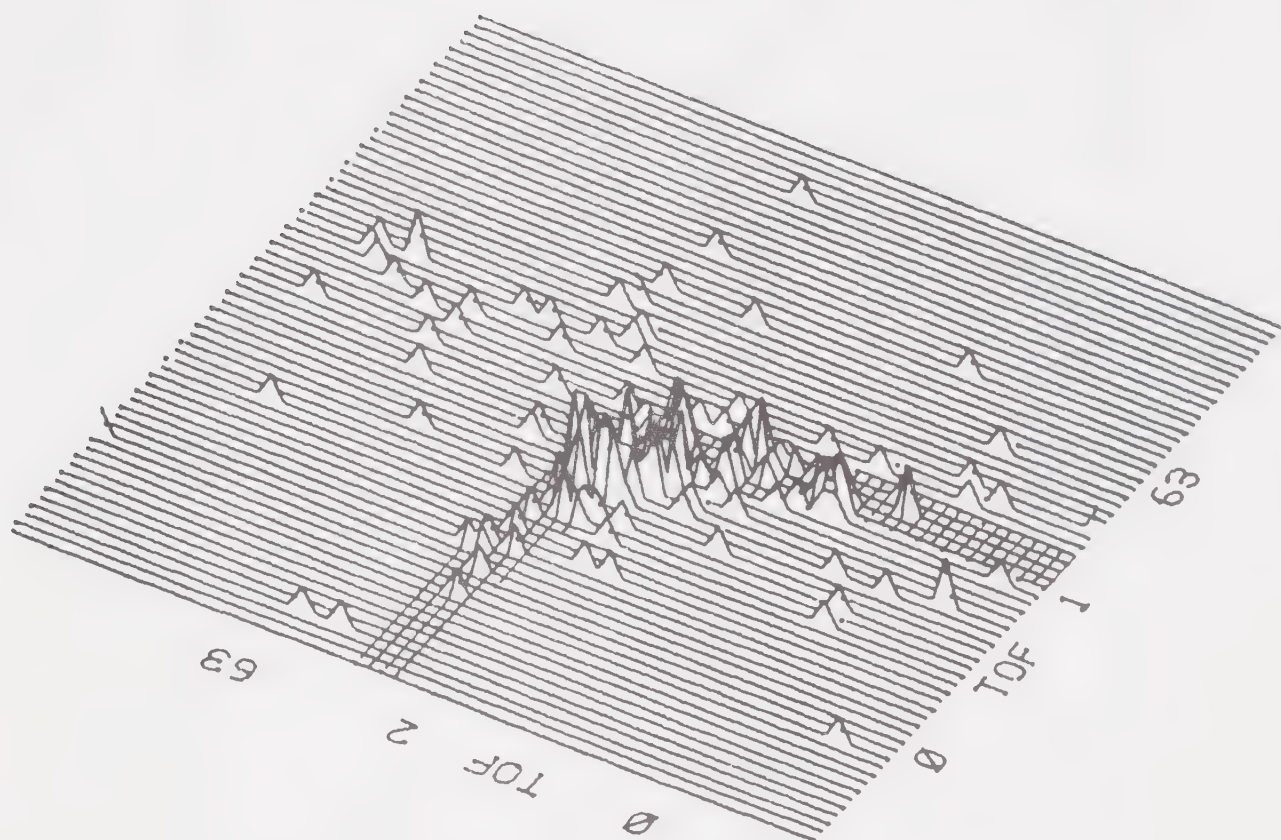
b - as two-dimensional scatter plots.

Both the histograms of events accepted by the eight parameter window sets, named "TRUE" or "ACCEPTED", as well as the rejected events ("RANDOM" or "REJECTED") are displayed for one geometry representing each of the three QFS runs.

The crosshatched band in the three-dimensional isometric plots indicates the broadening band around the kinematical locus and the dotted line indicates the locus curve in the scatter plots.



C.3.1 Run # 1.



QFS 200 TRUE  
190 EVENTS

35, -35  
4 MAX

Figure C.3.1.1 TOF2 x TOF1 isometric plot of "TRUE" events in  $35^\circ$ ,  $-35^\circ$  q.f.s. Run #1.



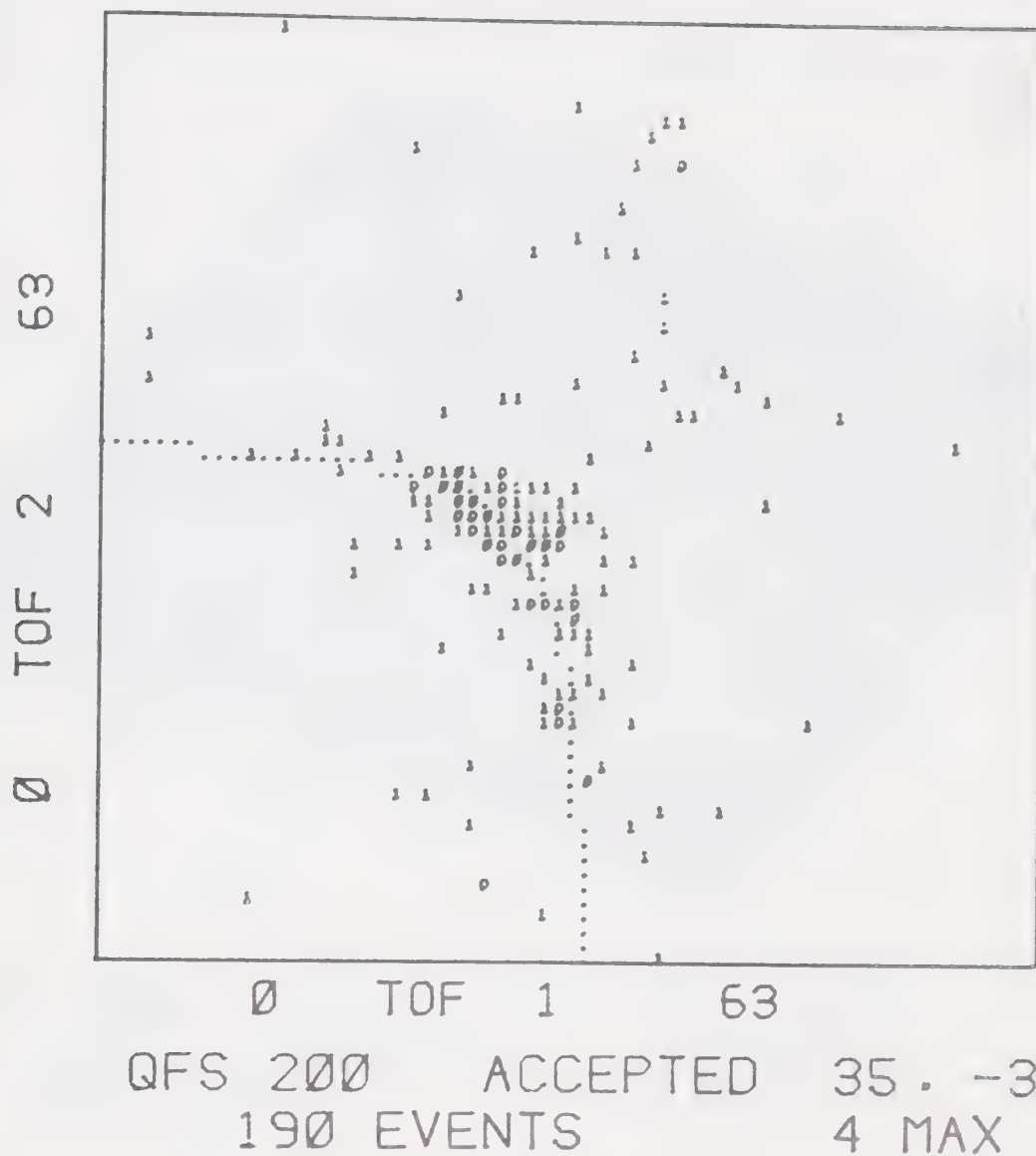
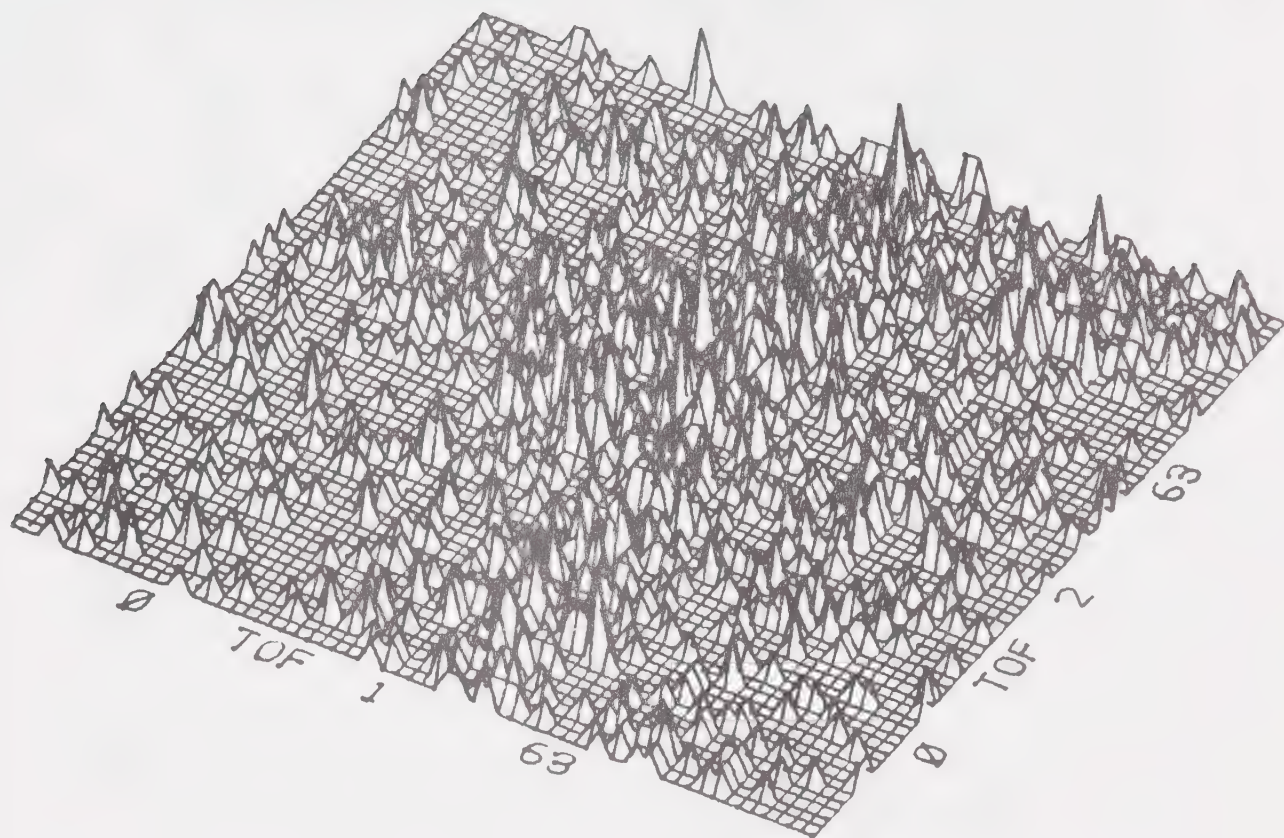


Figure C.3.1.2 TOF2 x TOF1 scatter plot of "TRUE" events  
in  $35^\circ$ ,  $-35^\circ$  q.f.s. Run #1.





QFS 200      RANDOMS      35, -35  
1519 EVENTS      6 MAX

Figure C.3.1.3 TOF2 x TOF1 isometric plot of background coincidences in 35°, -35° q.f.s. Run #1.





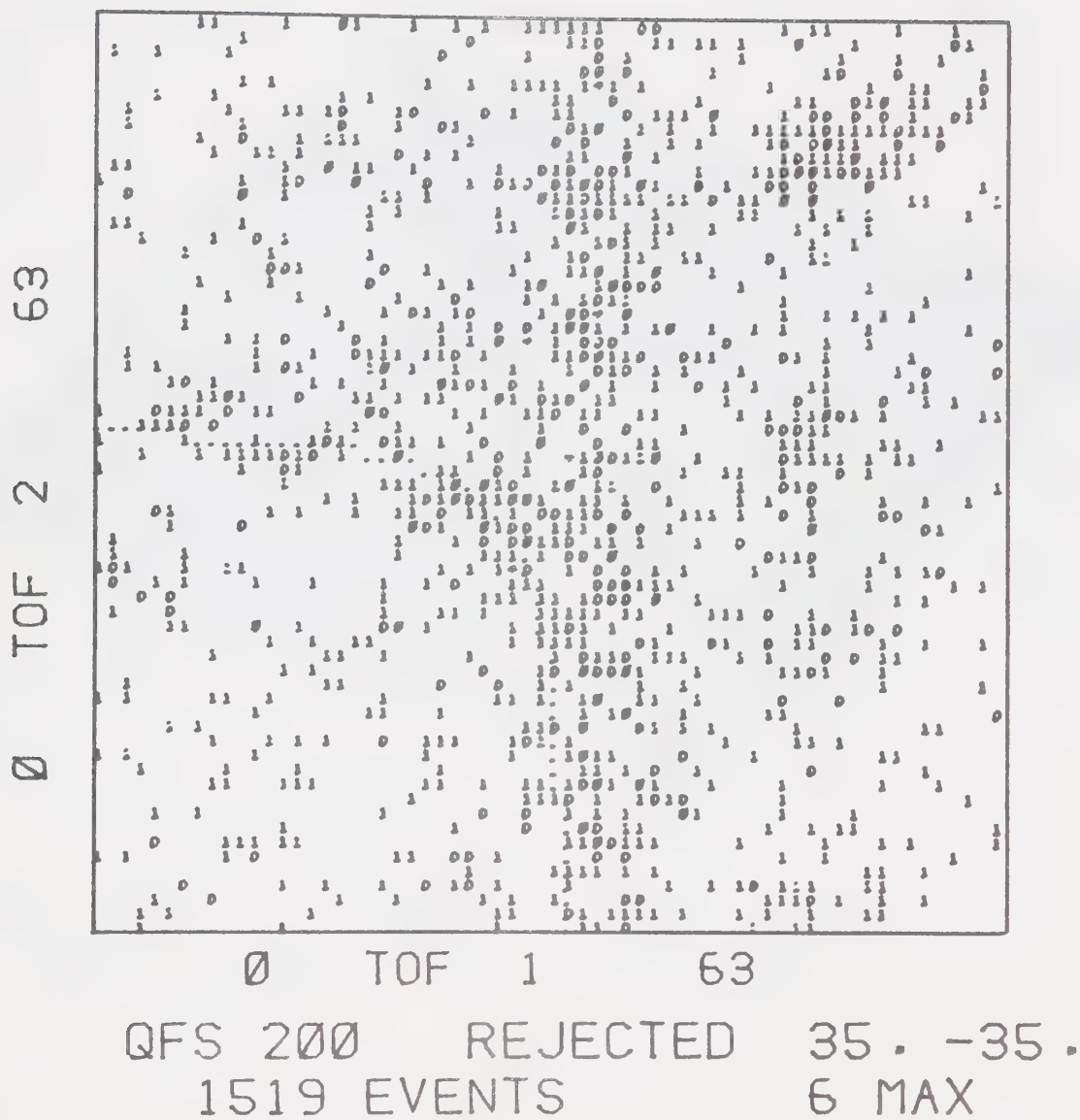
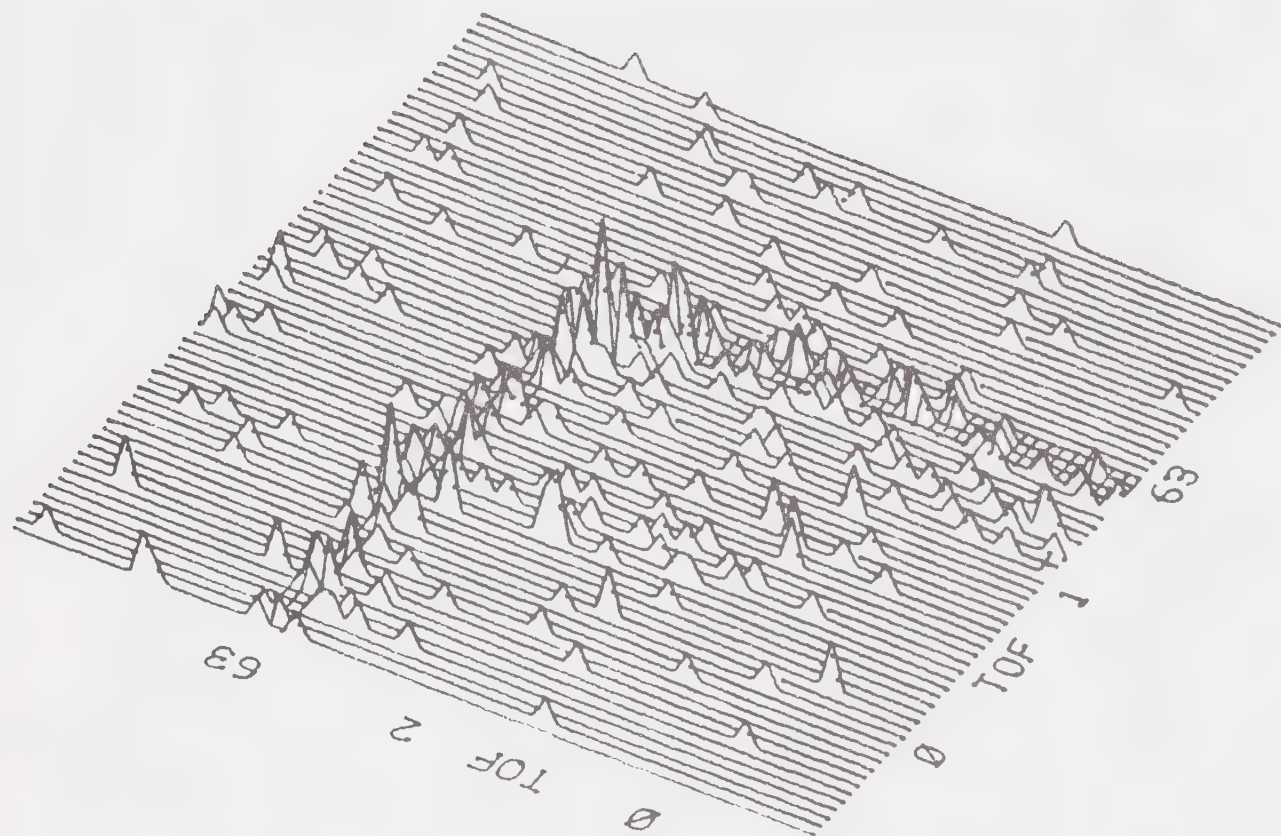


Figure C.3.1.4 TOF2 x TOF1 scatter plot of background coincidences in  $35^\circ$ ,  $-35^\circ$  q.f.s. Run #1.



C.3.2 Run # 2.



DBS 500            TRUE            25. -25.  
319 EVENTS            6 MAX

Figure C.3.2.1 TOF2 x TOF1 isometric plot of "TRUE" events in  $25.0^\circ$ ,  $-25.0^\circ$  q.f.s. Run #2.



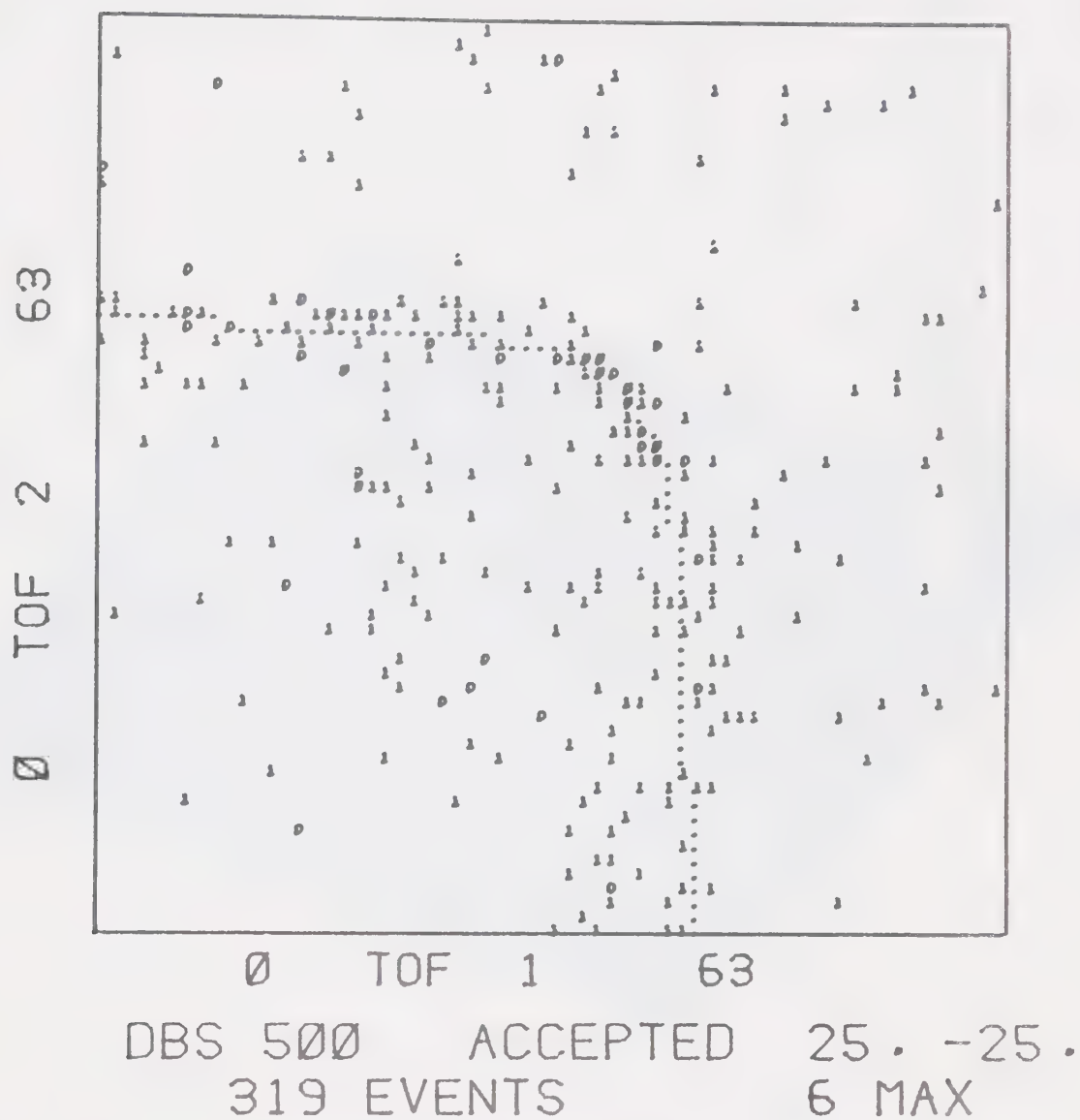
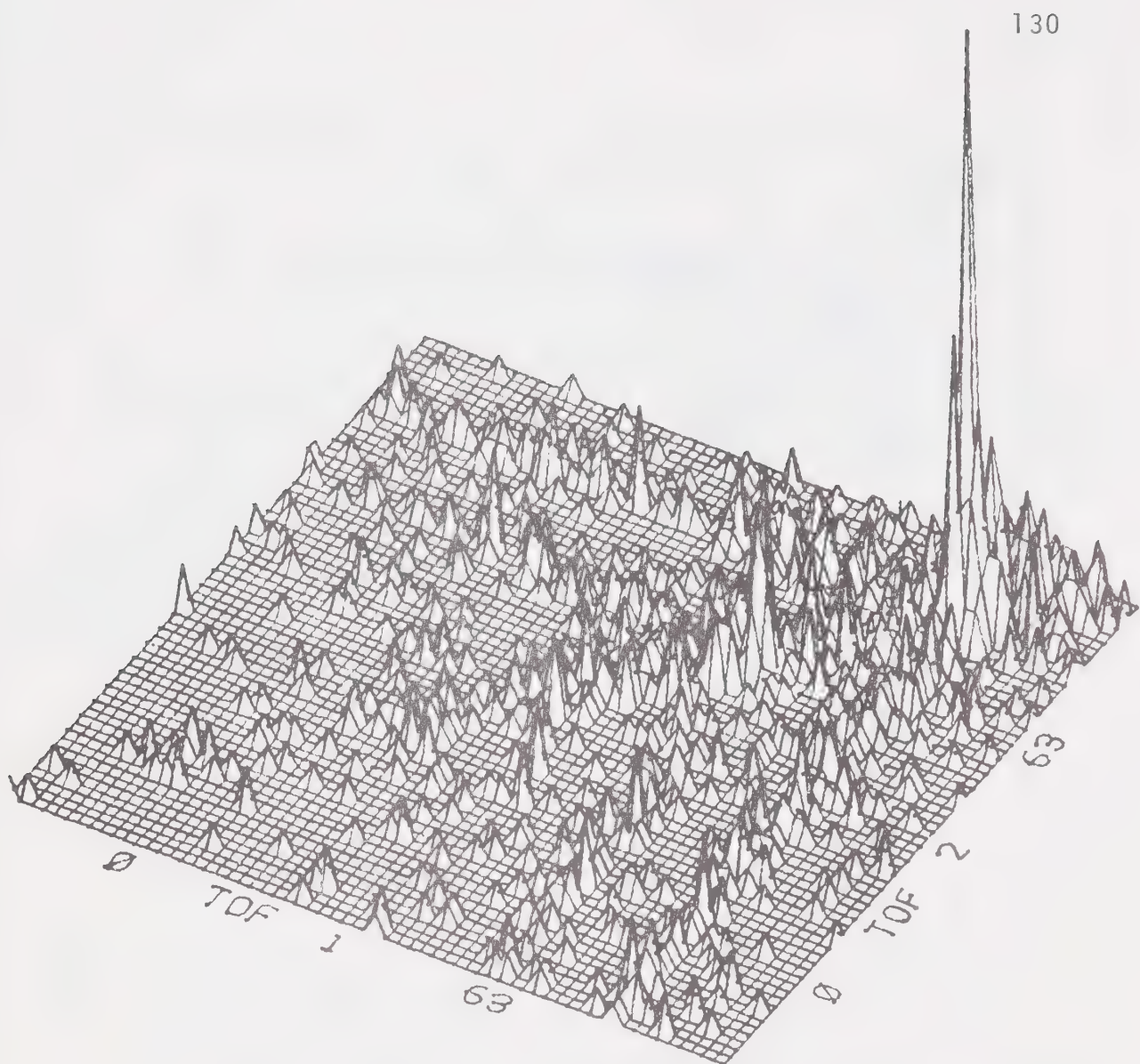


Figure C.3.2.2 TOF2 x TOF1 scatter plot of "TRUE" events in  $25.0^\circ$ ,  $-25.0^\circ$  q.f.s. Run #2.





DBS 500      RANDOMS      25. -25.  
 1370 EVENTS      29 MAX

Figure C.3.2.3 TOF2 x TOF1 isometric plot of background coincidences in  $25.0^\circ$ ,  $-25.0^\circ$  q.f.s. Run #2.





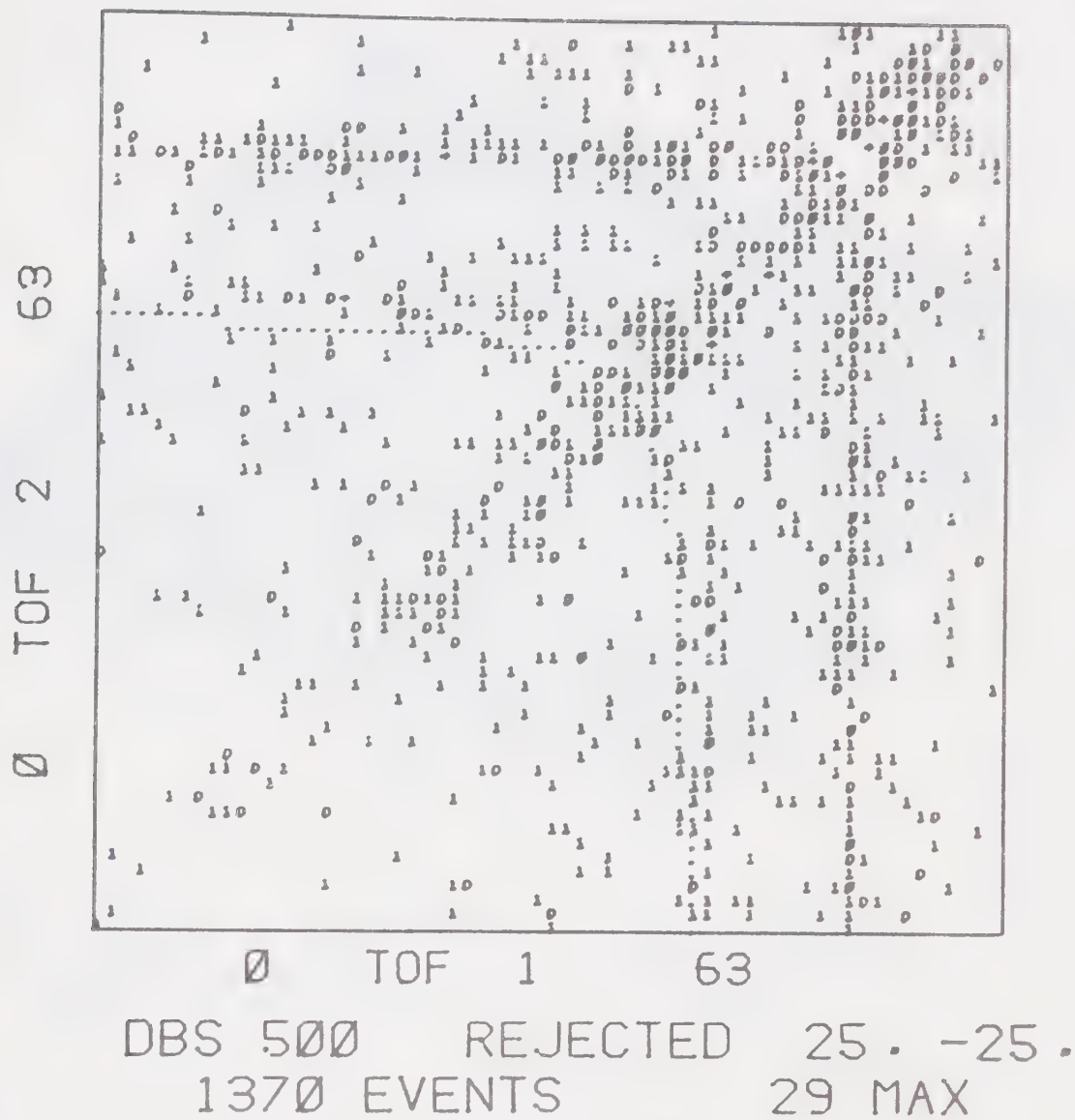
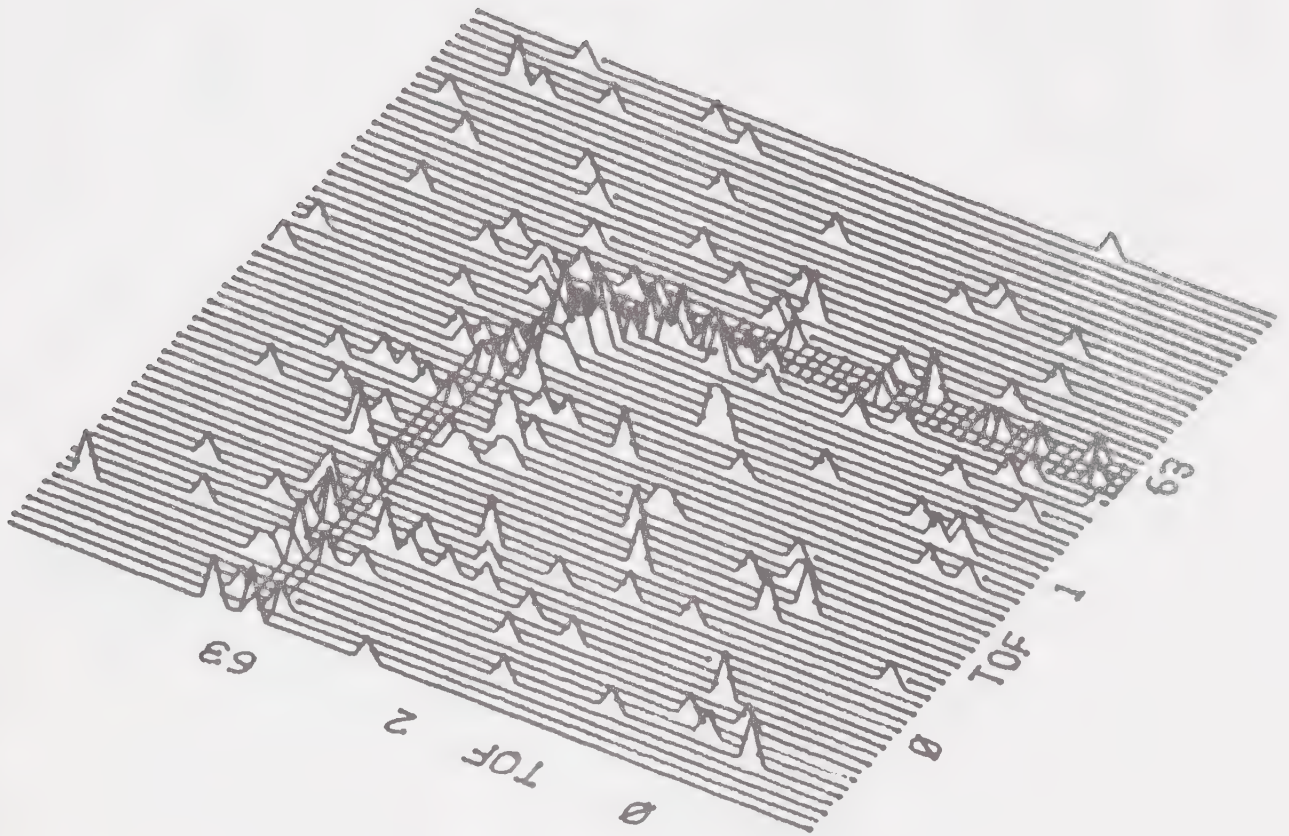


Figure C.3.2.4 TOF2 x TOF1 scatter plot of background coincidences in  $25.0^\circ$ ,  $-25.0^\circ$  q.f.s. Run #2.



C.3.3 Run # 3.



DBS 600      TRUE      30, -30.  
218 EVENTS      3 MAX

Figure C.3.3.1 TOF2 x TOF1 isometric plot of "TRUE" events in 30.0°, -30.0° q.f.s. Run #3.



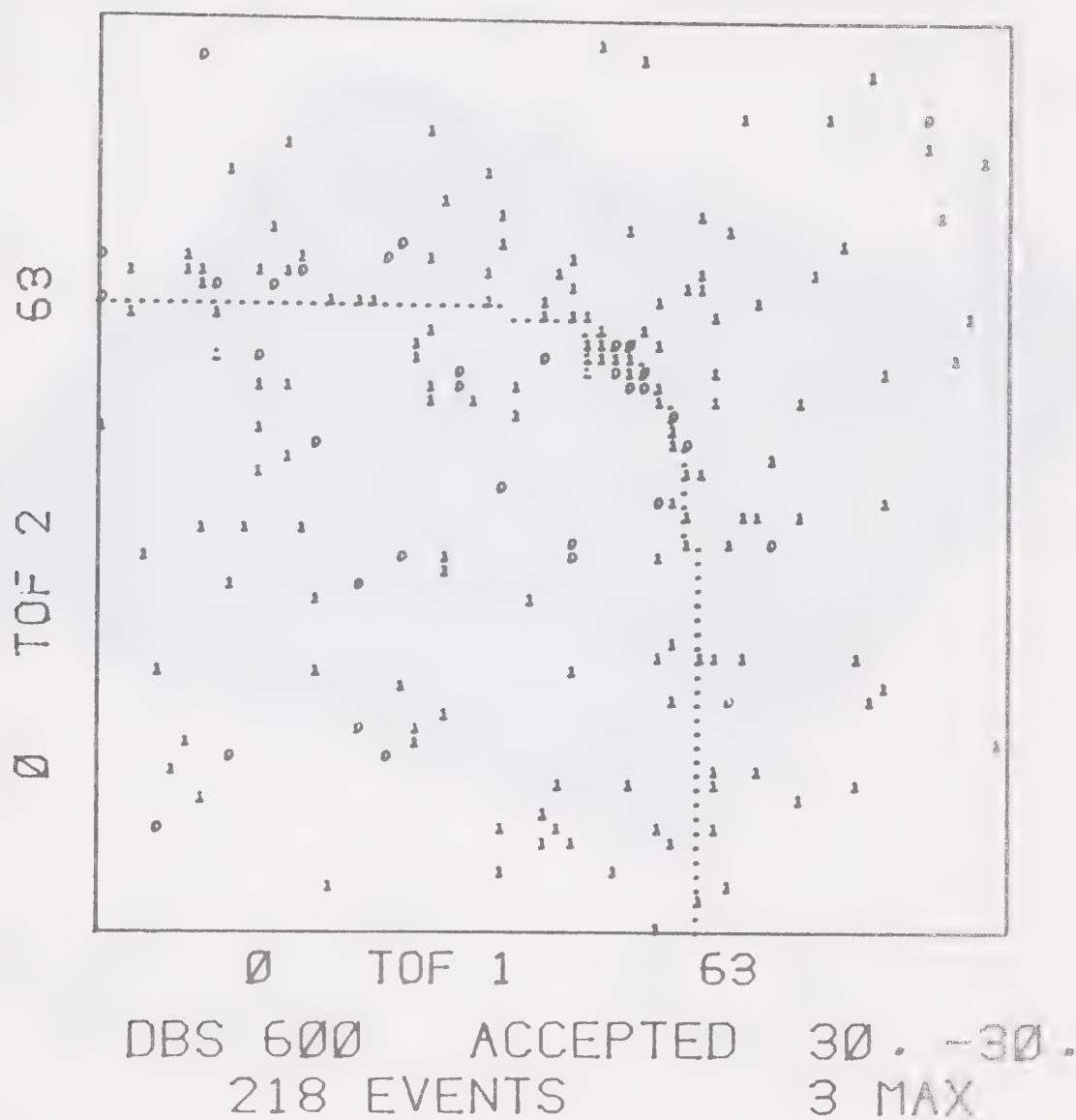
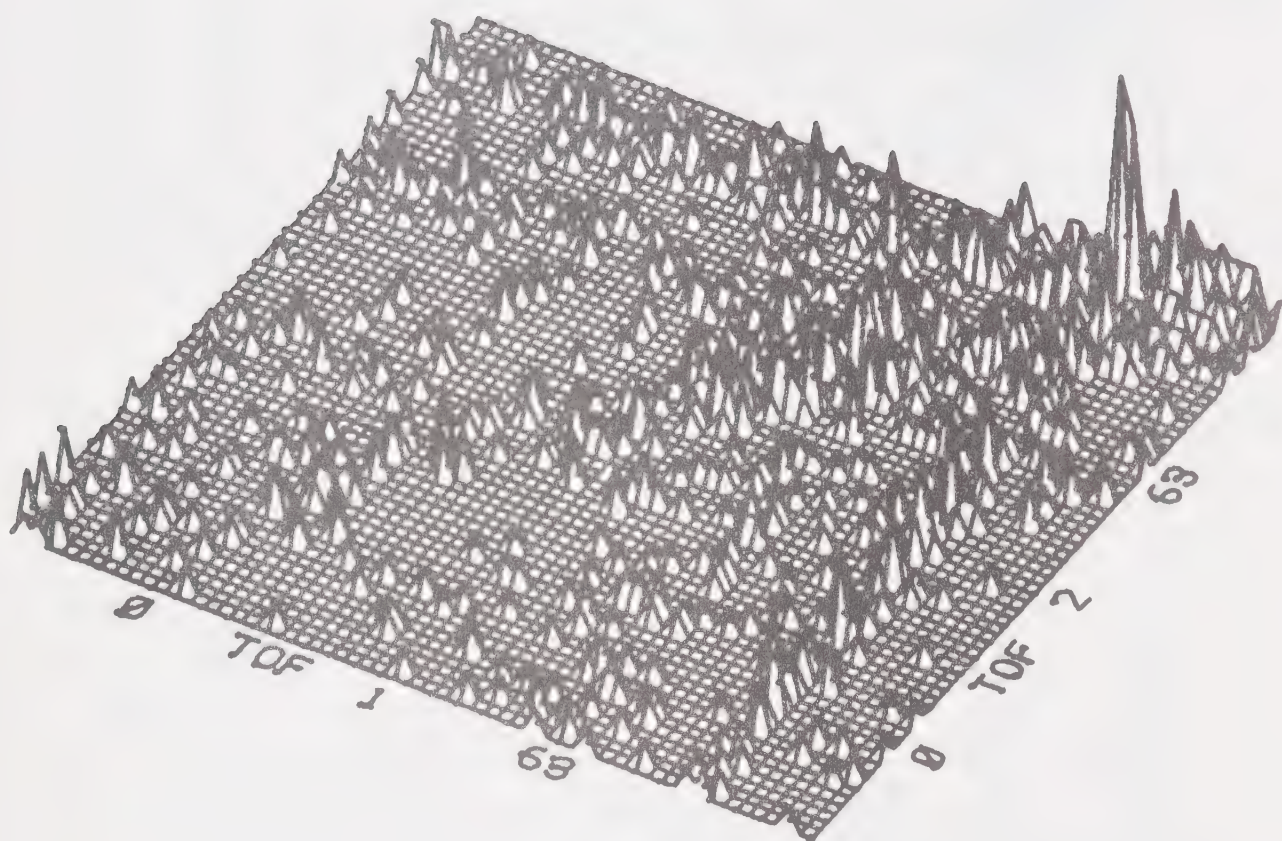


Figure C.3.3.2 TOF2 x TOF1 scatter plot of "TRUE" events in  $30.0^\circ$ ,  $-30.0^\circ$  q.f.s. Run #3.







DBS 600      RANDOMS      30, -30.  
996 EVENTS      11 MAX

Figure C.3.3.3 TOF2 x TOF1 isometric plot of background coincidences in  $30.0^\circ$ ,  $-30.0^\circ$  q.f.s. Run #3.





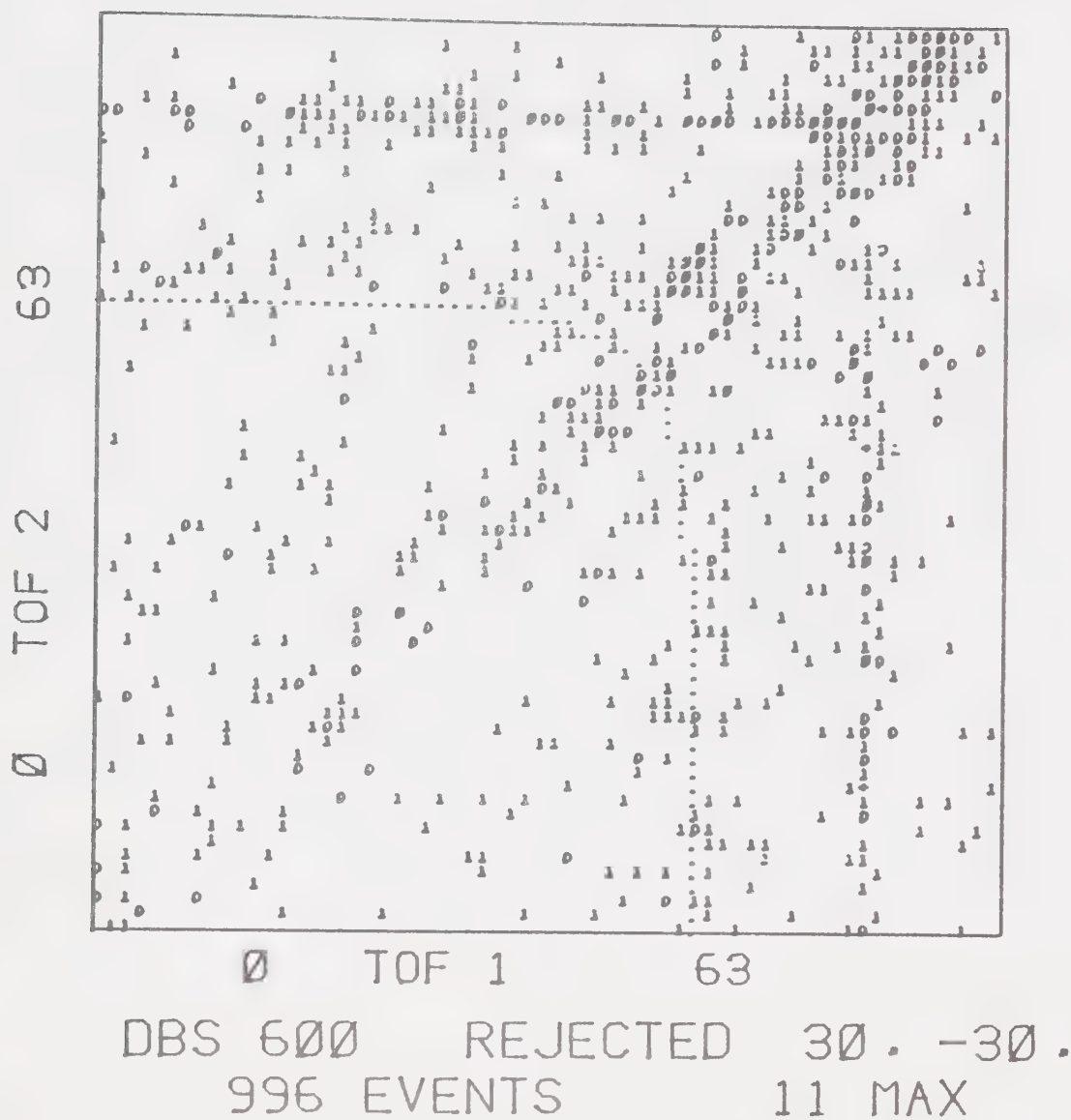


Figure C.3.3.4 TOF2 x TOF1 scatter plot of background coincidences in  $30.0^\circ$ ,  $-30.0^\circ$  q.f.s. Run #3.



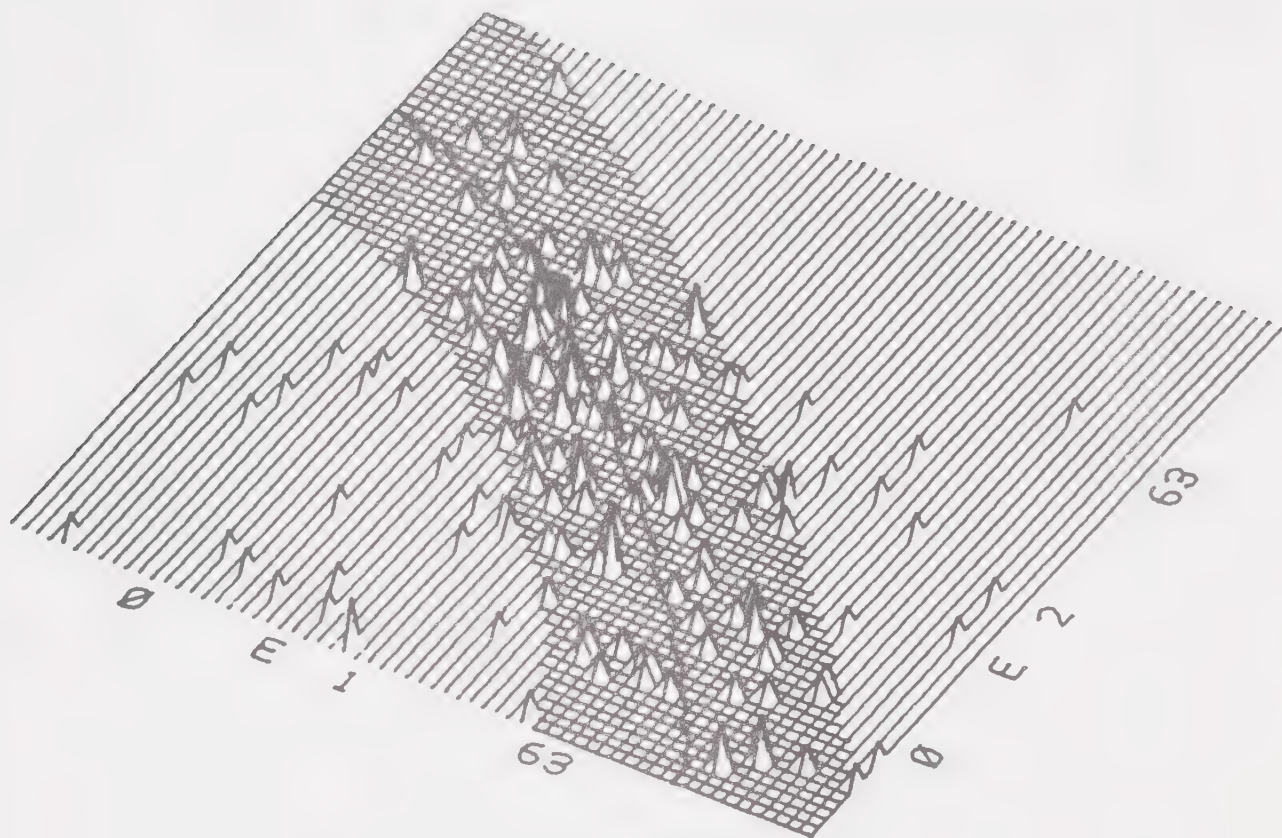
#### C.4 OFF LINE ANALYSIS OF THE EVENT RECORDED DATA

64 x 64 channel E2 versus E1 data histograms of the "TRUE" events are presented as three-dimensional isometric plots and also as two-dimensional scatter plots. One channel on each energy axis corresponds to 1/4 MeV interval, the scale covering the ranges from 2 MeV to 18 MeV in Run #1 and from 1 MeV to 17 MeV in Runs #2 and 3.

The crosshatched area in the isometric plots indicates the broadening band around the kinematical locus from which the data were projected onto either of the energy axes or onto a  $45^\circ$  straight line tangent to the locus at the QFS peak position. The solid curve in the isometric plots and a dotted line in the scatter plot indicate the kinematical locus of the mean scattering geometry. Only one representative QFS geometry is presented for each of the three runs.



C.4.1 Run # 1.



QFS 100 ACCEPTED 35 . -35 .  
186 EVENTS 3 MAX

Figure C.4.1.1 E2 x E1 isometric plot of "TRUE" events in 35°, -35° q.f.s. Run #1.



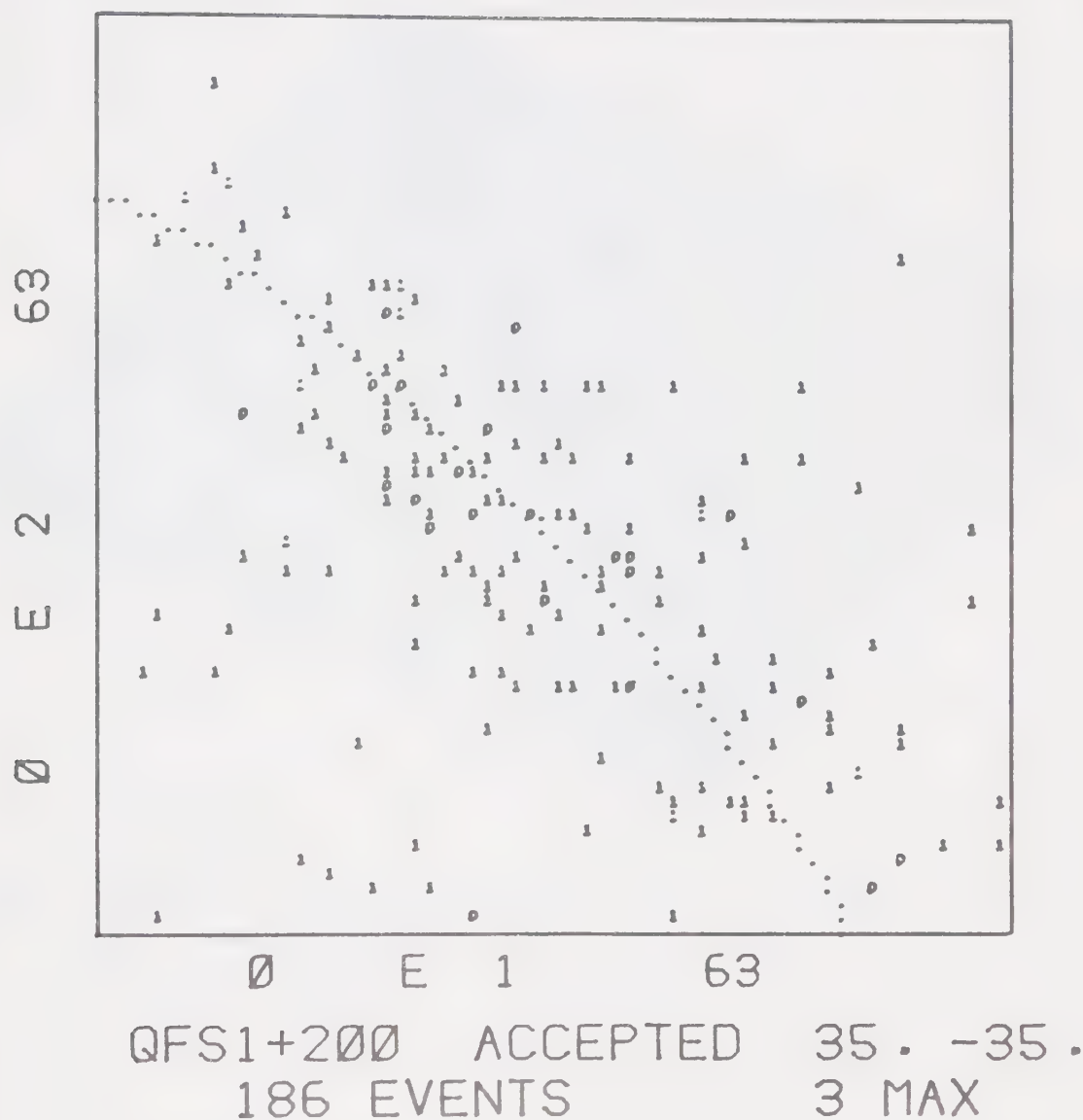
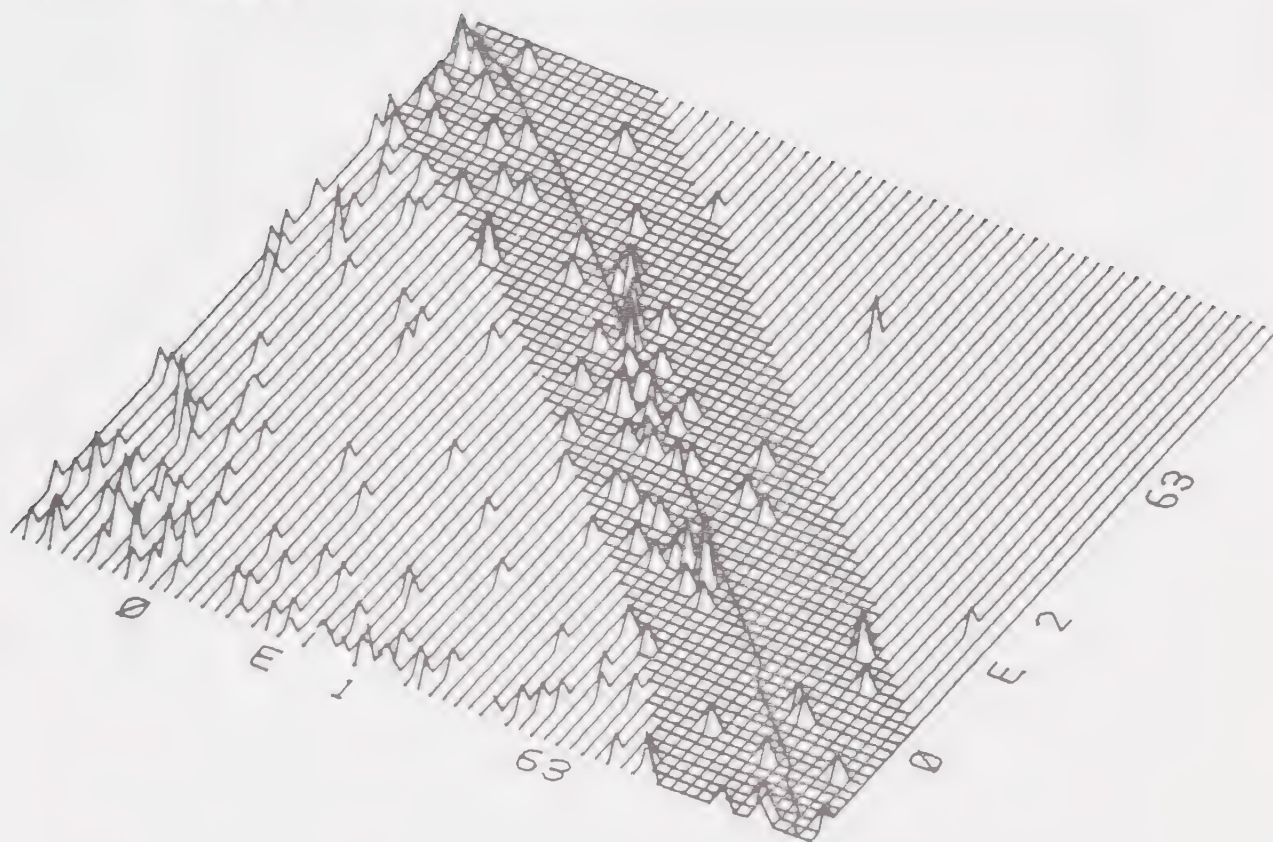


Figure C.4.1.2 E2 x E1 scatter plot of "TRUE" events in 35°, -35° q.f.s. Run #1.





C.4.2 Run # 2.



DBS 500      ACCEPTED      25. -25.  
 204 EVENTS                      3 MAX

Figure C.4.2.1 E2 x E1 isometric plot of "TRUE" events in 25.0°, -25.0° q.f.s. Run #2.



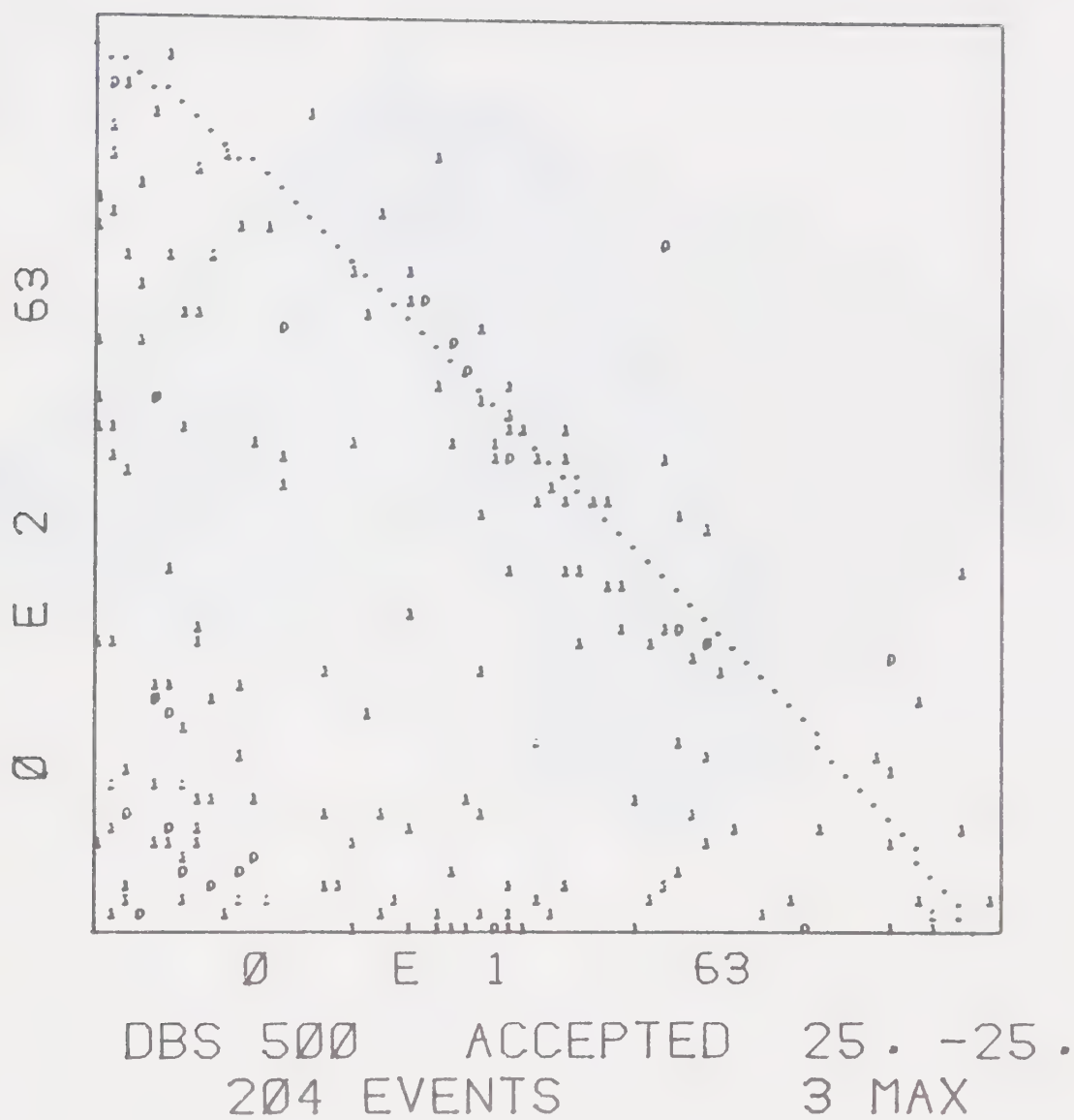


Figure C.4.2.2 E2 x E1 scatter plot of "TRUE" events in 25.0°, -25.0° q.f.s. Run #2.



C.4.3 Run # 3.

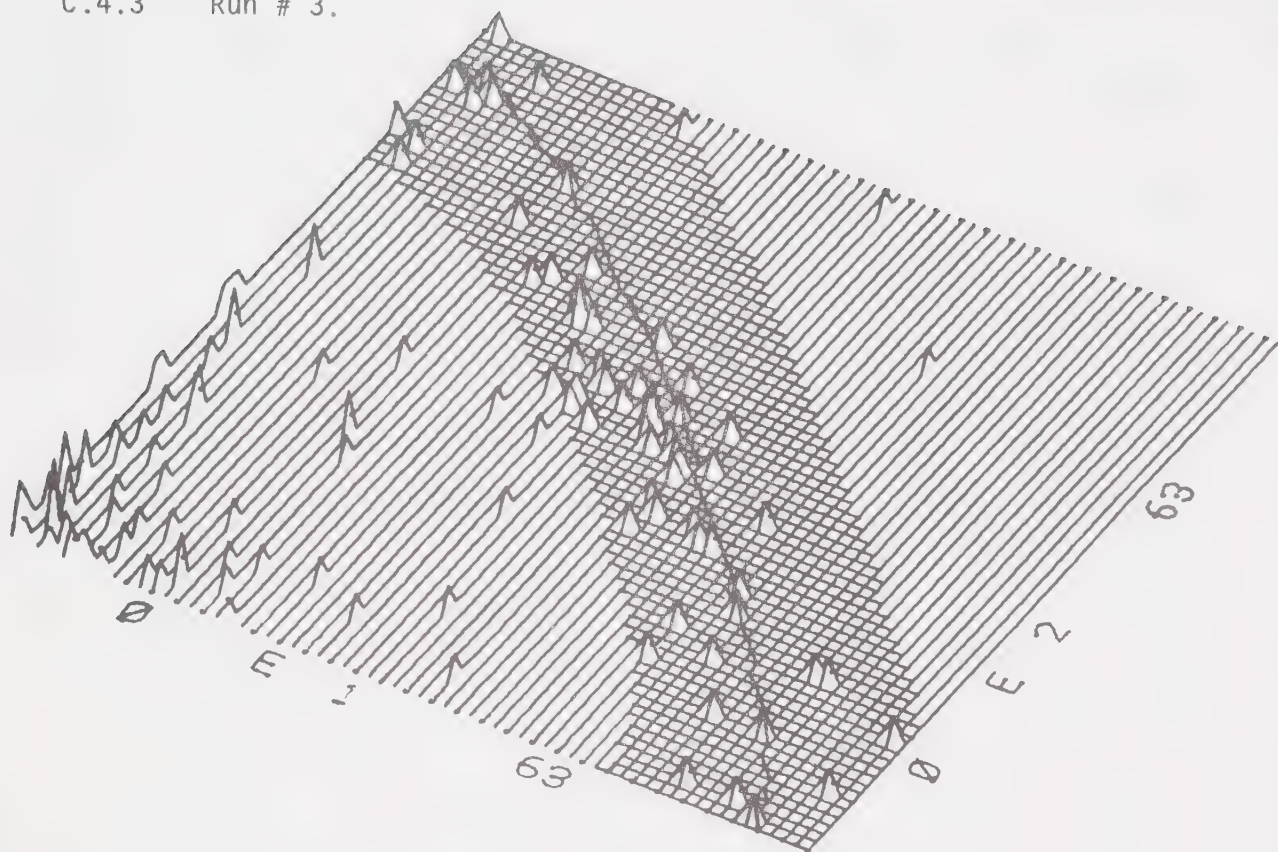


Figure C.4.3.1  $E_2 \times E_1$  isometric plot of "TRUE" events in  $30.0^\circ$ ,  $-30.0^\circ$  q.f.s. Run #3.



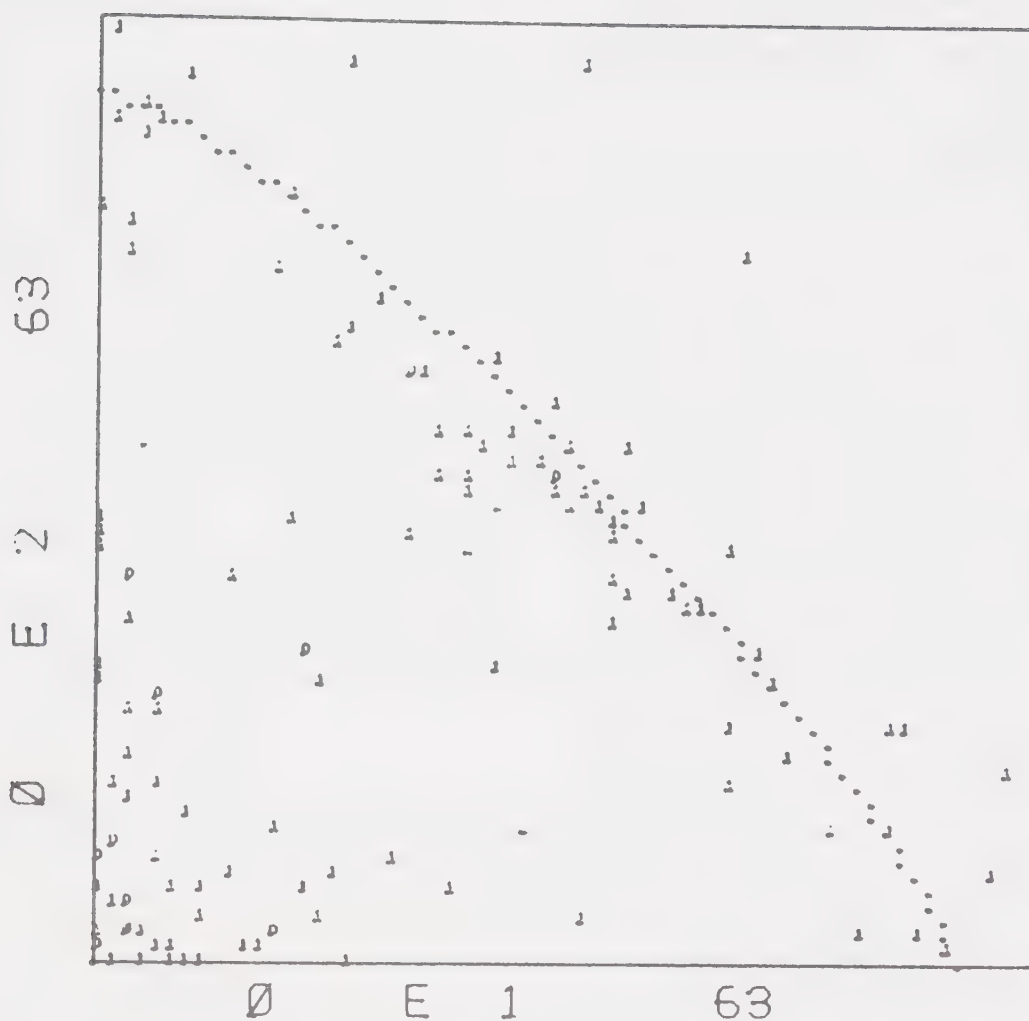


Figure C.4.3.2 E2 x E1 scatter plot of "TRUE" events in 30.0°, -30.0° q.f.s. Run #3.





## C.5 PROJECTION OF THE TWO-DIMENSIONAL DATA AND CALCULATION OF THE ABSOLUTE CROSS SECTION

### C.5.1 Data Projection

The spectra of the "TRUE" events projected onto the neutron energy axes from the band around the kinematical locus were formed automatically during the playback analysis of data events from the magnetic tape.

One could, in addition, project the data within the band onto a  $45^\circ$  line, tangent to the locus curve at the QFS peak position, after the two-dimensional data histograms had been formed. The program GOLDPAN further allowed binning of the projected spectra channels into variable width (1 MeV in our case) bins together with their display and their print-out.

### C.5.2 The Differential Cross Section

The differential cross section  $\frac{d^5\sigma_B}{dE d\Omega_1 d\Omega_2}$  for the  $d(n,2n)p$  breakup reaction is related to the intensity distribution  $I(s, \Omega_1, \Omega_2)$  by the target thickness  $N_t(\text{cm}^{-2})$  and the number of projectiles  $N_p$

$$I(s, \Omega_1, \Omega_2) = N_t N_p \int_{\Delta E_1} \int_{\Delta \Omega_1} \int_{\Delta \Omega_2} \frac{d^5\sigma_B}{dE_1 d\Omega_1 d\Omega_2} dE_1 d\Omega_1 d\Omega_2 \quad (C-1)$$

The integration is to be extended over a neutron energy interval  $\Delta E_1 (E_2 = E_2(E_1))$  along the kinematical locus) and



the experimental solid angles  $\Delta\Omega_1, \Delta\Omega_2$ .

Thus the number of experimental counts  $n_B$  in the five-variable space interval  $\Delta E_1 \Delta\Omega_1 \Delta\Omega_2$  obtained in a run of duration  $t$  will be

$$n_B(E_1, \Omega_1, \Omega_2) = N_t N_p t \int_{\Delta E_1} \int_{\Delta\Omega_1} \int_{\Delta\Omega_2} \frac{d^5\sigma_B}{dE_1 d\Omega_1 d\Omega_2} \eta_1(E_1) \eta_2(E_2(E_1)) dE_1 d\Omega_1 d\Omega_2 \quad (C-2)$$

where  $\eta_1(E), \eta_2(E)$  are the neutron detector #1 and #2 efficiencies for a neutron of energy  $E$ . We assume the efficiency of the C6D6 detector for a charged particle recoil is 1.0 (not so in run #1 - see corrections).

Similarly, the number  $N_1'$  of monitor counts, obtained in neutron detector 1 as singles due to the n-d elastic scattering of differential cross section  $\frac{d\sigma_e(\Omega)}{d\Omega}$ , over the same time  $t$  is

$$N_1' = N_t N_p t \int_{\Delta\Omega_1} \frac{d\sigma_e(\Omega)}{d\Omega} \eta_1(E(\Omega)) d\Omega \quad (C-3)$$

This equation is valid for both neutron detectors ( $N_1, N_2$ ).

Replacing now,  $\frac{d^5\sigma_B}{dE d\Omega_1 d\Omega_2}$ ,  $\eta_1(E), \eta_2(E)$  by step-constant values  $\sigma_{B_i}, \eta_{1_i}, \eta_{2_i}$  obtained by averaging these variables over intervals  $\Delta\Omega_1 \times \Delta\Omega_2 \times \Delta E_i$ , where  $\Delta E_i$  is an interval around  $E_1 = E_i$ , in equation (C-2), the number of counts  $n_{B_i}$  in such energy interval  $\Delta E_i$  becomes



$$n_{B_i} = N_t N_p t \sigma_{B_i} \eta_{1_i} \eta_{2_i} \Delta\Omega_1 \Delta\Omega_2 \Delta E_i \quad (C-4)$$

Similarly, the number of monitor counts  $N_1$  obtained when  $\frac{d\sigma_e(\Omega_1)}{d\Omega_1}$  and  $\eta_1(E(\Omega))$  in equation (C-3) are replaced by their averaged values  $\sigma_{e_1}$ ,  $\eta_{e_1}$  over the solid angle  $\Delta\Omega_1$  is

$$N_1 = N_t N_p t \sigma_{e_1} \eta_{e_1} \Delta\Omega_1 \quad (C-5)$$

substituting for  $N_t N_p t \Delta\Omega_1$  from equation (C-5), into (C-4) we can express the average cross section in a  $\Delta E_i = 1$  MeV bin around the neutron energy  $E_i$  by rewriting equation (C-4) as

$$\sigma_{B_i} = n_{B_i} \frac{\sigma_{e_1}}{N_1 \Delta\Omega_2} \frac{\eta_{e_1}}{\eta_{1_i}} \frac{\eta_{e_2}}{\eta_{2_i}} \frac{1}{\eta_{e_2}} \quad (C-6)$$

The energy binning of  $\Delta E_i = 1$  MeV seemed to be a reasonable compromise between the variation of the differential cross section, and finite geometry broadening on one side and the statistical error on the other.

### C.5.3 Monitor Peak Summing

The individual monitor spectra files in each run at one geometry setting were added together lining up the calculated centroids of the n-d elastic scattering peak into the same channel. Two such summed monitor spectra corresponding to the left and the right neutron detectors were



obtained in each run (#1,#2,#3) as displayed in Fig. C.5.3.1. These were further analyzed using the GOLDPAN routine which produced the net number of counts in the peak. The monitor peaks in runs #1 and #3 were free of any n-C elastic scattering contribution for all practical purposes. This contribution was eliminated by the  $1/4 \text{ } ^{137}_{\text{Cs}}$  C6D6 detector bias of the duplicated monitor circuit in run #1 and by the combination of too small a carbon recoil energy and  $1/3 \text{ } ^{241}_{\text{Am}}$  C6D6 bias in run #2.

A 23% n-C elastic contribution was observed in run #3. The superposition of the two peaks was reconstructed geometrically (see inset in Fig. C.5.3.1) on a large scale computer plot and the percentage of the total peak area corresponding to the n-d elastic scattering peak alone determined. Only one monitor sum is necessary in each run but the calculations were performed for both monitors to check the consistency of the results. The numbers of counts from the two monitors in each of the symmetric geometry runs were equal to within a few percent and the average value was used in the calculation of the cross section.

The monitor spectra were taken with respect to one C6D6 detector only in each run (C6D6 #1 in run #2 and C6D6 #2 - center in runs #2 and #3). The other two sets of data in each run were normalized to the monitor C6D6 data set by the ratio of the n-d elastic peak sums in the three singles TOF spectra





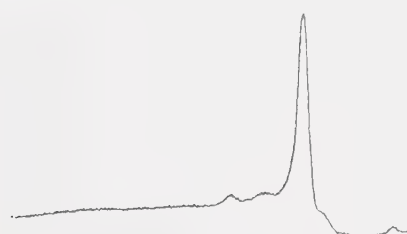


Figure C.5.3.1 The left and right monitor spectra corresponding to the entire Runs #1, #2, and #3. The inset is showing the contribution of n-C elastic scattering into the n-D elastic monitor peak and the reconstruction of their superposition.

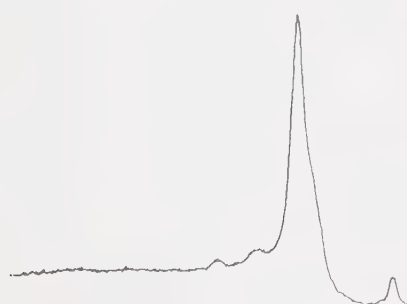
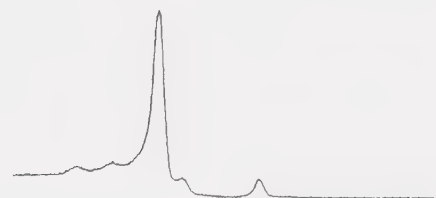


RUN # 1

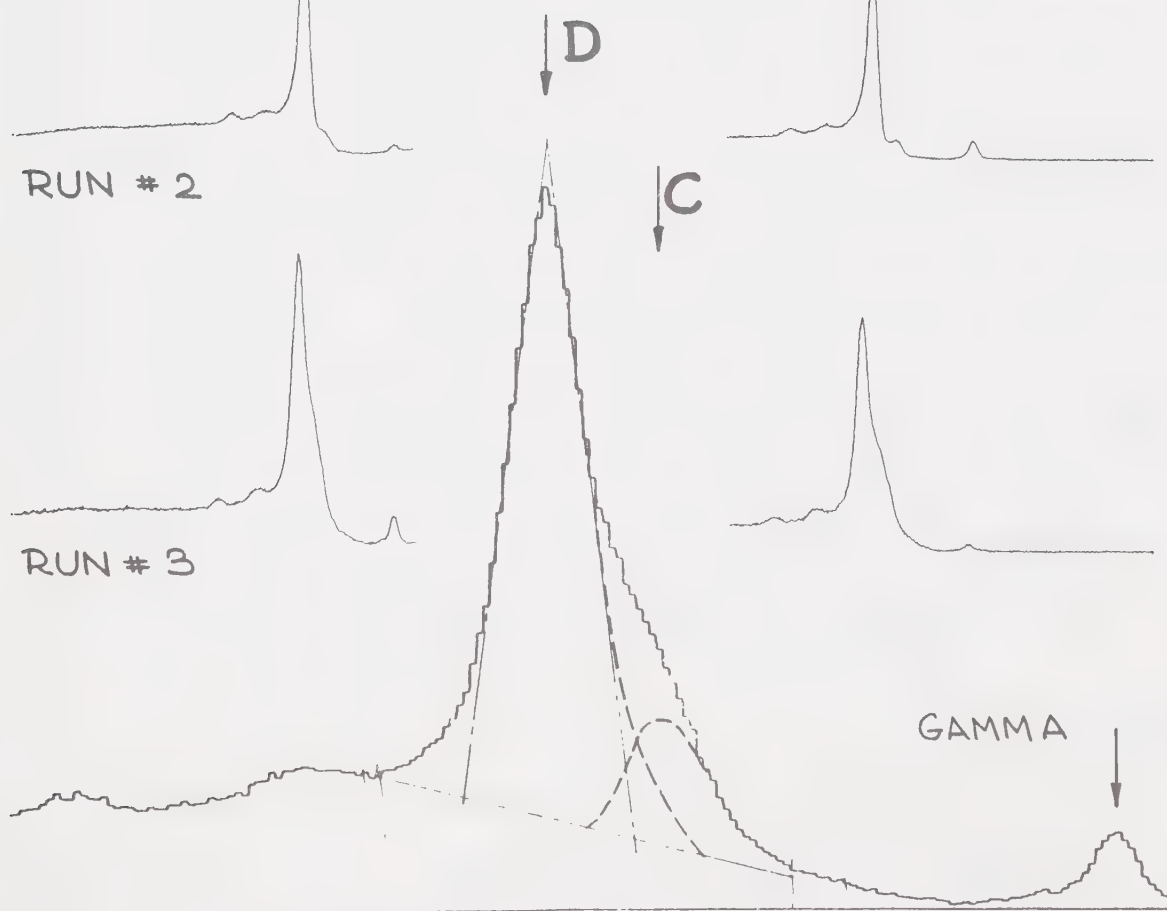
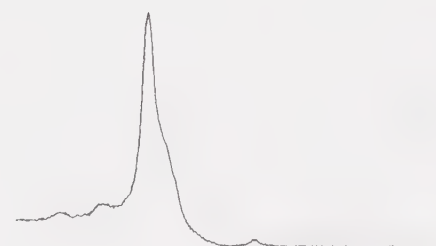
MONITOR B



RUN # 2



RUN # 3





obtained simultaneously in periodic intervals throughout each run.

#### C.5.4 Neutron Detector Efficiency

The neutron detector efficiency curves applied in the calculation of the absolute cross section, for the two neutron detector bias settings of  $1 \times {}^{60}\text{Co}$  and  $0.3 \times {}^{137}\text{Cs}$  used in this work, are shown in Fig. C.5.4.1.

As no experimentally measured efficiency was yet available for the neutron detectors used in this experiment, experimentally measured and fitted efficiency curves of Droszg (Dr-72) were used and checked by a Monte Carlo simulation program (Gr-67). The Droszg data were obtained for the same NE213 detector thickness with the other dimensions similar to our detectors. The calculated efficiency curve agreed to within  $\sim 5\%$  with the Droszg data up to the neutron energies where n-Carbon interactions start contributing into the light pulse produced in the scintillator. The computer program used does not contain the n-C cross sections. The upper part of the efficiency curve was therefore extrapolated to the  $0.3 \times {}^{137}\text{Cs}$  efficiency curve using the Droszg data.

A qualitative illustration of the n-Carbon contribution difference between the two different bias efficiency curves (Fig. C.5.4.1) can be seen in Figs. C.1.1 and C.1.2 as the extension of the neutron pulse shape ridge to the left at the low energy in Fig. C.1.2. The diagonal background



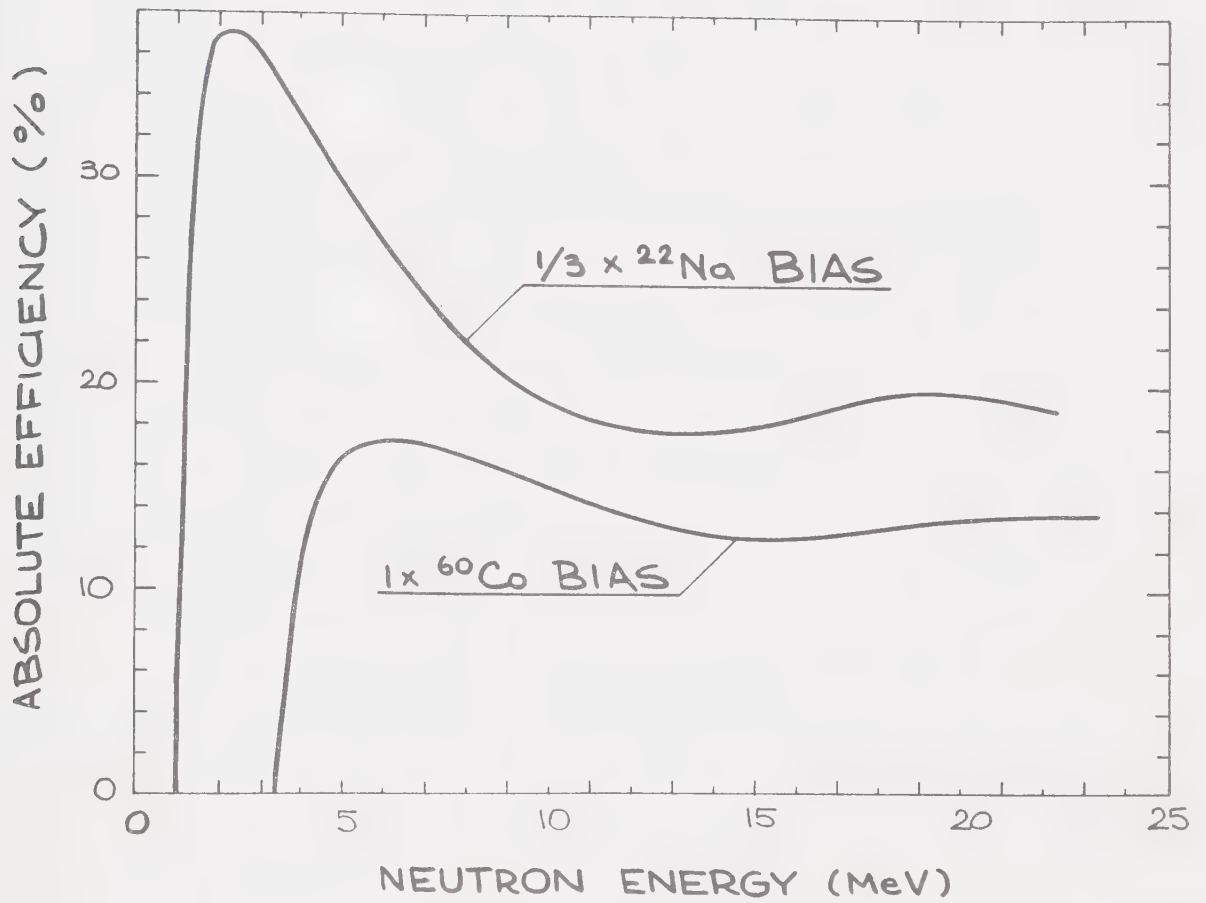


Figure C.5.4.1 The neutron detector efficiency curves used in this work.





band (e.g., in Figs. C.3.2.3, C.3.2.4), discussed in Chapter C.1.1, can be caused solely by the n-Carbon inelastic interactions in the neutron detector, because n-p interactions in the scintillator can not produce the  $\gamma$ -ray involved in this type of background. Thus the diagonal band is further evidence for the importance of n-C interactions in a scintillator at the lower bias.

#### C.5.5 Calculations and Results

The n-d elastic scattering data of Segrave et al. (Se-72) were used for the n-d elastic differential cross section. The values obtained at 20.5 MeV and 23 MeV incident neutron energy were averaged to be used as the differential cross section at 21.5 MeV in this calculation since no practical difference between the two values appears within their error ranges.

All data presented as tables and graphs in this chapter were corrected for a dead time of about 10% caused by the anticoincidence rejection of two simultaneous events occurring in two different C6D6 detectors.



TABLE 2 ABSOLUTE DIFFERENTIAL CROSS SECTION IN RUN #1

$\phi_1 = \phi_2 = 35^\circ$  ;  $\phi_1 = 0^\circ$ ,  $\phi_2 = 180^\circ$

$E_{n_0} = 21.5$ MeV	$E_{p_{min}} = .173$ MeV	At $E_1 = 9.55$ MeV	$E_{e_1} = E_{e_2} = 17.8$ MeV
$\eta_{e_1} = \eta_{e_2} = 0.133$	$\sigma_e = 62$ mb	$N_{MON} = 4.084 \times 10^5$	$\Omega_1 = .021$ sr
Dead time correction $d = 1.1$			

$$\sigma_{B_i} = \frac{\sigma_e d}{N_{MON} \eta_{e_1} \eta_{e_2}} \frac{\eta_{e_1}}{\eta_{1_i}} \frac{\eta_{e_2}}{\eta_{2_i}} \frac{1}{\eta_{C6D6_i}} n_{B_i} = \frac{c_i}{\eta_{C6D6_i}} n_i$$

Average energy $\frac{E_{1_i}}{\eta_{1_i}}$ (MeV)	Average energy $\frac{E_{2_i}}{\eta_{2_i}}$ (MeV)	$n_{2_i}$	$C_i$ ( $\frac{mb}{sr^2 MeV}$ )	No. of counts $n_{B_i}$	$\sqrt{n_{B_i}}$ $\frac{1}{n_{B_i}}$	C6D6 BIAS CORRECTION $\frac{1}{\eta_{C6D6_i}}$	$\sigma_{B_i}$ ( $\frac{mb}{sr^2 MeV}$ )	$\eta_{B_i}$ ( $\frac{mb}{sr^2 MeV}$ )
3.75	14.5	.127	.058	8	35	1.0	.51	.18
4.75	13.8	.129	.048	8	35	1.0	.42	.15
5.75	13.0	.132	.043	8	35	1.03	.39	.14
6.75	12.2	.135	.043	11	30	1.16	.60	.18
7.75	11.3	.141	.042	12	29	1.43	.80	.23
8.75	10.3	.147	.042	19	23	1.77	1.56	.36
9.75	9.3	.155	.042	24	20	2.02	2.24	.46
10.75	8.3	.163	.042	21	22	1.77	1.72	.38
11.75	7.2	.169	.042	17	24	1.44	1.14	.28
12.75	5.8	.172	.043	9	33	1.17	.50	.17
13.75	4.6	.164	.047	6	41	1.03	.32	.13





Figure C.5.5.1 Comparison of experimental and theoretical differential cross sections for the reaction  $n_0 + d \rightarrow n_1 + n_2 + p$  in the projection onto  $E_{n_1}$  axis in Run #1. The dashed line indicates the proton energy (right scale).

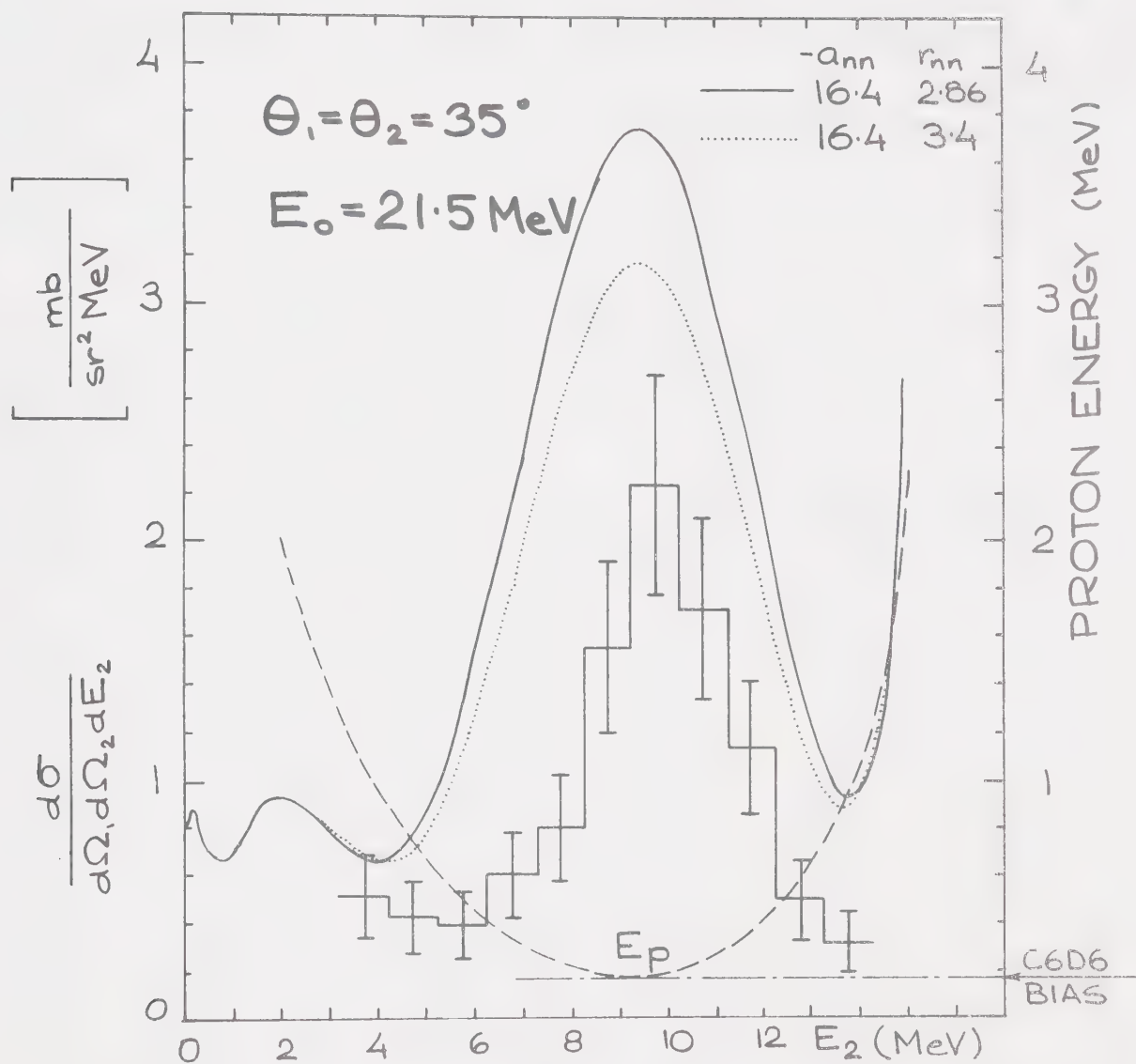






TABLE 3 ABSOLUTE DIFFERENTIAL CROSS SECTION

IN RUN #2 ;  $\theta_1 = \theta_2 = 23.8^\circ$  ;  $\phi_1 = 0$ ,  $\phi_2 = 180^\circ$ 

$E_{n_0} = 21.5^\circ \text{MeV}$	$E_{p_{\min}} = .829 \text{MeV}$	at $E_1 = 9.26 \text{MeV}$
$E_{e_1} = E_{e_2} = 19.8 \text{MeV}$	$\eta_{e_1} = \eta_{e_2} = .199$	$\sigma_e = 100 \text{ mb/sr}$
$N_{\text{MON}} = 3.4 \times 10^5$	C6D62/C6D61 neutron flux ratio $f = 0.56$	
$\Omega_2 = 7.3 \times 10^{-3}$	Dead time correction $d = 1.1$	

$$\sigma_{B_i} = \frac{\sigma_e d}{N_{\text{MON}} \cdot f \cdot \Omega_2 \cdot \eta_{e_2}} \cdot \frac{\eta_{e_1}}{\eta_{1_i}} \cdot \frac{\eta_{e_2}}{\eta_{2_i}} \cdot n_{B_i} = c_i n_i$$

Average energy $\overline{E_{1_i}}$ (MeV)	$\eta_{1_i}$	Average energy $\overline{E_{2_i}}$ (MeV)	$\eta_{2_i}$	$c_i$	$n_{B_i}$	$\sqrt{n_{B_i}}$ $\frac{n_{B_i}}{(\%)}$	$\sigma_{B_i}$ $(\frac{\text{mb}}{\text{sr}^2 \text{MeV}})$	$\Delta \sigma$ $(\frac{\text{mb}}{\text{sr}^2 \text{MeV}})$
1.6	.336	16.4	.188	.078	1	100	.08	.08
2.7	.368	15.6	.184	.072	6	41	.43	.18
3.7	.336	14.6	.181	.081	5	45	.40	.18
4.8	.301	13.7	.179	.091	5	45	.46	.20
5.8	.271	12.7	.179	.101	10	32	1.01	.32
6.8	.244	11.7	.181	.111	13	28	1.44	.40
7.8	.222	10.7	.185	.119	8	35	.96	.34
8.8	.205	9.7	.194	.123	17	24	2.10	.51
9.8	.193	8.7	.206	.123	11	30	1.36	.41
10.8	.185	7.7	.223	.119	7	38	.83	.31
11.8	.181	6.7	.247	.110	4	50	.44	.22
12.8	.179	5.7	.275	.100	8	35	.80	.28
13.7	.179	4.7	.305	.09	3	58	.27	.16
14.7	.181	3.7	.338	.08	5	45	.40	.18
15.6	.184	2.7	.368	.07	4	50	.29	.14



TABLE 4 ABSOLUTE DIFFERENTIAL CROSS SECTION

IN RUN #2 ;  $\theta_1 = \theta_2 = 25.0^\circ$  ;  $\phi_1 = 0$ ,  $\phi_2 = 180^\circ$ 

$E_{n_0} = 21.5 \text{ MeV}$	$E_{p_{\min}} = .756 \text{ MeV}$	at $E_1 = 9.3 \text{ MeV}$
$E_{e_1} = E_{e_2} = 19.6 \text{ MeV}$	$\eta_{e_1} = \eta_{e_2} = .196$	$\sigma_e = 100 \text{ mb/sr}$
$N_{\text{MON}} = 3.4 \times 10^5$	C6D62/C6D61 neutron flux ratio $f = 1.0$	
$\Omega_2 = 7.3 \times 10^{-3}$	Dead time correction $d = 1.1$	

$$\sigma_{B_i} = \frac{\sigma_e d}{N_{\text{MON}} \cdot f \cdot \Omega_2 \cdot \eta_{e_2}} \cdot \frac{\eta_{e_1}}{\eta_{1_i}} \cdot \frac{\eta_{e_2}}{\eta_{2_i}} \cdot n_{B_i} = c_i n_i$$

Average energy $\overline{E_{1_i}}$ (MeV)	$\eta_{1_i}$	Average energy $\overline{E_{2_i}}$ (MeV)	$\eta_{2_i}$	$c_i$	$n_{B_i}$	$\sqrt{n_{B_i}}$ $\frac{n_{B_i}}{(\%)}$	$\sigma_{B_i}$ $(\frac{\text{mb}}{\text{sr}^2 \text{ MeV}})$	$\Delta\sigma$ $(\frac{\text{mb}}{\text{sr}^2 \text{ MeV}})$
1.6	.336	16.4	.187	.141	4	50	.56	.28
2.7	.368	15.5	.184	.131	6	41	.79	.32
3.7	.336	14.6	.181	.146	3	58	.44	.25
4.8	.301	13.7	.179	.164	3	58	.49	.29
5.8	.271	12.7	.171	.191	7	38	1.34	.51
6.8	.244	11.8	.181	.201	5	45	1.00	.45
7.8	.222	10.8	.185	.216	7	38	1.51	.57
8.8	.205	9.7	.194	.223	11	30	2.45	.74
9.8	.193	8.8	.205	.224	8	35	1.79	.63
10.8	.185	7.8	.221	.217	7	38	1.52	.57
11.8	.181	6.8	.246	.199	8	35	1.59	.56
12.8	.179	5.7	.273	.182	3	58	.54	.31
13.7	.179	4.7	.303	.164	2	71	.33	.23
14.7	.181	3.7	.338	.145	5	45	.73	.32
15.6	.184	2.6	.368	.131	6	41	.79	.32



TABLE 5 ABSOLUTE DIFFERENTIAL CROSS SECTION

IN RUN #2 ;  $\theta_1 = \theta_2 = 26.3^\circ$  ;  $\phi_1 = 0$ ,  $\phi_2 = 180^\circ$ 

$E_{n_0} = 21.5 \text{ MeV}$	$E_{p_{\min}} = .678 \text{ MeV}$	at $E_1 = 9.34 \text{ MeV}$
$E_{e_1} = E_{e_2} = 19.43 \text{ MeV}$	$\eta_{e_1} = \eta_{e_2} = .199$	$\sigma_e = 100 \text{ mb/sr}$
$N_{\text{MON}} = 3.4 \times 10^5$	C6D62/C6D61 neutron flux ratio $f = 1.4$	
$\Omega_2 = 7.3 \times 10^{-3}$	Dead time correction $d = 1.1$	

$$\sigma_{B_i} = \frac{\sigma_e d}{N_{\text{MON}} \cdot f \cdot \Omega_2 \cdot \eta_{e_2}} \cdot \frac{\eta_{e_1}}{\eta_{1_i}} \cdot \frac{\eta_{e_2}}{\eta_{2_i}} \cdot n_{B_i} = c_i n_i$$

Average energy $\overline{E_{1_i}}$ (MeV)	$\eta_{1_i}$	Average energy $\overline{E_{2_i}}$ (MeV)	$\eta_{2_i}$	$c_i$	$n_{B_i}$	$\sqrt{n_{B_i}}$ $\overline{n_{B_i}}$ (%)	$\sigma_{B_i}$ ( $\frac{\text{mb}}{\text{sr}^2 \text{ MeV}}$ )	$\Delta\sigma$ ( $\frac{\text{mb}}{\text{sr}^2 \text{ MeV}}$ )
1.6	.336	16.2	.187	.195	1	100	.20	.20
2.7	.368	15.5	.183	.182	4	50	.73	.36
3.7	.336	14.7	.181	.202	0	-	-	-
4.8	.301	13.7	.179	.228	4	50	.90	.46
5.8	.271	12.8	.179	.253	8	35	2.01	.71
6.8	.244	11.9	.181	.278	4	50	1.10	.56
7.8	.222	10.9	.184	.299	7	38	2.09	.79
8.8	.205	9.9	.192	.311	3	58	.93	.54
9.8	.193	8.9	.204	.310	4	50	1.24	.62
10.8	.185	7.9	.220	.301	7	38	2.11	.80
11.8	.181	6.9	.242	.279	5	45	1.40	.62
12.8	.179	5.8	.27	.254	2	71	.51	.36
13.7	.179	4.8	.303	.226	1	100	.23	.23
14.7	.181	3.6	.339	.200	3	58	.60	.35
15.6	.184	2.4	.37	.180	5	45	.90	.40





Figure C.5.5.2 Comparison of experimental and theoretical differential cross sections (solid line) for the reaction  $n_0 + d \rightarrow n_1 + n_2 + p$  in projection onto the kinematical locus length  $S$  for the three angle pairs of Run #2.



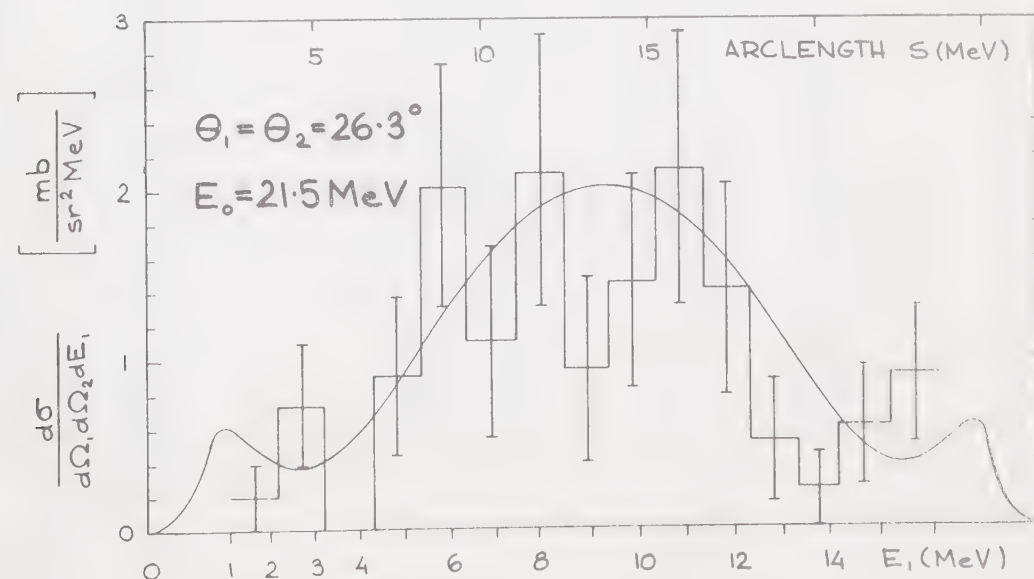
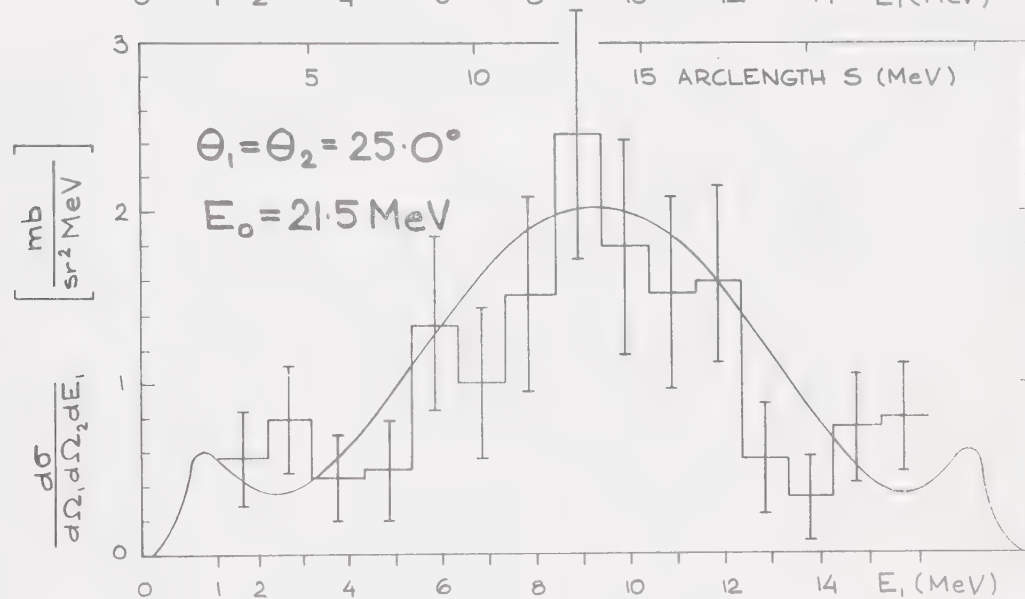
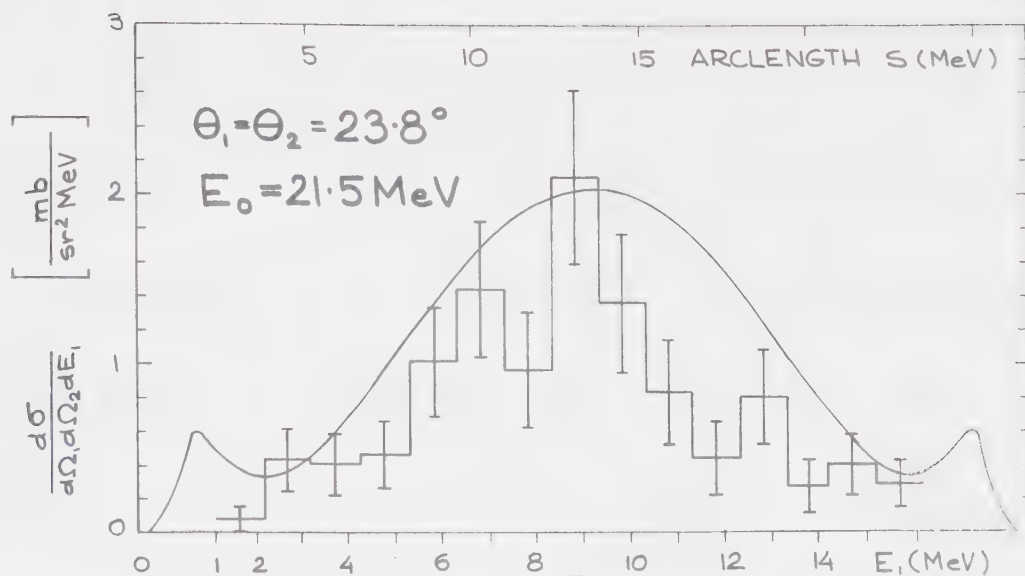




TABLE 6 ABSOLUTE DIFFERENTIAL CROSS SECTION  
IN RUN #3 ;  $\theta_1 = \theta_2 = 28.7^\circ$  ;  $\phi_1 = 0$ ,  $\phi_2 = 180^\circ$

$E_{n_0} = 21.5 \text{ MeV}$	$E_{p_{\min}} = .528 \text{ MeV}$	at $E_1 = 9.46 \text{ MeV}$
$E_{e_1} = E_{e_2} = 19.1 \text{ MeV}$	$\eta_{e_1} = \eta_{e_2} = .199$	$\sigma_e = 82.2 \text{ mb/sr}$
$N_{\text{MON}} = 2.979 \times 10^5$	C6D62/C6D61 neutron flux ratio $f = .40$	
$\Omega_2 = 6.65 \times 10^{-3}$	Dead time correction $d = 1.1$	

$$\sigma_{B_i} = \frac{\sigma_e d}{N_{\text{MON}} \cdot f \cdot \Omega_2 \cdot \eta_{e_2}} \cdot \frac{\eta_{e_1}}{\eta_{1_i}} \cdot \frac{\eta_{e_2}}{\eta_{2_i}} \cdot n_{B_i} = c_i n_i$$

Average energy $\overline{E_{1_i}}$ (MeV)	$\eta_{1_i}$	Average energy $\overline{E_{2_i}}$ (MeV)	$\eta_{2_i}$	$c_i$	$n_{B_i}$	$\sqrt{n_{B_i}}$ $\overline{n_{B_i}}$ (%)	$\sigma_{B_i}$ $(\frac{\text{mb}}{\text{sr}^2 \text{ MeV}})$	$\Delta\sigma$ $(\frac{\text{mb}}{\text{sr}^2 \text{ MeV}})$
1.6	.334	16.0	.186	.053	4	50	.23	.12
2.7	.368	15.4	.183	.053	4	50	.21	.11
3.8	.332	14.6	.181	.159	6	41	.35	.14
4.9	.298	13.7	.179	.067	2	71	.13	.10
5.9	.267	12.8	.179	.075	8	35	.60	.21
7.0	.240	17.8	.181	.083	4	50	.33	.17
8.0	.219	10.8	.185	.089	7	38	.62	.23
9.0	.202	9.8	.193	.092	7	38	.64	.24
10.0	.191	8.8	.205	.092	8	35	.73	.26
11.0	.184	7.8	.223	.087	6	41	.52	.21
12.0	.181	6.7	.246	.081	5	45	.40	.18
12.9	.179	5.7	.273	.073	5	45	.37	.16
13.8	.179	4.7	.303	.066	3	58	.20	.11
14.7	.181	3.6	.339	.059	4	50	.23	.12
15.5	.184	2.6	.370	.052	6	41	.32	.13



TABLE 7 ABSOLUTE DIFFERENTIAL CROSS SECTION

IN RUN #3 ;  $\theta_1 = \theta_2 = 30.0^\circ$  ;  $\phi_1 = 0$ ,  $\phi_2 = 180^\circ$ 

$E_{n_0} = 21.5 \text{ MeV}$	$E_{p_{\min}} = .445 \text{ MeV}$	at $E_1 = 9.45 \text{ MeV}$
$E_{e_1} = E_{e_2} = 18.8 \text{ MeV}$	$\eta_{e_1} = \eta_{e_2} = .199$	$\sigma_e = 82.2 \text{ mb/sr}$
$N_{\text{MON}} = 2.979 \times 10^5$	C6D62/C6D61 neutron flux ratio $f = 1.0$	
$\Omega_2 = 6.65 \times 10^{-3}$	Dead time correction $d = 1.1$	

$$\sigma_{B_i} = \frac{\sigma_e \cdot d}{N_{\text{MON}} \cdot f \cdot \Omega_2 \cdot \eta_{e_2}} \cdot \frac{\eta_{e_1}}{\eta_{1_i}} \cdot \frac{\eta_{e_2}}{\eta_{2_i}} \cdot n_{B_i} = c_i \cdot n_i$$

Average energy $\overline{E_{1_i}}$ (MeV)	$\eta_{1_i}$	Average energy $\overline{E_{2_i}}$ (MeV)	$\eta_{2_i}$	$c_i$	$n_{B_i}$	$\sqrt{n_{B_i}}$ $\overline{n_{B_i}}$ (%)	$\sigma_{B_i}$ $(\frac{\text{mb}}{\text{sr}^2 \text{ MeV}})$	$\Delta \sigma$ $(\frac{\text{mb}}{\text{sr}^2 \text{ MeV}})$
1.6	.334	15.9	.185	.145	3	58	.44	.25
2.7	.368	15.3	.183	.133	6	41	.80	.33
3.8	.332	14.5	.181	.149	3	58	.45	.26
4.9	.298	13.6	.179	.168	1	100	.17	.17
5.9	.267	12.8	.179	.188	4	50	.75	.38
7.0	.240	11.8	.181	.207	4	50	.83	.41
8.0	.219	10.9	.185	.221	12	29	2.66	.77
9.0	.202	9.9	.192	.231	7	38	1.62	.61
10.0	.191	8.9	.204	.230	9	33	2.07	.69
11.0	.184	7.9	.221	.220	2	71	.44	.31
12.0	.181	6.8	.244	.203	4	50	.81	.41
12.9	.179	5.8	.272	.184	3	58	.55	.32
13.8	.179	4.7	.303	.165	6	41	.99	.41
14.7	.181	3.8	.335	.148	4	50	.59	.30
15.5	.184	2.5	.370	.132	5	45	.66	.29



TABLE 8 ABSOLUTE DIFFERENTIAL CROSS SECTION  
IN RUN #3 ;  $\theta_1 = \theta_2 = 31.4^\circ$  ;  $\phi_1 = 0$ ,  $\phi_2 = 180^\circ$

$E_{n_0} = 21.5 \text{ MeV}$	$E_{p_{\min}} = .362 \text{ MeV}$	at $E_1 = 9.5 \text{ MeV}$
$E_{e_1} = E_{e_2} = 18.58 \text{ MeV}$	$\eta_{e_1} = \eta_{e_2} = .198$	$\sigma_e = 62.2 \text{ mb/sr}$
$N_{\text{MON}} = 2.979 \times 10^5$	C6D62/C6D61 neutron flux ratio $f = 1.26$	
$\Omega_2 = 6.65 \times 10^{-4}$	Dead time correction $d = 1.1$	

$$\sigma_{B_i} = \frac{\sigma_e \cdot d}{N_{\text{MON}} \cdot f \cdot \Omega_2 \cdot \eta_{e_2}} \cdot \frac{\eta_{e_1}}{\eta_{1_i}} \cdot \frac{\eta_{e_2}}{\eta_{2_i}} \cdot n_{B_i} = c_i \cdot n_i$$

Average energy $\overline{E_{1_i}}$ (MeV)	$\eta_{1_i}$	Average energy $\overline{E_{2_i}}$ (MeV)	$\eta_{2_i}$	$c_i$	$n_{B_i}$	$\sqrt{n_{B_i}}$ $\overline{n_{B_i}}$ (%)	$\sigma_{B_i}$ $(\frac{\text{mb}}{\text{sr}^2 \text{ MeV}})$	$\Delta \sigma$ $(\frac{\text{mb}}{\text{sr}^2 \text{ MeV}})$
1.6	.334	15.7	.185	.183	2	71	.37	.26
2.7	.368	15.2	.183	.167	6	41	1.00	.41
3.8	.332	14.5	.181	.187	2	71	.37	.26
4.9	.298	13.7	.179	.211	2	71	.42	.30
5.9	.267	12.8	.179	.235	3	58	.71	.41
7.0	.240	11.9	.181	.260	3	58	.78	.45
8.0	.219	11.0	.185	.278	7	38	1.94	.73
9.0	.202	10.0	.191	.292	10	32	2.92	.92
10.0	.191	9.0	.203	.290	7	38	2.03	.77
11.0	.184	8.0	.219	.279	6	41	1.68	.68
12.0	.181	6.9	.243	.256	2	71	.51	.36
12.9	.179	5.9	.268	.235	3	58	.70	.41
13.8	.179	4.8	.303	.207	3	58	.62	.36
14.7	.181	3.6	.341	.182	2	71	.36	.26
15.5	.184	2.3	.370	.165	4	50	.66	.33







Figure C.5.5.3 Comparison of experimental and theoretical differential cross sections (solid line) for the reaction  $n_0 + d \rightarrow n_1 + n_2 + p$  in projection onto the kinematical locus length  $S$  for the three angle pairs of Run #3.

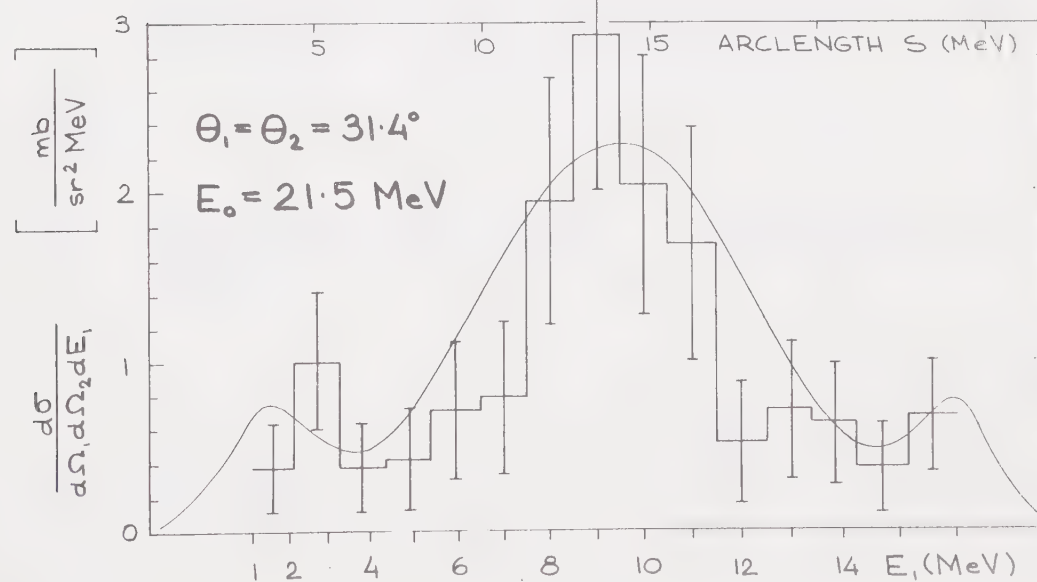
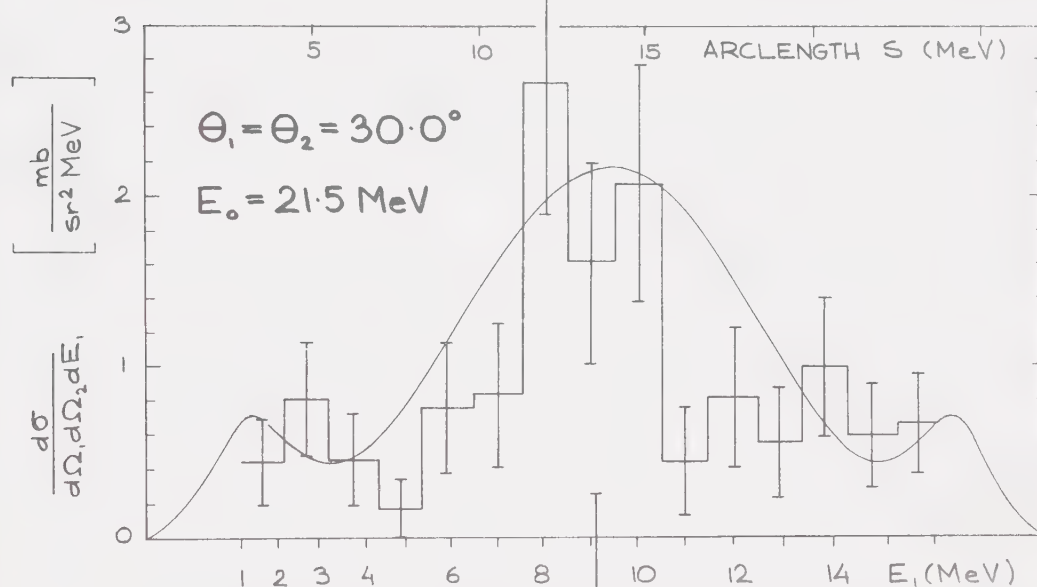
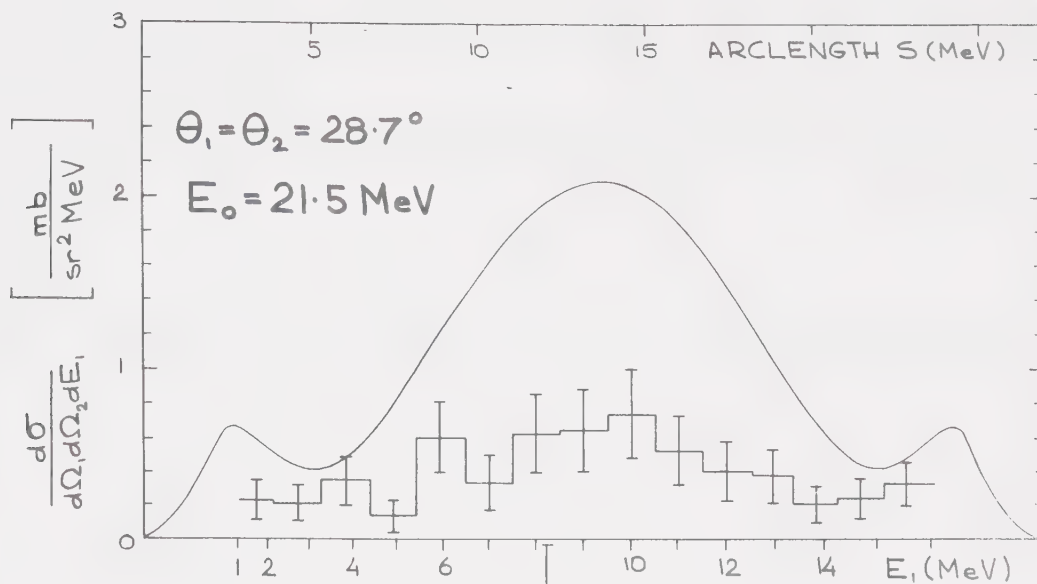




TABLE 9 RUN #2 CROSS SECTION AVERAGED AROUND 25.0°, -25.0° GEOMETRY

$\overline{E}_i$ (MeV)	$\sigma_i^{23.8^\circ}$ $(\frac{\text{mb}}{\text{sr}^2 \text{MeV}})$	$\sigma_i^{25.0^\circ}$ $(\frac{\text{mb}}{\text{sr}^2 \text{MeV}})$	$\sigma_i^{26.3^\circ}$ $(\frac{\text{mb}}{\text{sr}^2 \text{MeV}})$	Average $\sigma_i^{25.0^\circ}$ $(\frac{\text{mb}}{\text{sr}^2 \text{MeV}})$	Total no. of counts $n_{B_i}$	$\frac{\sqrt{n_{B_i}}}{n_{B_i}}$ (%)	Average $\Delta \sigma_i^{25.0^\circ}$ $(\frac{\text{mb}}{\text{sr}^2 \text{MeV}})$
1.6	.08	.56	.20	.28	6	41	.11
2.7	.43	.79	.73	.65	6	25	.16
3.7	.40	.44	Ø	.28	8	35	.10
4.8	.46	.49	.90	.62	12	29	.18
5.8	1.01	1.34	2.01	1.45	25	20	.29
6.8	1.44	1.00	1.10	1.18	22	21	.25
7.8	.96	1.51	2.09	1.52	22	21	.32
8.8	2.10	2.45	.93	1.83	31	18	.33
9.8	1.36	1.79	1.24	1.46	23	21	.30
10.8	.83	1.52	2.11	1.49	21	22	.33
11.8	.44	1.59	1.40	1.14	17	24	.28
12.8	.80	.54	.51	.62	13	28	.17
13.7	.27	.33	.23	.28	6	41	.11
14.7	.40	.73	.60	.58	13	28	.16
15.6	.29	.79	.90	.66	15	26	.17





Figure C.5.5.4 Comparison of relevant energies and both experimental and theoretical differential cross sections for the reaction  $n_0 + d \rightarrow n_1 + n_2 + p$  at  $E_0 = 21.5$  MeV with  $\phi_1 = 0^\circ$ ,  $\phi_2 = 180^\circ$ ,  $\theta_1 = \theta_2 = 25^\circ$ .

(Upper) Absolute experimental data (step line) and theoretical curves.

(Lower) Relative energies  $E_{n_1 p}$ ,  $E_{n_2 p}$ ,  $E_{n_1 n_2}$  for f.s.i., proton energy  $E_p$  and the production angle  $\theta_{n_1 n_2 \text{ c.m.}}$  (dashed line, right scale).



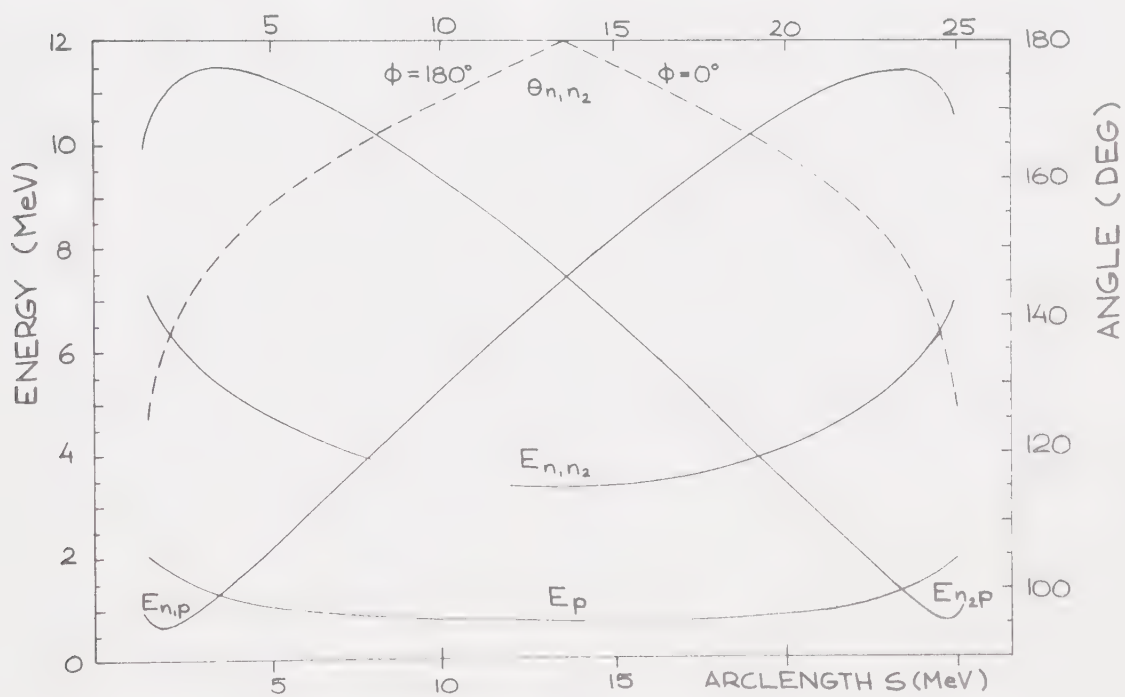
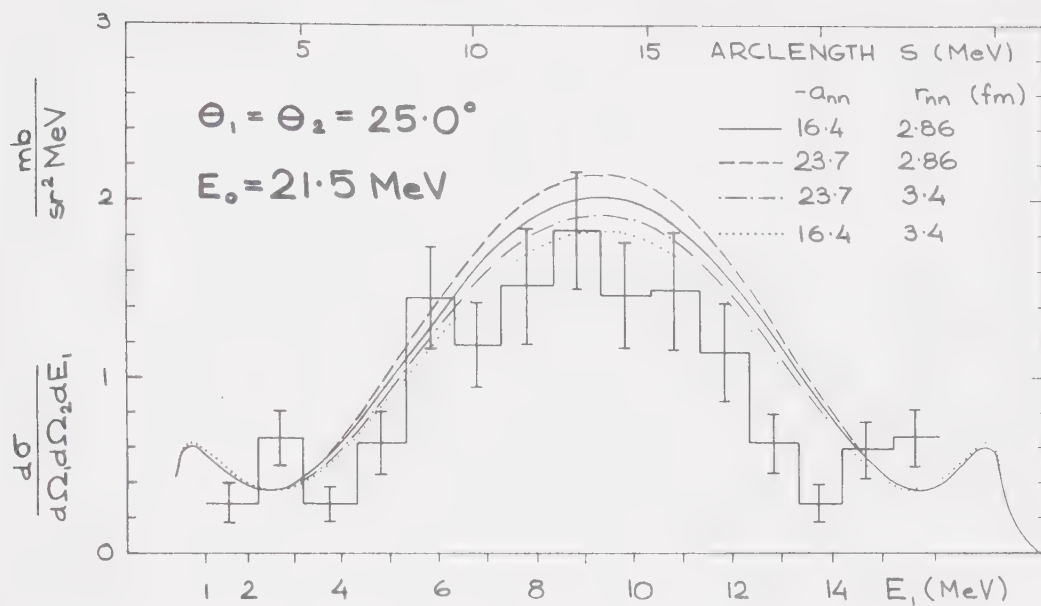




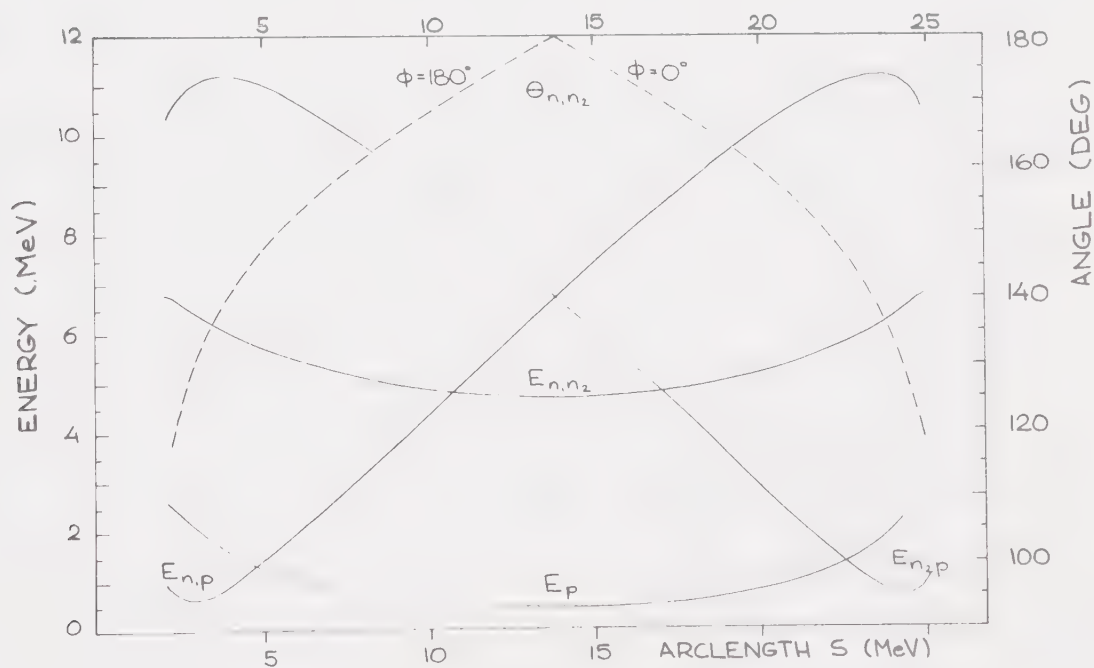
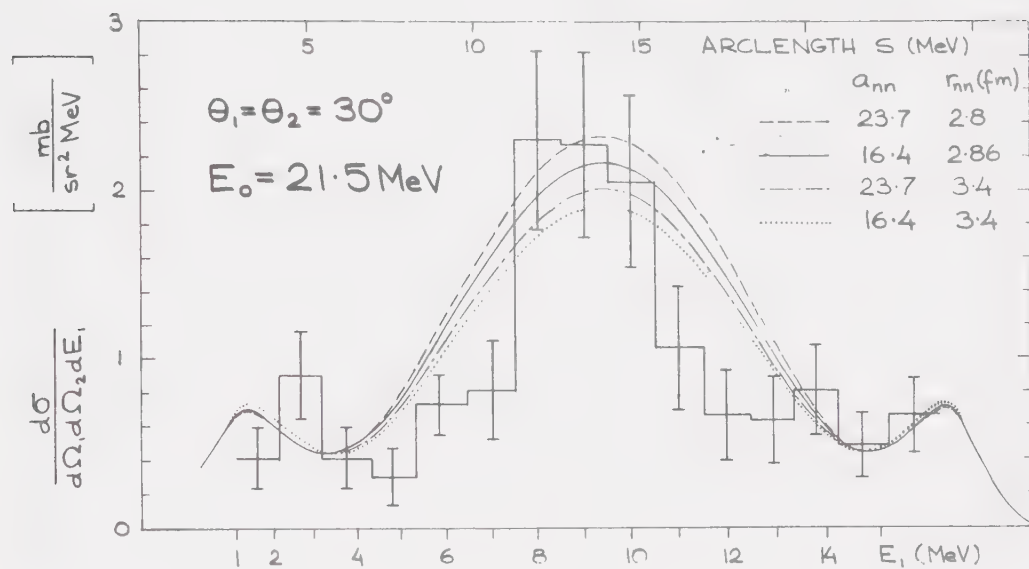
TABLE 10 RUN #3 CROSS SECTION AVERAGED AROUND  
30.0°, -30.0° GEOMETRY

$\overline{E}_i$ (MeV)	$\sigma_{30.0^\circ}$ $(\frac{\text{mb}}{\text{sr}^2 \text{MeV}})$	$\sigma_{31.4^\circ}$ $(\frac{\text{mb}}{\text{sr}^2 \text{MeV}})$	average $\overline{\sigma}_{30.0^\circ}$ $(\frac{\text{mb}}{\text{sr}^2 \text{MeV}})$	Total no. of counts $n_{B_i}$	$\frac{\sqrt{n_{B_i}}}{n_{B_i}}$ (%)	$\overline{\Delta\sigma}_{30.0^\circ}$ $(\frac{\text{mb}}{\text{sr}^2 \text{MeV}})$
1.56	.44	.37	.41	5	45	.18
2.69	.80	1.00	.90	12	29	.26
3.81	.45	.37	.41	5	45	.18
4.88	.17	.42	.30	3	58	.17
5.94	.75	.71	.73	7	38	.28
7.0	.83	.78	.81	7	38	.30
8.0	2.66	1.94	2.3	19	23	.53
9.0	1.62	2.92	2.27	17	24	.55
10.0	2.07	2.03	2.05	16	25	.51
11.0	.44	1.68	1.06	8	35	.37
12.0	.81	.51	.66	6	41	.27
12.94	.55	.70	.63	6	41	.26
13.81	.99	.62	.81	9	33	.27
14.69	.59	.36	.48	6	41	.19
15.46	.66	.66	.66	9	33	.22





Figure C.5.5.5 Equivalent of Fig. C.5.5.4 for  
 $\theta_1 = \theta_2 = 30^\circ$ .







## C.6 DISCUSSION OF RESULTS - CONCLUSIONS

The averaged experimental cross sections were compared directly with theoretical values without taking into account the finite experimental resolution since this would have required a Monte Carlo program and an enormous amount of additional computer time, especially for the arc projection. The theoretical values (solid line) were obtained with the computer code of Ebenhöh (Eb-72), which is a separable potential approximation of the exact three-body theory. The theoretical cross section is projected onto the kinematic arc length (except for  $35^\circ$ ,  $-35^\circ$  data projected onto E2 axis), while the experimental cross sections are projected onto a  $45^\circ$  line. Deviations between the experimental and theoretical distributions caused by this approximation should be very small in the QFS peak area since the locus curve closely coincides with the  $45^\circ$  line, except for the wings of the distribution where the locus has a sharp curvature. This results in a pileup of the projected experimental counts roughly in the areas where the theoretical curve predicts the minima between the QFS peak in the center and the two  $n_1p$  and  $n_2p$  Final State Interaction peaks on either end of the locus. Unfolding this effect would not be possible without a Monte Carlo program in the case of finite geometry as used in this experiment. The important point however is, that the QFS peak region remains unaffected.



Comparison between the experimental data obtained in the individual scattering angle pair geometries and the theoretical calculation using  $a_{nn} = -16.4 \text{ F}$  and  $r_{nn} = 2.86 \text{ F}$  for the n-n scattering length and the effective range show general agreement in the shape and amplitude of the QFS peak with the exception of the  $35^\circ - 35^\circ$  and  $28.7^\circ - 28.7^\circ$  sets.

The discrepancy observed in the  $35^\circ, -35^\circ$  set (Fig. C.5.5.1) could be attributed to the electronics troubles in the early stages of run #1 and to the uncertainty in the correction for the C6D6 bias interference with the minimum proton energy in the QFS peak (see dashed line in Fig. C.5.5.1). Electronics malfunction is also a possible cause of the  $28.7^\circ - 28.7^\circ$  discrepancy.

The proximity of the scattering angles corresponding to the three C6D6 detectors in runs #2 ( $23.8^\circ, 25.0^\circ, 26.2^\circ$ ) and run #3 ( $28.7^\circ, 25.0^\circ, 31.4^\circ$ ) made it possible to calculate the average cross sections of the adjacent sets and assign them to  $25.0^\circ, -25.0^\circ$  and  $30.0^\circ - 30.0^\circ$  quasi-free scattering angles respectively. Only  $30.0^\circ, -30.0^\circ$  and  $31.4^\circ, -31.4^\circ$  values were used for the average in run #3.

The statistical error, reduced up to 18% in this way (see Fig. C.5.5.5 and C.5.5.5), made it meaningful to include other values of the scattering parameters in the



comparison with the theoretical predictions (see various lines in the top parts of Fig. C.5.5.4 and C.5.5.5). Although the slight tendency of the  $25^\circ$ ,  $-25^\circ$  set to favour a shorter scattering length and a longer effective range is not convincingly supported by the  $30.0^\circ$ ,  $-30.0^\circ$  set, a general conclusion can be drawn, that the separable potential approximation of the exact three body theory fits the data of the present experiment very well. An overall agreement to within about 30% both in the shape and in the amplitude of the data with the predictions can be acknowledged.

The contributions of other possible sources of errors to the experimental cross section are mostly smaller than the statistical error (see Table 11).

The statistical uncertainty is lower than that of the only two previously existing n-n quasi-free scattering measurements, i.e., the data of Slaus et al. (S1-71) and Bovet et al. (Fo-74) obtained at the incident neutron energy of 14 MeV. The Slaus measurements of  $30^\circ$ ,  $-30^\circ$  quasi-free scattering was repeated in the work of Bovet et al. with additional measurements at  $41^\circ$ ,  $-41^\circ$  q.f.s. geometry. While the cross section at  $30^\circ$  agreed with the Slaus data, the cross section at  $41^\circ$  was found lower than the  $30^\circ$  cross section by a factor of 2 to 3. To check this discrepancy a QFS experiment is being prepared for the



TABLE 11 SUMMARY OF POSSIBLE ERROR CONTRIBUTIONS IN  
THE EXPERIMENTAL CROSS SECTION

<u>Contribution</u>	<u>Its Effect on Cross Section</u>
1. Statistical error	18% and higher as displayed by error bars in Figs. C.5.1, C.5.2, C.5.3, C.5.4, C.5.5 and as listed in Tables No: 2, 3, 4, 5, 6, 7, 8, 9 and 10
2. Statistical error in monitor sums	negligible
3. Uncertainty in the background subtraction in monitor peaks	less than 5%
4. Error in n-d elastic scattering cross section data	$\sim 8\%$ as quoted in (Se-71)
5. Energy spread due to the finite geometry	1 MeV horizontal averaging bars of the experimental cross section data points as indicated by the step-solid line in Figs. C.5.1 to C.5.5
6. Uncertainty in the neutron detector absolute efficiency	Variations of up to $\sim 20\%$ found possible





41.5° - 41.5° geometry at 21.5 MeV incident neutron energy. A pulsed deuteron beam will be used for the production of the 21.5 MeV neutrons and heavy water ( $D_2O$ ) will be used as the deuterium target.

In the meantime, QFS data have been obtained (in the way described in this work) also at angles (18.8°, -18.8°; 20.0°, -20.0°; 21.2°, -21.2°) and more data have been taken at (28.7°, -28.7°; 30.0°, -30.0°; 31.4°, -31.4°). The latter will hopefully allow replacing of the previous contradictory results at 28.7°, -28.7° geometry and thus give the possibility of obtaining a chain of cross section values for 30.0°, 28.7°, 26.2°, 25.0°, 23.8°, 21.2° and 20.0°, each an average over three adjacent sets. A least square fit to such a broad span of  $\sim 20\%$  statistical error data could be able to distinguish a certain combination of  $a_{nn}$  and  $r_{nn}$  values best fitting the data.

As our present results do not seem to support the (up to 80%) discrepancies reported in the pp q.f.s. experiments around 23 MeV incident energy (see Chapter A.2.3.2) they could confirm the speculations made in these reports that such disagreements are due to the lack of adequate Coulomb effect inclusion in the theoretical calculations.



## REFERENCES

- An-72 G. Anzelton, I. Slaus, D.J. Margaziotis and M.B. Epstein, Nuclear and Particle Physics A202 (1973) 593.
- Bo-69 D.P. Boyd, P.F. Donovan, J.F. Mollenauer, Phys. Rev. 188 (1969) 4.
- Bo-72 E. Bovet, P. Boschung and J. Rossel, Nuclear Instruments and Methods 101 (1972) 315.
- Br-71 W.J. Breithwaite, J.R. Calarco, J.M. Cameron and P.W. Storm, Nucl. Phys. A166 (1971) 515.
- Br-72 W. Breunlich et al., Nucl. Phys. A255 (1975) 267.
- Br-74 D.D. Brayshaw, Phys. Rev. Letters 32 (1974) 7.
- Ca-71 R.T. Cahil and I.H. Sloan, Nucl. Phys. A165 (1971) 161.
- Ca-72 R.T. Cahil, Nucl. Phys. A185 (1972) 236.
- Da-64 A.S. Darling, Hydrogen separation by diffusion through palladium alloy membranes, Reprinted from: The Less Common Means of Separation, published by The Institution of Chemical Engineers, March, 1964.
- Da-70 W.K. Dawson, J.F. Easton and D.A. Hutcheon, GPKS manual, Nucl. Res. Ctr., U of Alberta.
- Dr-72 M. Drosig, Nuclear Instruments and Methods 105 (1972) 573.
- Du-71 J.L. Durand et al., Phys. Rev. C4 (1971) 1957.
- Eb-72 W. Ebenhöf, Nuclear Physics A191 (1972) 97.
- Fa-61 L.D. Faddeev, Soviet Physics JETP 12 (1961) 5.
- Fo-74 F. Foroughi, E. Bovet and J. Rossel, Helv. Phys. Acta 48 (1975) 137.
- Go-70 M. Gourdin, Proc. Daresbury study weekend no. 1, ed. A. Connachi and E. Gabathuler (Science Research Council, Daresbury, 1970) p. 95.



- Gr-67 T.B. Grandy, 1967 Thesis, University of Alberta.
- Ha-65 R.P.R. Haddock et al., Phys. Rev. Letters 14 (1965) 318.
- He-27 W. Heisenberg, Z. Physik 43 (1927) 172.
- He-67 L. Heller, Rev. Mod. Phys. 39 (1967) 584.
- He-69 E.M. Henley, Isospin in nuclear physics, ed. D.H. Williamson (North Holland, Amsterdam, 1969) p. 17.
- He-72 E.M. Henley and T.E. Keliher, Nucl. Phys. A189 (1972) 632.
- Ka-51 J. Katz and E. Rabinowitch, The Chemistry of Uranium, Pt. I, Chapt. 8 (The Uranium-Hydrogen System), McGraw-Hill, 1951.
- Kl-73 H. Klein, H. Eichnev, H.J. Helten, H. Kretzer, K. Prescher, H. Stehle and W.W. Wohlfarth, Nucl. Phys. A199 (1973) 169.
- Ku-61 A.J. Kuches et al., Ann. of Phys. 15 (1961) 193.
- Lo-64 C. Lovelace, Phys. Rev. 135 (1964) B1225.
- Lo-68 E.L. Lomon and H. Feshbach, Ann. of Phys. 48 (1968) 94.
- Ma-70 D.J. Margaziotis, G. Paic, J.C. Young, J.W. Verba, W.J. Braithwaite, J.M. Cameron and T.A. Cahil, Phys. Rev. C2 (1970) 2050.
- Ma-71 D.J. Margaziotis, J.C. Young, I. Slaus, G. Anzelton, F.P. Brady and R.T. Cahil, Physics Letters 37B (1971) 263.
- Ma-71 T.G. Masterson and F.T. Noda, Tritium Furnaces - report University of Wisconsin, Madison, Wisconsin, 1971.
- Mc-71 I.E. McCarthy and P.C. Tandy, Nucl. Phys. A178 (1971) 1.
- Mi-55 (A.B. Migdal, J.E.T.P. (Sov. Phys.) 1 (1955) 2.
- Ne-71 J.W. Negele, Nucl. Phys. A165 (1971) 305.



- No-68 H.P. Noyes et al., Conference on Three-Particle Scattering in Quantum Mechanics (Texas A&M, 1968).
- Ny-68 D.R. Nygren, 1968 Thesis, University of Washington.
- Ok-67 K. Okamoto and C. Lucas, Nucl. Phys. B2 (1967) 346; Nuovo Cim. 48A (1967) 233.
- Pa-70 M.H. Partovi and E.L. Loman, Phys. Rev. D2 (1970) 1999.
- Pa-75 Pauleta et al., Nucl. Phys. A255 (1975) 267.
- Pe-70 E.L. Petersen et al., Phys. Lett. 31B (1970) 209.
- Pe-74 E.L. Petersen and M.I. Hoftel, Few Body Problems in Nuclear and Particle Physics, int. conf. (1974) Laval University, Quebec.
- Re-76 Reviews of Modern Physics, Vol. 48, No. 2, Part II (April 1976).
- Sa-67 E.O. Alt, P. Grassberger and W. Sandhas, Nucl. Phys. B2 (1967) 167; Phys. Rev. C1 (1970) 85.
- Sa-76 P.U. Sauer, in Few Body Dynamics, proceedings of the VII International Conference on Few Body Problems in Nuclear and Particle Physics (Delhi-1976).
- Se-72 J.D. Segrave et al., Elastic Scattering and Polarization at Fast Neutrons by Liquid Deuterium and Tritium, Reprinted from Annals of Physics 74 (1972) 1.
- Sh-73 S. Shirato et al., Nucl. Phys. A215 (1973) 277.
- Sl-70 I. Slaus, Three body problem in nuclear and particle physics, ed. J.S.C. McKee and P.M. Rolph (North-Holland, Amsterdam 1970) p. 337.
- Sl-71 I. Slaus, J.W. Sunier, G. Thompson, J.C. Young, J.W. Verba, D.J. Margaziotis, P. Doherty and R.T. Cahil, Phys. Rev. Letters 26 (1971) 789.
- Sm-68 Smith et al., Nucl. Inst. and Meth. 64 (1968) 164.
- So-73 J. Soukup, Report 1973, Univ. of Alberta.





- So-74 J. Soukup, J.M. Cameron, W.J. McDonald, G.C. Neilson and S.T. Lam, NRC, U of A, Internal Report #68.
- So-76 J. Soukup, NRC, U of A, Internal Report, 1976.
- Va-71 V. Valkovic et al., Nucl. Phys. A166 (1971) 547.
- Vr-74 D. Vranic, I. Slaus, G. Paic and P. Tomas, Few body problems in Nuclear and Particle Physics, int. conf. (1974) Laval University, Quebec City.
- Wa-52 K.M. Watson, Phys. Rev. 88 (1952) 1163.
- Wa-70 R.L. Walter, Proc. 3rd Int. Symp. on Polarization Phenomena in Nuclear Reaction, Madison, 1970 (Eds., H.H. Barschall and W. Haeberli, University of Wisconsin Press, Madison, 1970) p. 317.
- Wi-63 R. Wilson, The Nucleon-Nucleon Interaction (J. Wiley & Sons, N.Y.) 1963.
- Ya-54 Y. Yamaguchi, Phys. Rev. 95 (1954) 1628.
- Yu-35 H. Yukawa, Proc. Phys. Math. Soc. Japan 17, (1935) 48.
- Ze-70 B. Zeitnitz, R. Maschuw and P. Suhr, Nucl. Phys. A149 (1970) 449.
- Ze-72 B. Zeitnitz, R. Maschuw, P. Suhr and W. Ebenhöf, Phys. Rev. Letters 28 (1972) No. 25.



## APPENDIX 1. THE SAFETY SYSTEM

In addition to the internal safety features of the FNPF cryostat described in Chapter B2. an external safety system existed (see Figure AP.1) including: Fast acting valve (3) triggered by a Veeco ionization vacuum gauge (2), system of vacuum baffles (4) and a 400  $\ell$ /sec ion pump (5) providing efficient differential pumping, sealed vacuum system, vented into a duct (9) with exhaust fan at the roof level (10) and monitored for tritium contamination by a tritium monitor (11). During an experimental run all vacuum pumps on the beam line between the cryostat and the fast acting valve were outlet into a sealed storage tank (7), which was evacuated into the duct again after each run unless an accident occurred.

The following features were included in the interlock system:

1. Vacuum gauge (2)
2. Fast acting valve (3) cocked
3. Mobley rotary pump outlet closed
4. Fast acting valve (3) armed
5. Storage tank pressure < 1 atm. (8)
6. Outer case of T<sub>2</sub> manifold evacuated (16)
7. T<sub>2</sub> monitor in stack (11)
8. T<sub>2</sub> monitor of target position (12)
9. Liquid He present
10. Liquid N<sub>2</sub> present (18)
11. Cryostat vacuum (17)
12. Duct extract on.



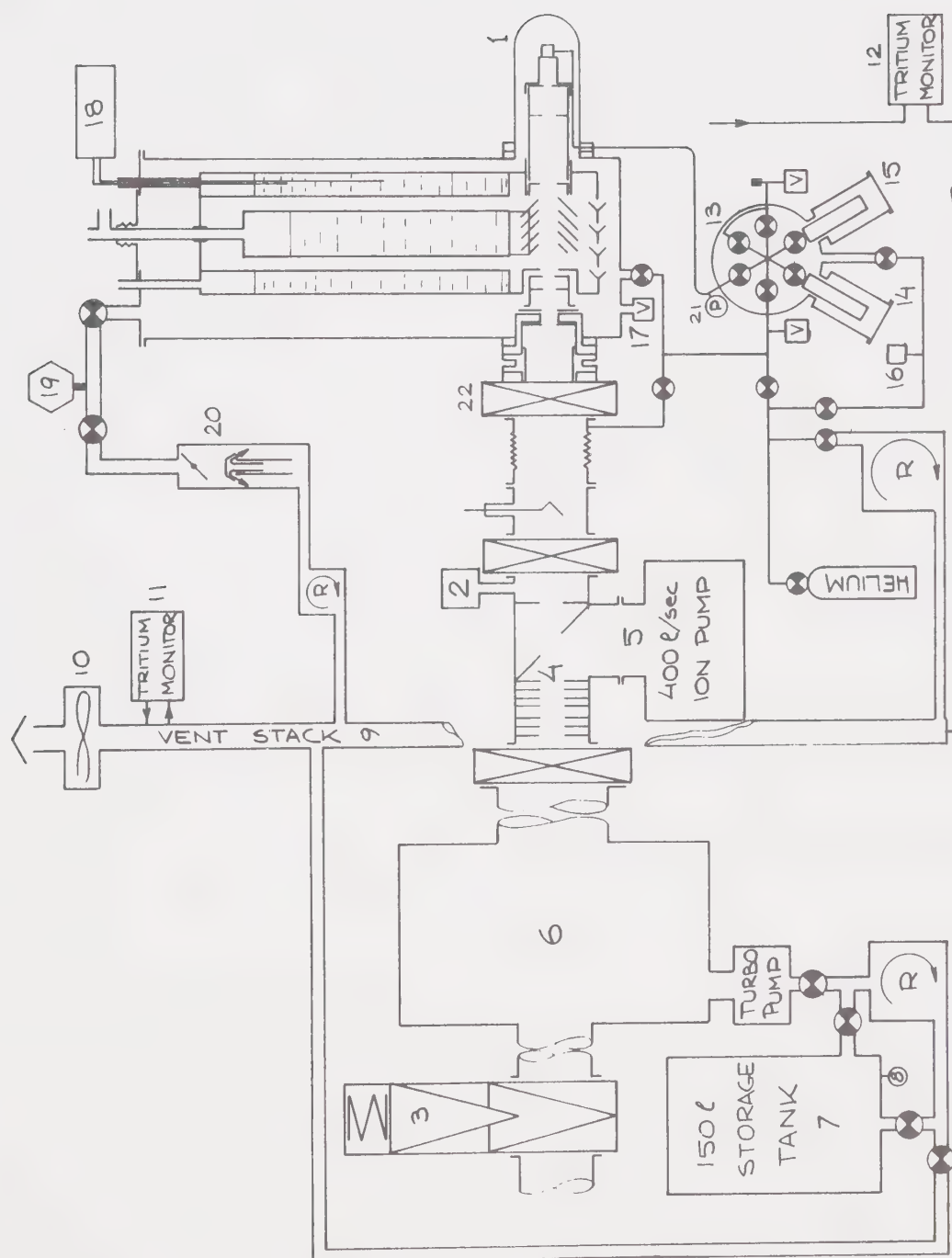


Figure AP.1 The safety system

















**B30178**